Universidade do Minho
Escola de Ciências

Alcinda Valéria Gomes Silva

Multifunctional magnetic nanolipogels based on peptide hydrogels for application in combined cancer therapy

dezembro de 2021

Multifunctional magnetic nanolipogels based on peptide hydrogels for application in combined cancer therapy
Alcinda Valéria Gomes Silva
UMinho|2021

Universidade do Minho
Escola de Ciências

Alcinda Valéria Gomes Silva

Multifunctional magnetic nanolipogels based on peptide hydrogels for application in combined cancer therapy

Master's Dissertation
Master in Biophysics of Bionanosystems

Performed under supervision of
Professor Doctor Elisabete Maria dos Santos Castanheira Coutinho
and
Professor Doctor Paula Margarida Vidigal Soares Teixeira Ferreira

December 2021

DIREITOS DE AUTOR E CONDIÇÕES DE UTILIZAÇÃO DO TRABALHO POR TERCEIROS

Este é um trabalho académico que pode ser utilizado por terceiros desde que respeitadas as regras e boas práticas internacionalmente aceites, no que concerne aos direitos de autor e direitos conexos.

Assim, o presente trabalho pode ser utilizado nos termos previstos na licença abaixo indicada.

Caso o utilizador necessite de permissão para poder fazer um uso do trabalho em condições não previstas no licenciamento indicado, deverá contactar o autor, através do RepositóriUM da Universidade do Minho.

Licença concedida aos utilizadores deste trabalho

Atribuição-CompartilhaIgual
CC BY-SA

https://creativecommons.org/licenses/by-sa/4.0/

ACKNOWLEDGEMENTS

This work, being a challenging project carried out in a challenging year, could not have succeed without the kindness and unconditional support of the people mentioned below.

First, I thank Doctor Elisabete Coutinho and Doctor Paula Ferreira, my research supervisors, for allowing me to explore such an emerging area. I appreciate all the trust, motivation, and constructive criticism when nothing seemed to work out. I extend my regards to Doctor José Alberto Martins and Doctor Peter Jervis for their willingness to help and for promoting such a positive atmosphere in the laboratory.

A word of appreciation to Doctor Loic Hilliou, Doctor Paulo Coutinho and Doctor Cacilda Moura for assisting me in their respective disciplines.

I further acknowledge the Centre of Physics of the University of Minho and Porto and the Centre of Chemistry of the University of Minho for providing the resources and facilities necessary for the research, and FCT, FEDER, PORTUGAL2020 and COMPETE2020, for funding under the projects PTDC/QUI-QFI/28020/2017 (POCI-01-0145-FEDER-028020) and PTDC/QUI-QOR/29015/2017 (POCI-01-0145-FEDER-029015). I also express my gratitude to the Unidade de Microscopia Eletrónica of University of Trás-os-Montes and Alto Douro for providing X-ray diffraction measurements and to C.A.C.T.I. of the University of Vigo for the transmission electron microscopy and hyperthermia studies.

I am deeply grateful to my lab mate and friend Sérgio Veloso. I can't even imagine this year without him. I also thank my friends André, Carlos and Patrícia, for sticking with me through the good and the bad days.

E como a racionalidade se apoia na emoção, pai, mãe, Nuno: obrigada por serem a minha inspiração, todos os dias.

STATEMENT OF INTEGRITY

I hereby declare having conducted this academic work with integrity. I confirm that I have not used plagiarism or any form of undue use of information or falsification of results along the process leading to its elaboration.

I further declare that I have fully acknowledged the Code of Ethical Conduct of the University of Minho.

Nanolipogéis magnéticos multifuncionais baseados em hidrogéis peptídicos para aplicação na terapia combinada do cancro

RESUMO

A terapia do cancro constitui uma das principais ocupações da nanomedicina, contribuindo, assim, para o seu rápido desenvolvimento. Esta área torna possível integrar várias modalidades terapêuticas e de diagnóstico numa única plataforma com o intuito de ultrapassar o paradigma atual do tratamento oncológico.

Os hidrogéis supramoleculares, em particular os hidrogéis baseados em péptidos de baixo peso molecular, têm provado ser eficazes como sistemas de entrega de fármacos, devido à sua capacidade de alterar a solubilidade, direcionamento, metabolismo e toxicidade de agentes terapêuticos. Os magnetolipossomas plasmónicos, para além de serem passíveis de controlo remoto com a aplicação de um campo magnético externo, aumentam a eficiência de libertação dos fármacos encapsulados quando termicamente estimulados, por exemplo, com hipertermia magnética e ótica. Assim, a combinação destes materiais – originando magnetolipogéis – permite reunir várias funcionalidades (entre as quais a hipertermia e a entrega de fármacos controlada a nível espacial e temporal) e, assim, otimizar a especificidade e eficácia dos agentes quimioterapêuticos utilizados atualmente.

Neste trabalho, foram sintetizados dois hidrogeladores baseados em desidrodipéptidos e selecionado o mais adequado para posterior funcionalização com magnetolipossomas plasmónicos; os últimos foram preparados a partir de nanopartículas núcleo/coroa de ferrite de manganês/ouro. Após a caracterização individual dos componentes no que concerne às suas propriedades reológicas, espetroscópicas e magnéticas, o magnetolipogel foi igualmente caracterizado e avaliado quanto à sua capacidade para transportar e libertar fármacos de forma controlada. Para tal, testou-se a resposta do magnetolipogel carregado com a molécula modelo 5(6)-carboxifluoresceína a um campo magnético alternado de baixa frequência e a vários de tipos de irradiação na zona do visível e do infravermelho-próximo. Os resultados obtidos revelaram que o sistema é um bom transportador de fármacos hidrofílicos, permitindo antever a entrega de agentes terapêuticos em resposta a um campo magnético e à aplicação de luz. Estas constatações, juntamente com o potencial do gel compósito para hipertermia e direcionamento magnético, podem abrir caminho para uma nova era no tratamento do cancro e de outras patologias.

Palavras-chave: Materiais macios, Magnetolipogel, Nanomagnetismo, Plasmónica, Terapia do Cancro.

Multifunctional magnetic nanolipogels based on peptide hydrogels for application in combined cancer therapy

ABSTRACT

Cancer therapy is an important discipline in nanomedicine and one of the main reasons for the rapid development of this research area. This field promises the integration of multiple therapeutic and diagnostic modalities in a single platform with the aim of overcoming the current paradigm of cancer treatment.

Supramolecular hydrogels, particularly low molecular weight peptide hydrogels, have been showing to be quite suitable drug delivery systems due to their ability to change solubility, targeting, metabolism and toxicity of drugs. Plasmonic magnetoliposomes, in addition to being remotely controllable with the application of an external magnetic field, also increase the efficiency of encapsulated drug release through thermal stimulation, e.g, with magnetic and optical hyperthermia. Thus, the combination of those two materials – giving magnetolipogels – brings together several functionalities, among which are hyperthermia and spatiotemporally controlled drug delivery. This allows increasing both the specificity and the efficacy of the currently used anticancer drugs.

In this work, two hydrogelators based on dehydrodipeptides were synthesised and the most convenient one was selected for further functionalisation with magnetoliposomes; the latter were prepared from manganese ferrite/gold core/shell nanoparticles. After individually characterising the components with regard to their rheological, spectroscopic, and magnetic properties, the magnetolipogel was equally characterized and evaluated concerning its ability to deliver drugs in a controlled way. To this end, the response of the 5(6)-carboxyfluorescein-loaded magnetolipogel to a low-frequency alternating magnetic field and to different types of irradiation with visible-near infrared light was assessed. The results showed that the system is a proper carrier of hydrophilic drugs and allow to envisage photo- and magneto-responsive drug delivery. These facts, together with the magnetic guidance and hyperthermia capabilities of the developed composite gel, may pave the way to a new era in the treatment of cancer and other diseases.

Keywords: Soft materials, Magnetolipogel, Nanomagnetism, Plasmonics, Cancer Therapy.

INDEX

ABBREVIATIONS AND ACRONYMS

3D	Three dimensional
AMF	Alternating magnetic field
AML	Aqueous magnetoliposome
APTES	(3-aminopropyl)triethoxysilane
Boc_2O	Di-*tert*-butyl dicarbonate
br	Broad
CAC	Critical aggregagtion concentration
Cbz	Benzyloxycarbonyl
CF	5(6)-carboxyfluorescein
CGC	Critical gelation concentration
DMAP	*N,N*-dimethylpyridin-4-amine
DMSO-d_6	Deuterated dimethyl sulfoxide
DNA	Deoxyribonucleic acid
DOX	Doxorubicin
DPPC	Dipalmitoylphosphatidylcholine
Fmoc	Fluorenylmethoxycarbonyl
G'	Elastic modulus
G''	Viscous modulus
GNP	Gold Nanoparticle
HBTU	*N,N,N',N'*-tetramethyl-*O*-(1*H*-benzotriazol-1-yl)uronium hexafluorophosphate
HR-MS	High-Resolution Mass Spectrometry
IDM	Indomethacin
ILP	Intrinsic loss power
LAOS	Large Amplitude Oscillatory Shear
LF-AMF	Low frequency-alternating magnetic field
MH	Magnetic hyperthermia
ML	Magnetoliposome
MMP	Metalloproteinase
MNP	Magnetic nanoparticle
MRI	Magnetic resonance imaging

Nap	Naphthalene
NIR	Near-Infrared
NMR	Nuclear Magnetic Resonance
NP	Nanoparticle
Npx	Naproxen
PDI	Polydispersity index
PDT	Photodynamic therapy
PS	Photosensitizer
PTT	Photothermal therapy
PTX	Paclitaxel
RGD	Arginylglycylaspartic acid
ROS	Reactive oxygen species
SAOS	Small amplitude oscillatory shear
SLP	Specific loss power
SML	Solid magnetoliposome
SPION	Superparamagnetic iron oxide nanoparticle
SPM	Superparamagnetic
SPR	Surface plasmon resonance
SQUID	Superconducting quantum interference device
STEM	Scanning transmission electron microscopy
T_C	Curie temperature
TEM	Transmission electron microscopy
TFA	Trifluoroacetic acid
TLC	Thin-layer chromatography
T_m	Melting temperature
TMG	*N,N,N',N'*-tetramethylguadinine
TRAIL	Tumour necrosis factor-related apoptosis-inducing ligand
XRD	X-ray diffraction
ω	Strain angular frequency
γ	Strain amplitude

INDEX OF FIGURES

INDEX OF TABLES

INDEX OF SCHEMES

Chapter 1

INTRODUCTION

1.1 CANCER NANOMEDICINE

Today, cancer-related mortality continues to show exceedingly high levels because of its rapid progression and limited therapeutic options with considerable toxicity. This mortality is expected to rise to 13.1 million deaths in less than ten years, so there is an urge for more effective and less toxic therapeutic systems (1,2). In cancer treatment, nanotechnology goes beyond drug delivery: it concerns with the creation of new therapies through the exploitation of nanomaterials properties (3). It allows targeting chemotherapeutic drugs, like doxorubicin (DOX) and methotrexate, directing them to cancer cells, guiding tumour surgery and improving the radiation-based treatment modality. This results in lower side-effects for the patient and, thus, in a higher survival rate (4). Nanotechnological targeted therapy has been defined as a type of treatment that specifically blocks the growth of cancer cells, instead of interfering with all cells that proliferate rapidly (5–8). As the formulation of new drugs to treat cancer takes time and requires a lot of investment, the scientific community turned to the reformulation of traditional drugs for innovative therapies (9). In this segment, nanomedicine in cancer treatment has evolved from a general approach to targeted systems, so some stimuli, either endogenous (e.g., temperature and pH) or exogenous (such as light and magnetic field), can be used to drive the therapeutic agents towards the disease site or trigger their activation at the selected location (10,11).

1.2 HYDROGELS

Thereby, the demanding revolution in the pharmaceutical market is centred in the development of drug delivery systems/platforms that can address the challenges of cancer treatment. For such, the encapsulation of drugs in well-defined nanostructures, such as hydrogels, has been extensively investigated due to their unique physical-chemical properties (12,13). Hydrogels are solid-like materials that retain significant amounts of water, while maintaining a distinct 3D structure; they can be divided in chemical or physical gels, based on the nature of the crosslinks (14,15). In chemical hydrogels, the crosslinks are established through covalent bonds and physical/supramolecular ones are held together by non-covalent molecular interactions, such as, hydrogen bonds, electrostatic or π-π interactions. This interplay can be disrupted by changes in the environment, such as temperature, pH, ionic strength, stress and by the presence of specific solutes. Consequently, the formation of physical hydrogels is often reversible, and the transition sol-gel is faster when compared to chemical networks (14).

1.2.1 Supramolecular peptide hydrogels

The self-assembly process – with biological origins – can be potentially exploited in the laboratory settings (16,17). In this context, peptides and their derivatives showed to be very interesting building blocks for the construction of supramolecular hydrogels. These biomolecules allow a high-water content and a tuneable viscoelasticity, whilst being biocompatible and often injectable, thus allowing their application in several fields of biomedicine (15). The self-assembly process depends on the hydrophobic and hydrophilic characteristics as well as the hydrogen bond balance of the hydrogelators. Thus, low molecular weight peptide hydrogelators are usually protected at the *N*-terminus with bulky aromatic moieties, such as fluorenylmethoxycarbonyl (Fmoc), benzyloxycarbonyl (Cbz), naphthoyl or pyrenyl groups (**figure 1.1 A**) (17,18). One of the major drawbacks concerning these materials is their susceptibility to proteolysis. This can be circumvented by using non-proteinogenic amino acids like D-, β- or α,β-dehydro- amino acids. Besides being resistant to proteolysis, the latter (**figure 1.1 B**) impose conformational constraints that might be favourable to the self-assembly process (15,19–21).

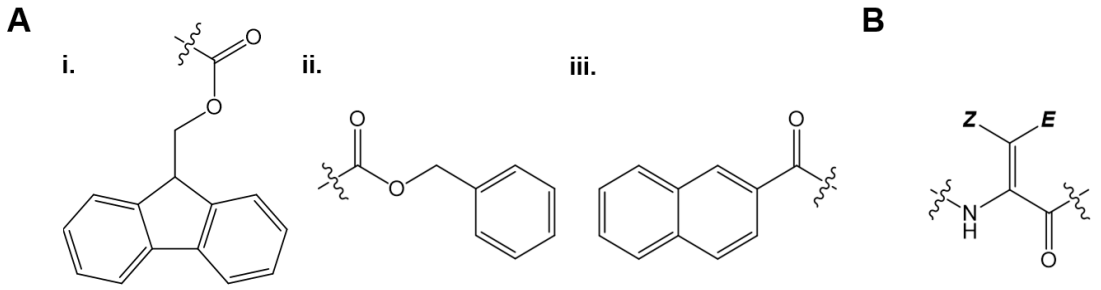

Figure 1.1 – Structure of *N*-capping aromatic groups of peptide hydrogelators (A): fluorenylmethoxycarbonyl (Fmoc) (i), benzyloxycarbonyl (Cbz) (ii) and 2-naphthoyl (iii); general scheme of an α,β-dehydroamino acid residue (B).

More and more studies are being carried out on the effect of amino acid sequence, chemical modifications, and mechanical tuning of hydrogels. The above-mentioned drug encapsulation and delivery depends not only on the diffusion of drugs in the hydrogel mesh but also on the nanofibres dissociation (22), so the study of thermodynamics and self-assembly process of hydrogel-forming peptides is of great importance (23). There is an agreement regarding the general mechanism of association of peptide fibres. It includes monomer conformational changes and hierarchical self-assembly – nuclei genesis followed by their growth into fibrils – that culminates in the lateral association of one-dimensional structures (**figure 1.2**) (23–25). However, it should be noted that it becomes more complex to describe the mechanism of the assembly of peptide-drug conjugates than that of pure peptides since the properties of drugs are quite different from those of amino acids; this results in additional molecular interactions and morphologies (26–28).

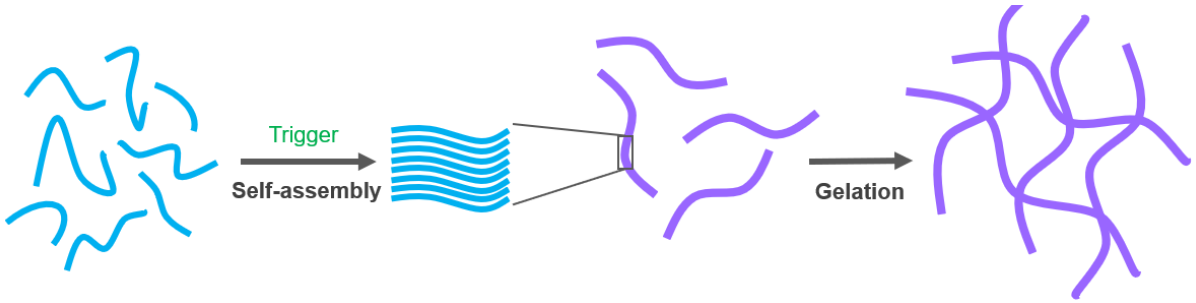

Figure 1.2 – Schematic of the self-assembly of short peptides to form supramolecular hydrogels.

1.2.1.1 Applications in cancer treatment – drug delivery

The properties of supramolecular peptide based hydrogels can eliminate some of the complications addressed in section 1.1, due to the possibility of localized drug administration (15,19–21).

1.2.1.1.1 Self-assembly and drug release triggers

As the structure of these kind of materials changes according to certain alterations in the environment, in a drug-loaded gel, drug release and retention depend on certain stimuli – smart peptide hydrogels (28,29). For these reasons, an approach to the main chemical and physical triggers by which peptides give rise to platforms for drug delivery applications is provided below.

1.2.1.1.1.1 *pH*

Considering the objective of the present work, small peptides that respond to a pH drop are of particular interest (30,31). Hydrogels that trap drugs at a higher pH than the one at which they are released are suitable for carrying chemotherapeutics, since they are endowed with selectivity for cancer cells (tumours are characterized by an acidic pH) (30–32). Apart from selectivity, which enables the reduction of side effects, these materials allow sustained drug release and are easy to prepare, since their synthesis mostly requires acid-sensitive linkers, ionizable groups or specific peptide sequences (33,34). As the fibres are made up of amphiphilic molecules, the charge of the peptides is highly influenced by the medium pH, leading to the association or dissociation of the monomers. These hydrogels, with pK_a closer to the pH of the tumour microenvironment, have their pH-sensitive moieties protonated in acidic environments, which alters the balance between hydrophobic and hydrophilic interactions; here, the fibrous network of the hydrogel is broken, promoting the release of the loaded therapeutic agents (33–35).

1.2.1.1.1.2 *Temperature*

Differently, thermo-responsive supramolecular peptide hydrogels are not widely explored, perhaps owing to the denaturing effect of temperature on these materials (36). Commonly, temperature-sensitive

hydrogels, when assembled in the body, can reverse the sol-gel state in places with large amounts of water (36,37). In fact, this type of hydrogel is advantageous when used as an injectable system: in the sol phase, the solution embodies drugs and converts to the gel phase when injected into the target tissue as a response to body temperature (38).

There are several other factors that trigger changes in gels, such as the presence of metal ions, redox reactions, and light (39); however, they will not be addressed here as they are not significant to the comprehension of this work.

1.2.1.1.2 Drug release profiles

As the reader may have noticed, we can take advantage of those stimuli to control hydrogels properties, and thus control the respective drug delivery profile, as the latter is shaped not only by the loaded drugs and the release medium, but also by the physicochemical and structural characteristics of the fibril network (40–42). Hence, the fundamental aspects and kinetics involved in drug release from hydrogels will be covered here, as it remains an important topic of discussion for the safe delivery of drug molecules.

In swelling polymers, the molecular drug release mechanism is a combination of drug diffusion and polymeric network relaxation. So, modelling the solute movement in these materials is complex. In 1987, Ritger and Peppas claimed that the following equation, previously proposed by themselves to relate the amount of drug released and time (43), can also be applied to swelling-systems (not exceeding 25% expansion) for the first 60% release data (44):

$$\frac{M_t}{M_\infty} = kt^n \qquad (1.1)$$

where M_t is the mass of drug released at time t, M_∞ is the mass of drug released as time approaches infinity, k is a constant involving the properties of the drug and macromolecular network system and n is the diffusional exponent, which translates the transport mechanism (43,45). The diffusional exponent depends on the type of transport, hydrogel geometry and peptide polydispersity. When it takes the value of 0.5, the drug is released by Fickian diffusion (case-I transport); on the contrary, when it equals 1, the material erosion/swelling dominates the release process (case II-transport). When n is between 0.5 and 1, there is more than one mechanism at work in the system – non-Fickian drug release (26,43,44). We are now able to compare drug release characteristics of different hydrogel matrices. For such, we must find the value of k, which indicates the initial kinetics of drug release (over a unit of time), and the half-life of release $t_{1/2}$, which gives information about the time it takes for M_t/M_∞ to reach 50% (26).

Peptide hydrogels are degradable in virtue of the natural origin of the building blocks (46). The term "degradability" refers to the process by which the fibrils begin to release their content to the outside, in the presence of appropriate external thermodynamic conditions (40). When this process is the predominant drug release mechanism, it is important to distinguish between the two types of degradation: surface erosion vs. bulk decomposition (47,48). For example, some research works show that matrix metalloproteinase (MMP) enzymes can participate in the decomposition of MMP-substrate motif incorporating hydrogels. When the speed of the original enzyme-substrate reaction is higher than the speed of enzyme transport, we are dealing with surface erosion; otherwise, bulk degradation is operating (47). These concepts are outlined in **figure 1.3**. In fact, the in-depth study of target cellular parameters in predicting the degree of degradability of these materials is central to control solute release, since local conditions are constantly changing. The coexistence of diffusion, chemical reactions, moving boundaries, changes in volume, biological interactions and dissolution of amino acids make the characterization of the drug delivery process a hard task (40,41,47).

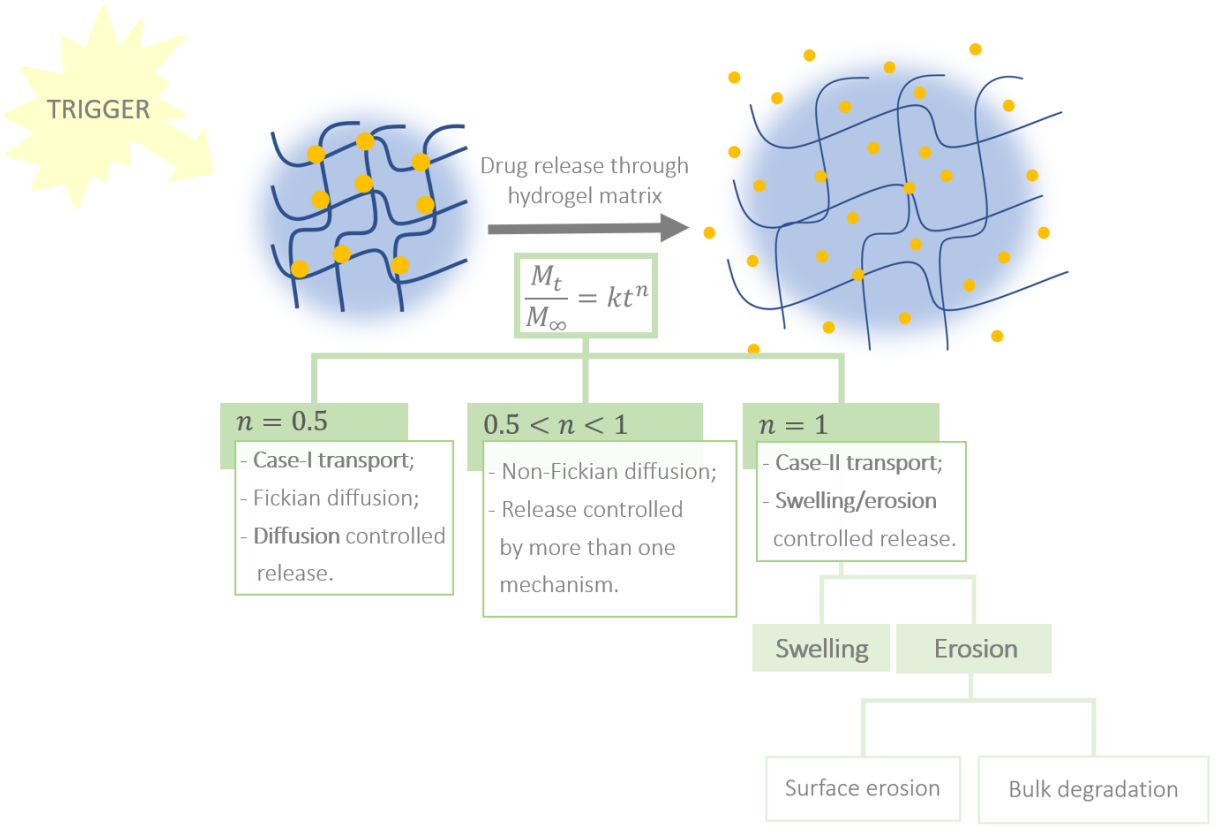

Figure 1.3 – Schematic representation of the different drug release kinetics from a hydrogel matrix and aspects to consider in case-II transport.

To precisely regulate the release rate of the anticancer drug paclitaxel (PTX), Chakroun designed several PTX-peptide conjugates with different critical aggregation concentrations (CAC) (49). CAC translates the

predisposition of the hydrogel filaments to dissociate. Thus, one can understand that the compound with the highest CAC has exhibited the highest release rate, while the compound with the lowest CAC has shown the slowest conjugate release. Taking this into account, a two-phase mechanism for pro-drug release has been inferred. The release of PTX-peptide conjugate began at the hydrogel-medium interface, where filaments dissociation and monomer diffusion occurred due to the entry of water (swelling) and osmotic pressure (47), respectively. Because of the gel's shrinkage, the second phase took place through bulk dissociation to achieve thermodynamic equilibrium with the surroundings (49). In this case, surface area was the point that explained the slow linear release profile of the drug-peptide conjugate. Some methods have been developed to modulate the sol-gel state of the matrix. For example, it is possible to define the lifetime of pH-responsive peptide hydrogels by programming the pH profile of the surrounding medium (50,51). Additionally, if we want to obtain a $t_{1/2}$ higher than one day, we can change the morphology and composition of the nanofibers introducing elements that increase electrostatic and hydrophobic interactions (increasing $t_{1/2}$ to 2 – 3 days) or inserting cleavable covalent bonds between the drug and the fibres (increasing $t_{1/2}$ to one week) (26). Still, Choe and Yun chose not to conjugate the drug with the self-assembling peptide. Instead, they loaded the Fmoc-FF-based hydrogel with an anti-inflammatory drug, indomethacin (IDM) (52). The value of n increased with the decrease in IDM content in the hydrogel, with super case II-transport for IDM 0.2%, case II-transport for IDM 0.4% and non-Fickian diffusion for IDM 0.5%. Therefore, for low concentrations of IDM, erosion predominates, which was proved when investigating the stability of the Fmoc-FF-based hydrogel in phosphate buffer. Interestingly, at an advanced stage, drug release rate was reduced for all IDM concentrations, and it was concluded that Fickian diffusion mechanism was operating (n<0.45) (26). Hence, a system was developed with a biphasic release profile, mouldable through changes in the loaded drug concentration (52).

1.3 NANOPARTICLES

"There's plenty of room at the bottom" is an inspiring invitation to enter a new field of physics (53). Since Feynman uttered this phrase, nanoscale knowledge has been presented as essential for biomedical sciences progress. It includes the study of nanoparticles (NPs), which are defined as particles of matter with nanometric dimensions (≤100 nm) (54,55). These materials present different physical-chemical characteristics, compared to their bulk phase: in addition to having a discrete electronic state, they also show greater chemical activity due to a higher area/volume ratio (56). This large surface area makes

them interesting candidates for several applications, mainly in pharmaceutics, biology and biomedicine (54). Their synthesis methods are classified into two main categories, depicted in **figure 1.4**: (i) top-down (macro-scale materials fragmentation) and (ii) bottom-up (atoms/molecules assembly), both being conducted in order to control composition, morphology (fibres, particles, cubes, disks) and size of NPs, and consequently, their mechanical, optical, electronic and magnetic properties (56–58).

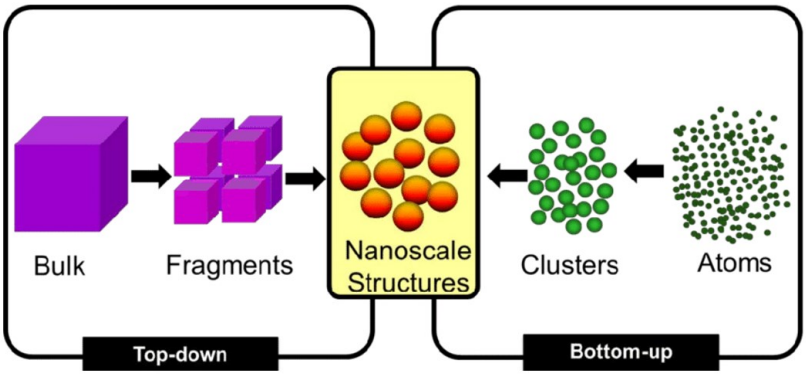

Figure 1.4 – Synthesis methods for nanofabrication. Reprinted from (58).

In fact, semiconductor NPs and metal clusters size controls the absorption and emission properties as a result of quantum confinement effect. Similarly, magnetic materials show size-dependent magnetization, as will be next discussed in detail (59). However, regarding the toxicity of these materials, many more aspects are involved, among which size, shape, aspect ratio, surface charge and tension, crystalline structure, aggregation, concentration, and roughness stand out. Interestingly, these factors can be adjusted through surface coatings or through NP incorporation in polymeric matrices, in order to modulate their pharmacokinetics and interaction with tissues (60,61).

Given the relevance of these materials in biomedicine, next sections will address, conceptually and functionally, specific nanoparticles, as well as some of their applications.

1.3.1 Magnetic nanoparticles

Nanoscopic magnetic systems are composed of nanoparticles or clusters with at least one dimension in the order of nanometres. The recent impulse in these materials research aims to obtain microsensors, soft magnetic materials with lower energy losses and faster responses and enhanced hard magnets for a wide range of applications, fluctuating between clinics and ceramics (62). Within the scope of this work, its application in cancer nanomedicine should be highlighted, through drug delivery, magnetic hyperthermia, and magnetic resonance imaging (MRI), in addition to the possibility of combining several therapeutic functions (63,64). Before studying magnetic NPs (MNPs) today's relevance, it is imperative

to understand the origin of the technical features that make them so useful in biomedicine; in this regard, nanoscale magnetism will be explained below.

Magnetic permeability μ translates the degree of magnetism induced in a material under an external magnetic field. There are three main types of materials, considering this physical property. Those with a μ value less than 1 correspond to diamagnetic ones, where the total angular momentum of the atoms is zero. On the other hand, with a magnetic permeability greater than 1, paramagnetic ($\mu>1$) and ferromagnetic ($\mu>>1$) materials emerge (65,66). Paramagnetism occurs in materials that show magnetization under a magnetic field and whose magnetic moment becomes zero when that is removed. In a slightly different way, ferromagnetism is characterized by the retention of magnetic properties when the magnetic field disappear. In these materials, there is hysteresis and spontaneous magnetization below a critical temperature (67,68). This type of magnetism only manifests when the material atoms/ions are arranged in a lattice and the respective magnetic moments interact collectively in order to align parallel to each other, forming domains (67,69). These domains' structure depends on three energetic terms, namely exchange interaction, magnetostatic and anisotropy energies. The first gives rise to ferromagnetic behaviour, the second is responsible for domain formation and the latter limits the width of the walls where its orientation gradually changes (68,70). Saturation magnetization can be used to characterize these materials properties because it measures their magnetization when all domains are aligned (68). It decreases as the material is heated due to moment alignment disturbance caused by atoms thermal agitation (67). This effect reaches the climax when the transition from ferromagnetic to paramagnetic behaviour occurs, at Curie temperature T_C (67,69).

Below T_C, bulk to nanometre-scale size reduction decreases the number of domains, decreasing the magnetostatic energy (65). Therefore, magnet dimensions also play a role in its magnetic behaviour. When it is small enough, the energy required for domains formation is greater than the energy needed for the maintenance of a single domain (62). This phenomenon can be illustrated in terms of coercivity (**figure 1.5**), that is, the external magnetic field intensity necessary to demagnetize a ferromagnetic material (71).

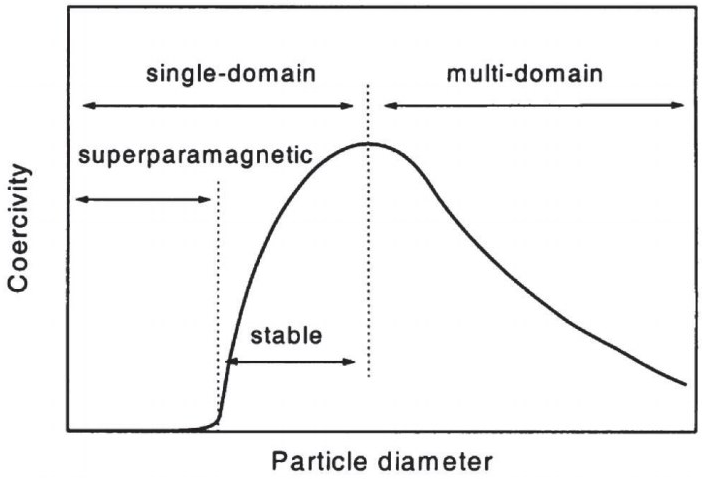

Figure 1.5 – Coercivity as function of magnet size. Reprinted from (65).

For decreasing diameters, coercivity increases to a maximum and then decreases to zero – superparamagnetic (SPM) transition point (72) – and for spherical MNPs, the respective (critical) size r can be calculated as denoted in **equation 1.2**:

$$r = \sqrt[3]{\frac{6k_B T_B}{K}} \qquad (1.2)$$

where k_B, T_B and K represent Boltzmann's constant, blocking temperature and anisotropy constant, respectively (72).

Taking into account the coherent rotation of all moments of a SPM particle and the energy barrier to the magnetization vector caused by anisotropy energy, the magnetization energy E_B is given by:

$$E_B = KVsen^2\theta - \mu Hcos(\alpha - \theta) \qquad (1.3)$$

where V is the particle volume, θ(α) is the angle between the particle's magnetic moment (applied field) and the easy-axis, μ represents the magnitude of the net magnetic moment and H is the applied field (62). In the absence of H, the particle remains in one out of two possible equilibrium states ($\theta = 0$ and $\theta = \pi$), separated by the energy barrier KV, which decreases with particle size reduction. Its magnetization relaxation occurs due to thermal fluctuations and the characteristic time for a flip (effective relaxation time τ) is calculated by Néel equation (**1.4**), in which T represents absolute temperature and τ_0 is inversely proportional to the jump attempt frequency of the particle magnetic moment between the opposite directions of the magnetization easy-axis.

$$\tau = \tau_0 e^{\frac{E_B}{k_B T}} = \tau_0 e^{\frac{KV}{k_B T}} \qquad (1.4)$$

Considering this, it is now possible to characterize T_B (**equation 1.5**), a parameter that pops up in **equation 1.2**, representing the temperature above which there is at least one flip during the observation/measurement time τ_m of the employed experimental technique (62,65).

$$T_B = \frac{KV}{k_B \ln(\tau_m/\tau_0)} \qquad (1.5)$$

Here, we can deduce that no flip is observed (blocked regime) when $\tau_m \ll \tau$ or $T < T_B$ and that NP magnetization flips (unblocked regime) when $\tau_m \gg \tau$ or $T > T_B$.

In fact, despite the ferromagnetic composition, MNPs exhibit a superparamagnetic behaviour because of their size ($\leq r$). These materials are characterized by high magnetic susceptibility, zero coercive field and absence of hysteresis, which makes them promising for cancer treatment (65,66).

1.3.1.1 Applications in cancer treatment

MNPs are commonly composed of metals such as iron, nickel, manganese, cobalt, and their oxides. Among the latter, iron oxides, such as magnetite (Fe_3O_4) and maghemite (γ-Fe_2O_3), stand out, due to their good colloidal stability and easy synthesis (73). Transition metal ferrites are the most chosen for biomedical applications, with manganese ferrite NPs showing enhanced magnetic susceptibility and tuneable magnetic properties, which makes them suitable for magnetically-guided drug delivery, hyperthermia, and MRI studies (74,75). However, this type of particles exhibits moderate levels of toxicity in biological systems (17,76). Thus, non-transition metal ferrites (e.g., calcium ferrite) emerge to allow an increased cell viability (since calcium is safely metabolized by human body), in addition to improving thermal stability and heating capacity, which makes them particularly interesting for magnetic hyperthermia (MH) (77–79). Nonetheless, in some cases, there is a need to minimize iron oxide NPs intracellular degradation (80,81). For such, these materials can be adorned with lipid bilayers, forming magnetoliposomes, and passivated with silica, enabling covalent functionalization with stealth and lysosomal escape agents, as will be later explored. Although these particles handling optimization is still a challenge, they already demonstrated great potential for several applications, such as those pictured in **figure 1.6** (80–83).

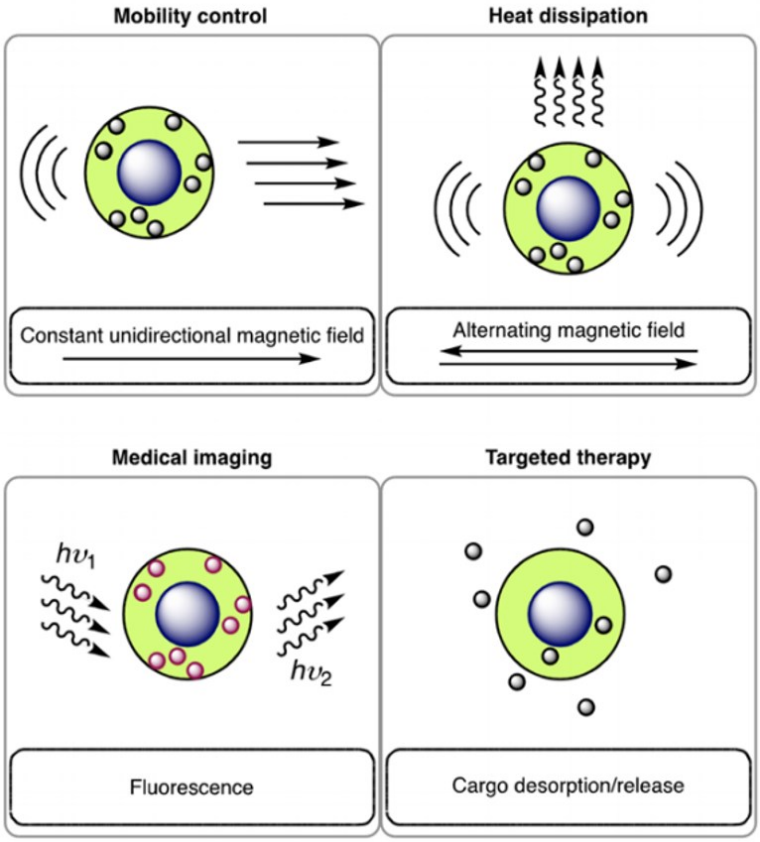

Figure 1.6 – MNPs therapeutic utilities. Adapted from (83).

1.3.1.1.1 Drug delivery

In addition to the *in vivo*-controllable movement through the application of an external magnetic field, MNPs can be safely administered to the body in colloidal formulations, reaching almost all tissues. This is extremely advantageous, given their ability to load and release molecules through physical encapsulation and chemical adsorption (83,84). This technique is effective in reducing side effects on healthy cells and non-specific molecular interactions, allowing for a reduction in the administered dose, mostly in cancer treatment (63,85). In fact, several studies have already been reported describing shell-coated iron oxide NPs that bind different anticancer molecules such as DOX, methotrexate, gemcitabine, mitoxantrone, epirubicin, carmustine, cytarabin, 5-fluorouacil, docetaxel and β-cyclodextrin (86). For example, Teng developed silica-coated iron oxide NPs. Mesoporous silica allowed DOX adsorption through π-π interactions and the respective pores enabled drug transport and pH-triggered release (87). This system looks effective for drug delivery, considering a greater and faster *in vitro* DOX release at acidic pH, due to the weakening of DOX binding to the NPs. The authors anticipate this nanosystem for *in vivo* magnetic guidance, taking advantage of magnetic properties of the particles (87). Core/shell particles actually show unique properties that cannot be provided by any other system (85).

However, if the point is to achieve clinical practice, MNPs synthesis must be complex enough to act as it is intended, but simple enough to get nanoparticles in the quantity and quality needed (63,85). For such, magnetoliposomes are very interesting. Bearing this in mind, Rodrigues *et al.* used 3-amino-6-(benzo[*d*]thiazol-2-ylamino)thieno[3,2-*b*]pyridine-2-carboxylate loaded lipid-coated manganese ferrite NPs and evaluated them as anticancer carriers (74). The pioneer results are very promising for multimodal cancer therapy, as the magnetoliposomes can be magnetically guided to the proper therapy site and release drugs through fusion with the cell membrane, in addition to the possibility of hyperthermia (74).

1.3.1.1.2 Magnetic hyperthermia

Today, cancer is treated through radiation, chemotherapy, and surgery; however, none of these methods are fully established (86,88). Although hyperthermia appears as an alternative, its application in the clinics is limited by its non-specificity, which leads to thermal toxicity of healthy cells. Encouragingly, the application of magnetic materials allows local hyperthermia through their exposure to a high frequency-alternating magnetic field (AMF) (63,89,90). This therapeutic strategy is based on raising the temperature in the vicinity of the tumour to 40-43 °C, affecting cellular structures, such as, membranes, cytoskeleton, macromolecules, and DNA, in addition to changing the expression of certain genes. This culminates in cancer cells death or their sensitization to radiation and chemotherapy (91–93). It dates to 1957, when Gilchrist and co-workers obtained the differential heating of nodes with γ-Fe_2O_3 particles, as a function of radiofrequency, magnetic field intensity and magnetic particles coercive force (5,94). Nowadays, this type of hyperthermia employs MNPs, which, being superparamagnetic, do not show any remaining magnetization upon magnetic field removal. Hence, in addition to being selective and non-invasive, MH avoids embolism in blood vessels (95–97).

That AMF causes heating effects in MNPs, through hysteresis losses and relaxation processes – Néel and Brownian relaxations (90). As described before, superparamagnetic NPs present only one domain, since all magnetic moments behave collectively, forming a superspin; in Néel relaxation (**figure 1.7**), this spin rotates while MNP physical orientation does not change. Here, magnetic energy is dissipated by magnetic anisotropy energy, which makes it difficult to reorient the superspin (82,97,98). The time required to bring it back into equilibrium is called Néel relaxation time τ_N and is given by **equation 1.6**.

$$\tau_N = \tau_0 e^{\frac{KV}{k_B T}} \qquad (1.6)$$

Differently, in Brownian relaxation (**figure 1.7**), the MNP rotates in the fluid to align the superspin with the direction of the applied magnetic field, while the spin remains fixed (96,97). In this process, thermal energy is produced by friction resulting from shear stress in the fluid. Brown relaxation time τ_B is calculated according to the following equation,

$$\tau_B = \frac{3\eta V_H}{k_B T} \qquad (1.7)$$

in which η is the medium viscosity and V_H is the particle hydrodynamic volume.

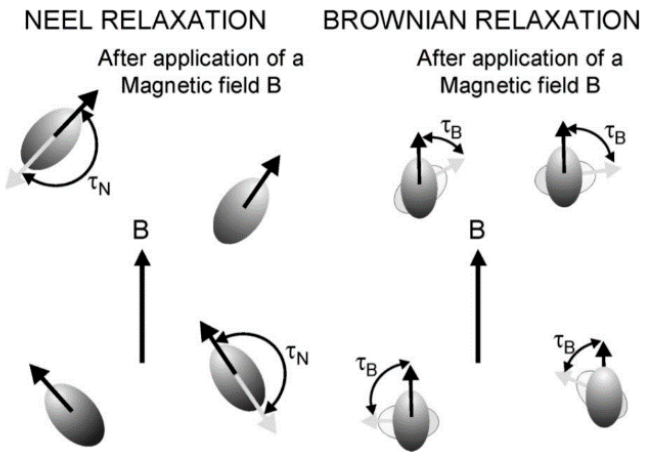

Figure 1.7 – Schematic representation of the Néel and Brownian relaxation mechanisms for a magnetic fluid. Reprinted from (98).

According to **figure 1.8**, the effective relaxation time τ corresponds approximately to the Néel relaxation time for particles with a radius less than 14 nm. On the other hand, for larger radii, τ approaches Brown's relaxation time.

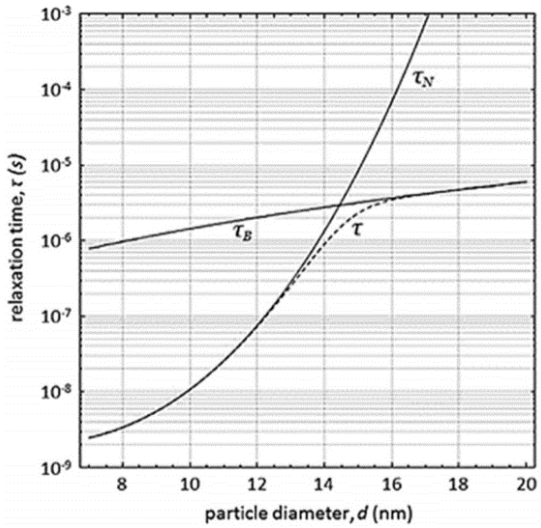

Figure 1.8 – Relaxation time for single domain magnetite NPs (K=25 kJ/m^3) in an aqueous medium (T=310 K, η=8.9×10^{-4} Pa s). The dashed line shows the effective relation time τ ($1/\tau=1/\tau_N+1/\tau_B$). Reprinted from (97).

As the former process is the predominant one in relaxation loss, when dealing with particles with a suitable size for tumour penetration and accumulation, τ_N assumes a great importance (95,96).

Although MH itself is considered a therapy and has several mechanisms that induce cell death, it is not effective due, for example, to the possible progressive tumour thermotolerance. Thus, its combination with chemotherapy can bring promising results (99). For such, Hayashi reported the synthesis of Fe_3O_4 nanoparticles associated with a polypyrrole-polyethyleneglycol-folic acid polymer that produce heat under the effect of an AMF and release DOX for myeloma treatment (100). The temperature increase at 44 ºC led to a change in the polymer that allowed drug release (100). For a similar purpose, Zhang produced an MH-mediated "tumour necrosis factor-related apoptosis-inducing ligand" (TRAIL) delivery system for a combined therapy using a thermosensitive and biodegradable polymeric hydrogel (101). Here, TRAIL and iron oxide NPs were complexed with poly(organophosphazene). Hyperthermia was found to restore the sensitivity of TRAIL-resistant cancer cells and to increase TRAIL-induced apoptosis through caspase activation (101). When producing these nanosystems, it is intended to obtain excellent structural and magnetic properties. Their performance as hyperthermia mediators depends on MNPs structure, size, anisotropy, and saturation magnetization (95,97,102). Some examples are given in **table 1.1**, in which the specific loss power (SLP) (figure of merit to evaluate MNPs heating capacity) values correspond to a 50 mT, 300 KHz AMF exposure, except for Co-, Mn-ferrite samples, in which the AMF refers to 30 mT, 700 kHz (96).

Table 1.1 – Optimization of magnetic particle hyperthermia efficiency based on magnetism tuning. Adapted from (102).

Material	$K\ (kJ/m^3)$	$H\ (kA\ m^{-1})$	**Optimum size** (nm)	$SLP\ (W/g)$
Co	412	1440	9	200
fcc-FePt	206	1140	9	215
$CoFe_2O_4$	200	448	9	360
$MnFe_2O_4$	3	546	10	136
Fe	48	1750	12	400
Fe_3O_4	9	446	19	170
γ-Fe_2O_3	4.7	414	24	165
$FeCo_3$	1.5	1790	34	600

The use of a high frequency applied magnetic field raises questions regarding safety in medicine. In order to obtain a greater amount of energy dissipated by MNPs, in addition to the optimum size shown above,

the applied magnetic field intensity-frequency product ($H \times f$) should be higher than the upper limit initially proposed in 1984 by Atkinson-Brezovich ($4.85\times10^8\ A\ m^{-1}\ s^{-1}$); therefore, there is a lower threshold to activate the mechanism. Nonetheless, there is also a maximum limit, imposed by the patient's safety and tolerance (102,103). Bearing this in mind, although the typical range of applied magnetic fields tolerated by living tissues is 10 kHz – 1 GHz, 1 – 100 mT, several studies have been made that describe much higher ranges, as shown in **table 1.2** (102–104).

Table 1.2 – Maximum field-frequency product tolerated by living tissues based on recent literature. Adapted from (102).

$H\ (kA\ m^{-1})$	**Frequency** (kHz)	$H \times f\ (\times\ 10^9\ A\ m^{-1}\ s^{-1})$	**Reference**
18	100	1.8	(103)
10	410	4.1	(105)
32	183	5.9	(106)
19	435	8.3	(107)
37.3	500	18.7	(108)

Several strategies are available to improve MH treatment effectiveness (103). However, recent studies point to the combination of MNPs and other materials, such as hydrogels, liposomes, and target functions, in order to achieve advances in thermo-chemotherapy. More details on this subject will be given later.

1.3.1.1.3 Magnetic Resonance Imaging

Magnetic Resonance Imaging (MRI) is a medical imaging technique that allows to obtain both molecular and anatomical information, offering good in depth-penetration and spatial resolution (109,110). This technique is based on the measurement of the signals emitted by magnetic field-exposed body protons. MNPs, especially superparamagnetic iron oxide nanoparticles (SPIONs), have been widely investigated as MRI contrast agents, in order to increase the performance of this technique (86,109,111). In addition to their large surface area, that allows the linking of several target and therapeutic functions (e.g., antibodies, peptides and small molecules), they are highly biocompatible comparatively to gadolinium (86,112). When SPIONs are exposed to a magnetic field, their moments align with the field direction, increasing the magnetic flux; this leads to a signal dephasing in relation to the surrounding protons. Actually, these particles work introducing local inhomogeneities by changing near hydrogen nuclei relaxation times, mainly T2 (spin-lattice) (113–117).

MNPs size also influences the signal dephasing mechanism. For smaller ones (in which the protons are under a changing magnetic environment), this phenomenon occurs through motion averaging

mechanism, where the dephasing is slow and incomplete due to the diffusion effect. After a critical size, a discreet and complete dephasing, driven by the visit-limited regime, is observed. For larger particles (those subject to a constant magnetic environment), the static dephasing mechanism prevails, in which the protons signal undergoes gradual changes (86,118). From here, the arrangement of MNPs and other materials (e.g., hydrogels) is anticipated in order to enhance relaxation rates, as it would control diffusion and other important parameters. Indeed, it is expected that the versatility of these materials enables an accurate, reliable, and non-invasive detection and identification of tumour and other diseases, thereby making progress around clinical diagnosis (86,119,120).

1.3.1.2 Interest of silica-coating

Despite all the potential of MNPs in biomedicine, there are some limitations inherent to their use. These drawbacks include agglomeration, resulting from dipole-dipole interactions, low affinity for biomolecules and iron leaching out, which can be serious in the case of cancer cells (121–123). According to the studies exposed so far, to overcome these limitations, MNPs are usually coated with ligands or polymers (121).

Silica coating, such as (3-aminopropyl)triethoxysilane (APTES), has been increasingly investigated on iron oxide nanoparticles. This organosilane shows great affinity for metal oxides (124) (either by adsorption or covalent binding) in such a way that its active amine gives MNPs the ability to conjugate biomolecules, drugs, and other functions (125,126). APTES surface-functionalized NPs are thus available for a wide variety of applications, including drug delivery, MH and MRI, as already reported in literature (125,127). Furthermore, APTES is a solution for the weak colloidal stability of MNPs, preventing capillary embolism in biomedical applications (128). This has been studied in detail by Saravanan; this author noticed that a solution of APTES-modified nanoparticles remained turbid 5 days from its preparation, indicating that the corresponding NPs had better dispersion than the non-functionalized ones, owing to a larger capacity of hydrogen-bonding with the solvent (129).

So, rational NP design techniques coupled with silanes flexibility is undeniably useful, not only in suppressing NPs inconveniences, but also in improving their abilities.

1.3.2 Plasmonic components-functionalized magnetic nanoparticles

MH is, in fact, very promising in cancer treatment due to the aforementioned non-invasiveness, remote control, absence of penetration depth limit, great resolution and molecular specificity. However, this modality still requires a relatively high dose of MNPs and carries the risk of tumour cells developing

resistance to applied thermal stress (130,131). Fortunately, MNPs can be easily combined with materials other than silica, getting extra functionalities. For example, the combination of MNPs with plasmonic NPs can make controlled target-directed applications possible, because of the equally interesting characteristics of those components, such as surface plasmon resonance (SPR) – widely used in sensors, bioassays, diagnostic tools, photothermia and photodynamic therapy (132,133). Due to the serious potential of these composites, the theoretical basics of nanoplasmonics are then provided.

Plasmon is a quantum of plasma oscillations. It involves the density of free electrons in a metal and is accompanied by an electromagnetic field created by the oscillating charges. Surface plasmons, particularly, in virtue of being plasmons confined by an interface between a metal and a dielectric, exist at frequencies lower than plasma frequency (**figure 1.9**) (134–136). Indeed, when the electrons in a metal conduction band are confined in space, the frequency of their oscillation admits discrete values – electromagnetic confinement effect, described by Mie in 1908. If it coincides with that of the incident light, the amplitude of that oscillation is maximum and SPR occurs. This phenomenon depends on the metal type, particle size, shape, structure, and composition, as well as the surroundings dielectric constant (135–137).

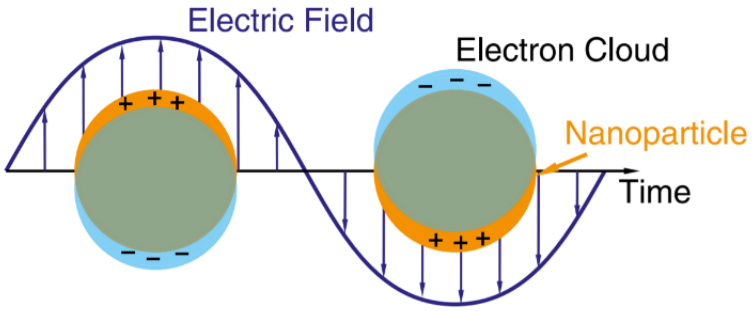

Figure 1.9 – Schematic representation of a localized surface plasmon. Reprinted from (134).

Spherical gold nanoparticles (GNPs) exhibit a SPR band around 520 nm (visible zone). When these nanoparticles are less than 10 nm in size, this band is greatly softened due to phase changes resulting from the higher surface electron collision rate. Increasing their size leads to a red shift in the SPR frequency, as well as an increase in band intensity. It follows that plasmon tunning can be done by controlling GNPs size during their synthesis (138–140). Considering the oxidation states of gold (Au^{+1}, Au^{+3} and Au^{0}), the most relevant step in this process is Au^{+1}/Au^{+3} reduction to Au^{0} (since Au^{0} is the desirable final state for GNPs), by adding an electron donor to the reaction (141). The most consensual precursor is $HAuCl_4$, in which gold is in the form of Au^{3+}. The Turkevich method treats it with citric acid in boiling water; here, the acid acts as a reducing and stabilizing agent and its proportion in relation to

gold can be changed according to the desired final size. In a more recent method, GNPs synthesis is carried out by a biphasic reduction, using tetraoctylammonium bromide as the phase transfer reagent and $NaBH_4$ as the reducing agent; this protocol produces small NPs (1.5 to 5 nm) with low dispersity by varying the reaction conditions such as temperature, reduction rate and gold-thiol ratio (142). In such small nanoparticles (with a diameter much smaller than the wavelength of light λ), the extinction coefficient σ_{ext} takes the following form (143):

$$\sigma_{ext} = \frac{18\pi[\varepsilon_m(\lambda)]^{3/2}}{\lambda} V \frac{\mathrm{Im}[\varepsilon(\lambda)]}{[\mathrm{Re}[\varepsilon(\lambda)] + 2\varepsilon_m(\lambda)]^2 + \mathrm{Im}[\varepsilon(\lambda)]^2} \qquad (1.8)$$

where $\varepsilon(\lambda)$ represents the wavelength dependent complex dielectric function, ε_m is the dielectric constant of the surrounding medium and V is the volume of the NP (143). In the absorption spectrum, the real part of the dielectric constant dictates the position of the SPR and the imaginary part is related to the respective bandwidth. The optical properties of GNPs can also be controlled via shape/structure tunning. Gold nanoshells are especially interesting for biomedical applications as SPR occurs at higher wavelengths (144). The shell thickness reduction from 20 to 5 nm translates into a 300 nm bathochromic shift, because of the coupling of the outer and inner surface layer plasmons for thinner shells, which is great considering the therapeutic window (700 – 1000 nm) (144).

1.3.2.1 Additional biomedical applications in photodynamic and photothermal therapies

GNPs action window is actually important when one intends to use them in cancer treatment, for example, through photodynamic therapy (PDT) and photothermal therapy (PTT). The former requires the use of a photosensitizer drug (PS) and a light source; the goal is for the drug to be excited in order to transfer energy to the molecular oxygen present in tumour tissues; this will produce reactive oxygen species (ROS) and lead to cell apoptosis. GNPs can take part in this process, as they increase ROS production through the formation of intracellular aggregates, which suggests that these NPs amplify the absorbed photonic energy, transferring it to the PSs (145). On the other hand, PTT is a method of heat ablation in which electromagnetic radiation energy is used to induce malignant tissues heating, parallel to MH. This is because the absorbed light can be converted into heat by non-radiative processes, through the fast phase loss of the coherently excited electrons (146–148). Each NP can be considered an individual heat source and the localized increase in temperature around a single NP depends on the absorption cross section, laser intensity, NP morphology and both metal and surroundings thermal conductivities (149). Thus, the surface heating ΔT_{NP} of an individual NP in medium is given by

$$\Delta T_{NP} = \frac{\sigma_{abs} I}{4\pi R_{eq} \beta k_0} \qquad (1.9)$$

where σ_{abs} denotes absorption cross section, I is the power density of the incident light, R_{eq} is the equivalent radius of a sphere with the same volume as the particle, k_0 is the thermal conductivity of the surrounding medium and β represents the thermal capacity coefficient dependent on the particle aspect ratio (ar) ($\beta = 1$ for nanospheres and $\beta = 1 + 0.96586(\ln^2(ar))$ for nanorods) (149). From **equation 1.9**, it is concluded that the temperature increase on a single NP surface is very low. However, when many GNPs are used, a significative temperature increase is achieved (149). Thus, one can understand the need of functionalizing MNPs with plasmonic NPs, as proposed at the beginning of this section, to increase the heating capacity of the former. This union can take many forms, the most popular of which are magnetic core-gold shell NPs (**figure 1.10 A**) and gold-decorated magnetic core-silica shell NPs (**figure 1.10 B**) (132,133). Despite the diverse architectures of these hybrids and the possibility of combining both magnetic and plasmonic properties for thermal therapy, most works explore only the plasmonic component for that purpose, to the detriment of the magnetic component. Apparently, the latter became more employed in the magnetic guidance of the nanosystem and in MRI (130).

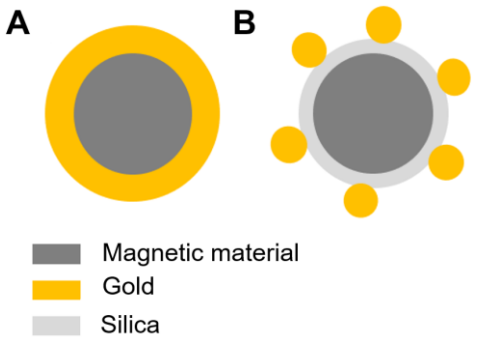

Figure 1.10 – Schematic representation of two of the most studied magnetoplasmonic nanocomposite architectures: magnetic core-gold shell NPs (A) and gold-decorated magnetic core-silica shell NPs (B).

1.3.3 Liposomes containing magnetic/plasmonic nanoparticles

Another achievement of bionanotechnology lies in the development of carriers that prolong therapeutics circulation time in the bloodstream, protecting them from biodegradation and delivering them to the desired location (150). Among these, liposomes have been widely applied to overcome drug delivery challenges (151,152).

In 1965, Bangham concluded that lipids arrange spontaneously in water in order to minimize Gibbs free energy, forming a spherical structure (153). Later, the term "liposome" came up, defining spherical vesicles with an aqueous nucleus surrounded by one or more phospholipid bilayers, which can vary in

terms of size, charge, lipid composition and lamellae number (154–157). These structures are promising for drug delivery because (i) they are made of materials that actually exist in the body, (ii) can be surface-modified with products that protect them from harsh environments and (iii) can be responsive to stimuli, such as, temperature and pH (150,158,159). As mentioned earlier, besides being drug carriers, liposomes can encapsulate MNPs, forming organic-inorganic nanohybrid particles – magnetoliposomes (MLs) – in order to stabilize them at physiological pH and avoid their degradation and aggregation (150,160–162). Two essential types of magnetoliposomes can be identified: aqueous MLs (AMLs), in which MNPs are trapped by liposomes, and solid MLs (SMLs), in which MNPs are covered by a lipid bilayer (74,163). The latter, although offering a better magnetic response, cannot include hydrophilic drugs. Of course, like MNPs, silica-coated magnetic/plasmonic nanoparticles can also be encapsulated by a lipid bilayer to be applied in cancer therapy. These nanosystems, besides reducing NP-APTES biophysical impact on cells in terms of membrane fluidity, cell movement and focal adhesion (164), can combine different imaging modalities for diagnosis and therapeutic strategies, such as, magnetic-guided drug delivery, magnetic hyperthermia, photothermia and photodynamic therapy (75,165). The drug release is promoted by lipid bilayer line defects and consequent increased permeability (166), which can take place in two ways: temperature increase above lipids phase transition temperature (T_m) because of NPs hysteresis losses or electromagnetic radiation absorption, and magneto-mechanical action, in which oscillating forces, generated under a low frequency AMF, increase membrane permeability to small molecules (166–168).

In disease treatment, especially in cancer, targeting and drug release control are extremely important. The first can occur passively or actively: passive targeting is based on the enhanced permeability and retention effect (EPR) and on the deficient structure of tumour-associated blood vessels, while active targeting happens when MLs targeting moieties (e.g., peptides, antibodies, and aptamers) attach to tumour cells surface (158,169). The latter is accomplished by composition tunning. For example, by changing MLs composition in terms of cholesterol and PEG content, lipid saturation and iron oxide MNPs size, Vlasova and co-workers studied low frequency AMF-induced dye release process (168). They found that polyethylene glycol (PEG) slightly decreases membrane disruption, stabilizing it. Contrarily, the MLs exposure to a non-heating AMF disturbs the lipid bilayer due to MNPs oscillatory movement (being equivalent to temperature-induced lipid phase transition), which promotes the release of loaded molecules. Interestingly, cholesterol and unsaturated lipids can be used to decrease drug release rate, as the deformations are more likely to heal (168). In fact, besides protecting and preserving NPs magnetic and plasmonic properties, MLs display a positive impact on drug pharmacokinetics (162,170).

1.4 MAGNETOGELS AND LIPOGELS

Nonetheless, the current need to overcome traditional chemotherapy low specificity in cancer treatment requires the design of even more sophisticated bionanostructures (171). Concerning this, magnetogels are seen as high-performance systems as they reduce drugs cytotoxicity and side-effects, improve drug delivery efficiency and retention time, and allow for MRI and hyperthermia. This is achieved through hydrogel-MNPs match, bringing together properties that individual materials do not have (17,171,172).

In these cases, which can involve polymeric network filling with MNP-concentrated suspensions, magnetization energy also depends on MNPs dipole-dipole interactions, which affects the heating capacity (173,174). The respective pointlike interaction is described as:

$$U_{DD} = -\frac{\mu_0}{4\pi}\left[3\frac{\left(\overrightarrow{m_i}\cdot\overrightarrow{r_{ij}}\right)\left(\overrightarrow{m_j}\cdot\overrightarrow{r_{ij}}\right)}{\left|r_{ij}\right|^5}+\frac{\overrightarrow{m_i}\cdot\overrightarrow{m_j}}{\left|r_{ij}\right|^3}\right] \qquad (1.10)$$

where $\overrightarrow{m}$ is the nanoparticle magnetic moment, r_{ij} represents the distance between the particle centre at positions i and j, connected by the vector $\overrightarrow{r_{ij}}$, and μ_0 corresponds to the vacuum magnetic permittivity (173). This interaction is meaningless when the dipole moment and the vector that connects the dipoles are co-aligned. In the absence of a magnetic field, interparticle interactions can lead to MNPs self-assembly in chains, multi-loops, cages, and rings, which can be controlled in bottom-up synthesis (e.g., through MNPs linking mechanism, size and spacing) (173,175,176). In ferrofluids under a magnetic field and weak shear flows, chain-like structures cause an increase in magnetization (the opposite occurring under strong shear flows), thereby affecting hyperthermia efficiency. Further, under an AMF and in high concentrations, monodisperse chain-assembled MNPs, presenting axial anisotropy, show larger hysteresis losses, which leads to higher heating efficiency in most angles between the field direction and the cluster anisotropy axis (173,177–179). On the other hand, the formation of random clusters can lead to a decrease in SLP, which can be bridged through the use of anisotropic particles or particles with higher saturation magnetization (173,178).

During the design of these composites, the physical features of each component may influence those of the other, such as MNPs' ability to rotate and gel's stimuli-responsive behaviour (180). In this regard, the interaction between gels and MNPs was studied by Bonhome-Espinosa (181). He characterized the change in hydrogel mechanical properties according to MNPs concentration. A considerable porosity and swelling capacity were found, as well as greater stiffness and viscoelastic moduli, in relation to non-magnetic materials. This concentration dependence is explained by the indirect attraction between

hydrogel monomers through MNPs and is proven by several studies (181). From another perspective, Soares *et al.* studied the effect of chitosan on iron oxide NPs magnetic and thermal properties. This widely studied polymer did not affect their magnetic properties since both composition and superparamagnetism were preserved, so they remained capable of generating heat under an AMF (182). Additional studies carried out by Villamin show the effect of pH on chitosan matrix-surrounded iron oxide NPs magnetic relaxation (183). Decreasing the pH, chitosan swelled as a result of NH_2 groups protonation. Now, if Néel relaxation time remains constant, it was proposed that swelling decreases Brownian relaxation time, which became the dominant relaxation process in this material; this translated into a shift in magnetic susceptibility imaginary part to higher frequencies (183). Actually, besides pH-promoted gel volume changes, it is very important to look at the AMF-induced polymeric network swelling/deswelling time scale. The kinetics of gel collapse and rearrangement must be optimized together with the heating rate and efficiency (especially in MNP-loaded temperature-responsive hydrogels), considering the limiting character of these phenomena to the nanosystem activity (180,184,185). Considering all this, it turns that it is possible to design multimodal materials able to respond to tissue microenvironment (internal) changes and that can be externally and spatiotemporally controlled by magnetic fields for chemo/hyperthermia therapy (180,186).

Alongside magnetogels, hydrogels combination with liposomes presents a long history, with Weiner having pioneered the introduction of these vesicles into a collagen matrix. He noted that liposome payloads release rate decreased in the presence of a hydrogel (187). Lipogels support thermodynamic stability of formulations, improve administration routes, and greatly increase drug-loading capacity (187–189). In addition to biopolymers, such as collagen, chitosan, gelatine, dextran, and alginate, it is worth mentioning the use of synthetic small self-assembling peptides, covered in section 1.2.1, as scaffold (188,190). For example, Wickremasinghe *et al.* placed cytokines and growth factors in liposomes embedded in an arginylglycylaspartic acid (RGD) adhesion sequence-incorporating hydrogel. With this architecture, the authors managed bimodal molecule release as liposomes delay cargo delivery and peptides are enzymatically degraded, enabling sustained molecules release (190,191). In another work, resveratrol-loaded liposomes were combined with a temperature-responsive hydrogel to repair damaged sciatic nerves in mice (192). The gels were formed at physiological temperature and allowed resveratrol diffusion after it passed through the lipid bilayer, showing a stable drug release *in vitro* and the repair of injured nerves *in vivo* (192).

These authors achieved promising results in controlled drug delivery because, as with magnetogels, incorporating liposomes in polymeric networks alters physical and biological properties of the materials (189,193). Hydrogel mechanical and rheological characteristics can also be improved by changing these soft NPs concentration (although to a lesser extent than with inorganic NPs), as they can interact with nanofibres or help with their crosslinking. In addition, liposomes make it possible to prolong drug release time and increase its accumulation in the desired location, compared to non-composite gels (193). In these materials, several complexation methods have already been studied in order to modulate drug release, for example by nanofibres degradation, Fickian diffusion or fusion of liposomes with plasma membrane (188,190). Thus, lipogels appear as interesting alternatives to overcome the liposomal instability in solution, as well as uncontrolled drug release, either from hydrogels with inappropriate mesh sizes or from magnetogels whose AMF-induced deswelling promotes burst release (180).

1.5 MAGNETOLIPOGELS: PROPERTIES, BIOMEDICAL APPLICATIONS, AND CURRENT STATE

Although magnetogels and lipogels allow the tuning and functionalization of hydrogel structure and properties (173), the former are difficult to stabilize and the latter lack external control. Thus, the introduction of lipid-coated MNPs (e.g., MLs) in a polymeric matrix is extremely attractive, as it offers several advantages over the nanosystems described above. In relation to magnetogels, magnetolipogels allow to amplify the loaded drug range (in virtue of lipids ability to incorporate both hydrophilic and hydrophobic molecules), increase their encapsulation efficiency, and prevent NPs leaching or aggregation (194,195). Regarding lipogels, magnetolipogels reinforce the spatiotemporal control of molecule release, considering the magnetically controlled system guidance, and the increase in lipid bilayer permeability by MH and/or magnetic mechanical action (173).

We can design several architectures for these composite nanosystems, e.g., inserting AMLs, SMLs or membrane-embedded MNPs in a hydrogel (**figure 1.11**). Although the latter enables a decrease in MNPs concentration due to the efficient destabilization of liposomes through their physical oscillation, it is necessary to coat them with hydrophobic molecules (196). On the other hand, the inclusion of hydrophilic MNPs within the liposome turns out to be simpler in terms of synthesis (196). Different constructions are already reported, such as, magnetogels-encapsulating vesicles and self-assembling NP-vesicle hydrogels, as Cogan performed (197,198). In her work, alginate hydrogels patterned with aggregates of iron oxide NPs and $NiCl_2$ containing-dipalmitoylphosphatidylcholine (DPPC) vesicles were

developed and the response of cultured fibroblasts to nickel (II) release was followed (197). It was found that the magnetolipogel supported fibroblasts growth and only the AMF-induced nickel (II) release caused cell apoptosis in the gel, giving spatial and temporal control of cell behaviour (197). Although nickel has interesting magnetic properties, it is cytotoxic, so it was applied as a cell apoptosis inducing agent in this study. The truth is that iron oxide-based crystalline NPs are the most used MNPs in the first steps of these complex systems development because, in addition to their good magnetic properties, they exhibit low production costs, environmental safety, low toxicity, diversity and the ability to enhance pharmaceutical activity and tumour targeting (199–201). The major handicap lies in their propensity to aggregate and oxidize, which, in magnetolipogels, is filled by its functionalization with hydrogelators, gel-incorporated phospholipids and eventually surfactants and biomolecules (201,202).

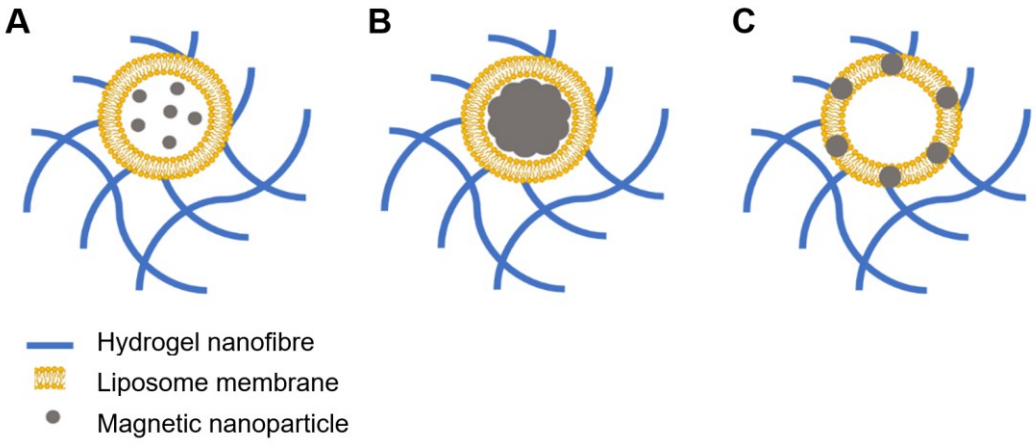

Figure 1.11 – Some possible architectures for magnetolipogels: hydrogel-incorporated-AMLs (A), -SMLs (B) and -membrane-embedded MNPs (C).

Alginate-based magnetic lipogels are, in fact, the most reported. They have been tested for several applications (203), mainly in the field of biomedicine, since they can support all functional components in a single composite system and allow easy liposome-encapsulated payloads diffusion, if necessary (204). For example, to visualize drug release by real-time MRI, Elk and co-workers prepared an alginate microgel loaded with [Gd(HPDO3A)-(H_2O)]-containing liposomes and T2 contrast agents (holmium ions) that allow microgel monitoring in all treatment states (205). It was found that the payloads were quickly released after hyperthermia; moreover, the utility of [Gd(HPDO3A)-(H_2O)] for following liposome-encapsulated drug release *in vivo* is anticipated (205). Earlier, in 2009, alginate hydrogel-supported vesicle assemblies allowed the direct conversion of electrical signals into chemicals, with Fe_3O_4 NPs as intermediates; this culminated in the release of vesicle-encapsulated carboxyfluorescein, upon a quite low AMF (392 kHz) (206). In addition to the possibility of magnetic

guidance, this system also demonstrated the ability to host membrane-bound biomolecules, which makes it useful for stem cells culture (206).

Despite the possible application of magnetogels in imaging and tissue engineering, the present work is essentially concerned with controlled drug delivery and hyperthermia for cancer treatment. It is well known that drug release within a therapeutic dose window to a specific location and time increases the drug efficiency and decreases its side effects, since only the targeted tissue is exposed to therapy (207). Considering this, in a highly sophisticated approach, Ullrich managed to control an enzymatic reaction for the delivery of unstable substances (208). Again, alginate was used as a scaffold, taking into account its usefulness in liposome incorporation and enzyme immobilization (209,210). Furthermore, the author took advantage of liposomes ability to release molecules upon rising temperatures. The heating was achieved by MNPs, which acted as converters of radiofrequency fields into biochemical signals by inducing liposomes phase transition. At low temperatures, the bilayer is rigid and has low permeability to hydrophilic molecules; when the melting temperature (T_m) is reached, the membrane melts in a more fluid state and becomes more permeable (208). As liposomes show a reversible phase transition, when the heating is interrupted, the release of reagent into the alginate matrix breaks off, which offers control at several levels over the enzymatic reaction (208). Although ink-jet printing technique is the most used technology to produce these structures, mainly in the form of microgels (where liposomes and MNPs can be independently adjusted) (173,196), an innovative method for their production was reported five years ago, involving microfluidics, and using extractive gelation (204). Herewith, it was possible to produce alginate hydrogel microparticles containing MNPs and DPPC/Cholesterol-monodispersed liposomes, with controlled diameter (<10 μm). Microparticles purification was achieved by magnetic separation, which has already been a breakthrough in this area; as the concentration of all components (hydrogelator polymer, liposomes and MNPs) was optimized, the final structures proved to be exceptionally stable, besides being magneto and thermoresponsive (204).

The consensus of alginate regarding the design and synthesis of these nanostructures is undeniable, however, it was found that this biopolymer reduces liposomes stability against leakage in traditional syntheses, especially those consisting of phosphatidylcholine (173,196). Chitosan can work as an alternative, once it is an excellent liposome reservoir and offers a diffusion barrier, unlike alginate (207). In this follow-up, the incorporation of iron oxide NPs and DOX-containing DPPC liposomes into a hydrophobically modified chitosan gel has already been described. As in previous studies, liposomes thermal sensitivity combined with the AMF-induced heating allowed to deliberately release DOX. This

study demonstrated that even small amounts of iron oxide NPs are sufficient to trigger drug release, with changes appearing only in liposomes, leaving the gel intact (207).

Still, being highly versatile materials with several advantages over polymeric matrices (211,212), more attention should be paid to supramolecular hydrogels in the development of magnetic lipogels. Veloso *et al*. incorporated both SMLs and AMLs into three different hydrogels based on peptides *N*-capped with the nonsteroidal anti-inflammatory drug naproxen (Npx) (Npx-L-Phe-*Z*-ΔAbu-OH, Npx-L-Phe-*Z*-ΔPhe-OH and Npx-L-Ala-*Z*-ΔPhe-GRGDG-OH), all suitable for drug delivery (194). Hydrogelation was promoted by changing pH, according to the process suggested by the authors (**figure 1.12**). Interestingly, the peptide network showed cavities capable of accommodating drugs, which are convenient to circumvent premature drug release from MLs (194). Very recently, the same team aimed to minimize MNPs coating impact on gelation, as the use of thick coatings involves an increase in hydrogelator concentration and a decrease in MNPs heating efficiency (213). To this end, they studied the influence of manganese ferrite NPs lipid functionalization in a peptide hydrogel (Cbz-L-Met-*Z*-ΔPhe-OH) since lipids offer steric stabilization and hydrophobic zones, useful for drug storage in the matrix. MNPs concentration and distribution were enhanced, and their magnetic properties were shown to be potentiated in the gel, particularly the heating efficiency. There was also a reproducible DOX release upon an AMF, which encourages to keep seeking for magnetic conduction, MH, and controlled drug delivery in a single nanosystem (213).

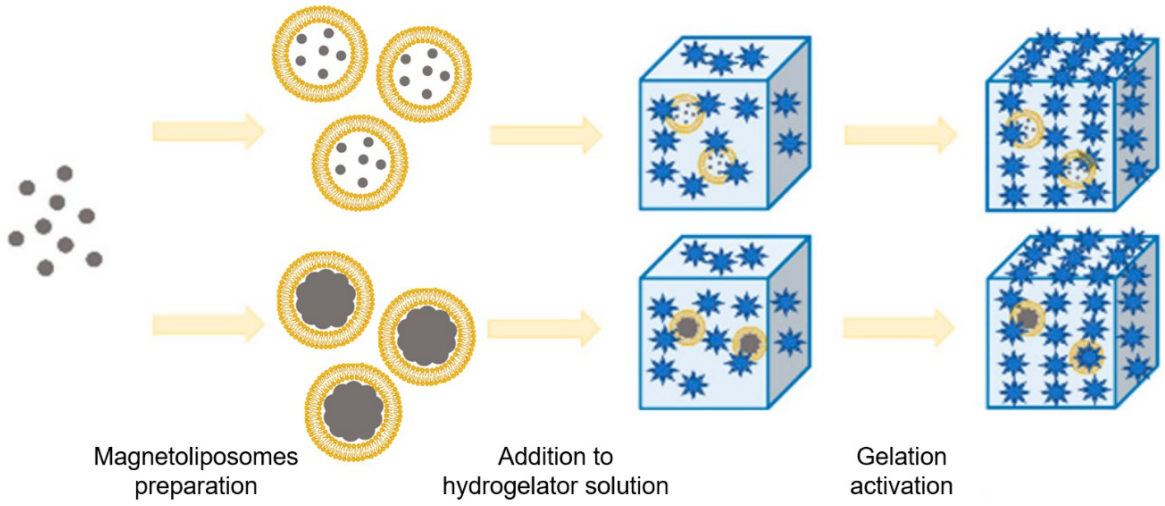

Figure 1.12 – Representation of the strategy used for supramolecular magnetolipogel synthesis. Adapted from [194].

Considering this, in an ambitious work, we have brought together the advantages and applications of several materials in order to develop a multifunctional plasmonic magnetolipogel for multimodal cancer therapy. We started by synthesizing two novel lysine dehydrodipeptides (**figure 1.13**), different in the

C-terminus residue – dehydroaminobutyric acid (ΔAbu, compound **1**) and dehydrophenylalanine (ΔPhe, compound **2**).

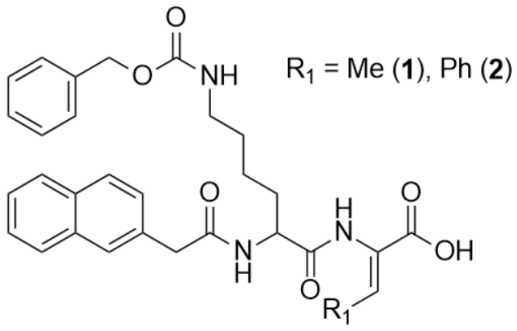

Figure 1.13 – Schematic representation of the synthesised hydrogelators Nap-L-Lys(Cbz)-Z-ΔAbu-OH (compound **1**) and Nap-L-Lys(Cbz)-Z-ΔPhe-OH (compound **2**).

The latter, along with the *N*-capping groups, enhance hydrophobic interactions and stacking between the aromatic moieties of the molecules, favouring gelation. Moreover, naphthalene (Nap) allows following dynamic processes, such as monomer aggregation, thanks to its intrinsic fluorescence. Next, aqueous plasmonic magnetoliposomes were produced; we chose to synthesize core/shell $MnFe_2O_4$/gold nanoparticles because, in addition to the applications reported so far, this geometry allows to decrease the reactivity of the magnetic material (increasing the stability of the overall particle) and provides surface chemistry for further functionalization (214). After selecting the convenient hydrogelator, the magnetolipogels were assembled using the strategy addressed in (194) and the system was evaluated as a platform for controlled drug delivery. Here, 5(6)-carboxyfluorescein – used as a model drug because of its useful fluorescence quantum yield (215) – was encapsulated and its release from the hydrogel and magnetolipogel matrices was monitored for three days.

Chapter 2

EXPERIMENTAL PROCEDURES

2.1 SYNTHESIS

2.1.1 Dehydrodipeptide hydrogelators

Compounds **1** and **2** were fully characterized by ^{1}H and ^{13}C nuclear magnetic resonance (NMR) spectroscopies and high-resolution mass spectrometry (HR-MS). Spectra were collected on a Bruker Avance III 400 spectrometer (with deuterated dimethyl sulfoxide (DMSO-*d*$_6$) as solvent), operating at 400.13 MHz and 100.62 MHz, for ^{1}H and ^{13}C NMR, respectively. HRMS data were obtained from the mass spectrometry service of University of Vigo, Spain.

2.1.1.1 *N*-2-naphthylacetyl-L-lysyl(*N*-benzyloxycarbonyl)-*Z*-dehydroaminobutyric acid (Nap-L-Lys(Cbz)-*Z*-ΔAbu-OH) (compound 1)

Synthesis of the methyl ester of threonine [H-L-Thr-OMe (3)]. Threonine [H-L-Thr-OH] (2.98 g, 25 mmol) was added to 40 mL of methanol in an ice bath. Thionyl chloride (3.4 equiv, 6.17 mL) was added dropwise, and the reaction mixture was left stirring for 4 h at 40 °C. The solvent was removed under reduced pressure and ethyl ether was added. The process was repeated until a yellow oil of compound **3** was formed (3.99 g, 94.1 %).

^{1}H NMR (400 MHz, DMSO-*d*$_6$) δ (ppm): 1.183-1.199 (3H, d, *J* = 6.4 Hz, γ-C*H*$_3$ Thr); 3.732 (3H, s, OC*H*$_3$); 3.915 (1H, br s, α-C*H* Thr); 4.098-4.125 (1H, m, β-C*H* Thr); 5.630 (1H, s, β-O*H* Thr); 8.399 (3H, br s, N*H*$_3^+$ Thr).

Synthesis of the methyl ester of *N*-*tert*-butyloxycarbonyl-L-lysyl(*N*-benzyloxycarbonyl)-D,L-threonine [Boc-L-Lys(Cbz)-D,L-Thr-OMe (5)]. Boc-L-Lys(Cbz)-OH (**4**) (1.14 g, 3 mmol) was dissolved in acetonitrile (7 mL) in an ice bath. *N,N,N′,N′*-tetramethyl-*O*-(1*H*-benzotriazol-1-yl)uronium hexafluorophosphate (HBTU) (1.10 equiv, 1.25 g, 3.3 mmol), H-L-Thr-OMe (1.00 equiv, 0.51 g, 3 mmol) and triethylamine (3.00 equiv, 1.25 mL, 9 mmol) were added. The mixture was left stirring at room temperature overnight. The solvent was removed under reduced pressure, resulting in a residue that was partitioned between ethyl acetate (25 mL) and $KHSO_4$ (1 M, 25 mL). The organic phase was carefully washed with $KHSO_4$ (1 M, 2 × 25 mL), $NaHCO_3$ (1 M, 2 × 25 mL) and brine (1 × 35 mL) and dried with $MgSO_4$. Removal of the solvent afforded compound **5** as a diastereomeric mixture (1.05 g, 70.6%).

^{1}H NMR (400 MHz, DMSO-*d*$_6$) δ (ppm): 1.036 (3H, d, *J* = 6.4 Hz, γ-C*H*$_3$ Thr); 1.145-1.319 (2H, m, γ-C*H*$_2$ Lys); 1.366 (3H, s, 3×C*H*$_3$ Boc); 1.477 (2H, d, *J* = 8.8 Hz, δ-C*H*$_2$ Lys); 1.603 (2H, d, *J* = 6.0 Hz, β-C*H*$_2$ Lys); 2.948 (2H, t, *J* = 6.4 Hz, ε-C*H*$_2$ Lys); 3.331 (3H, s, OC*H*$_3$ Thr); 3.956-4.128 (2H, m, α-C*H* Lys + α-C*H* Thr); 4.274 (1H, q, *J* = 3.2 Hz, β-C*H* Thr); 4.988 (3H, s, C*H*$_2$ Cbz + β-O*H* Thr); 6.953 (1H,

d, *J* = 8.4 Hz, α-N*H* Lys); 7.201 (1H, t, *J* = 5.6 Hz, ξ-N*H* Lys); 7.274-7.374 (5H, m, Ar*H* Cbz); 7.691 (1H, d, *J* = 8.4 Hz, N*H* Thr).

Synthesis of the methyl ester of *N*-*tert*-butyloxycarbonyl-L-lysyl(*N*-benzyloxycarbonyl)-*Z*-dehydroaminobutyric acid [Boc-L-Lys(Cbz)-*Z*-ΔAbu-OMe (6)]. To a solution of compound **5** (1.05 g, 2.12 mmol) in dry acetonitrile (5 mL), *N,N*-dimethylpyridin-4-amine (DMAP) (0.11 equiv, 0.029 g, 0.23 mmol) and di-*tert*-butyl dicarbonate (Boc_2O) (1.1 equiv, 0.51 g, 2.33 mmol) were added under stirring at room temperature. The mixture was monitored by ^{1}H NMR until all reactant was consumed. *N,N,N',N'*-tetramethylguadinine (TMG) (2% in volume, 0.1 mL) was added under continuous stirring. The mixture was left stirring at room temperature and monitored by ^{1}H NMR until all reactant was consumed. Evaporation at reduced pressure gave a residue that was partitioned between ethyl acetate (25 mL) and $KHSO_4$ (1 M, 25 mL), washed with $KHSO_4$ (1 M, 2 × 25 mL), $NaHCO_3$ (1 M, 2 × 25 mL) and brine (1 × 30 mL) and dried with $MgSO_4$. Removal of the solvent afforded compound **6** (0.62 g, 61.3%).

^{1}H NMR (400 MHz, DMSO-d_6) δ (ppm): 1.362-1.605 (15H, m, γ-CH_2 Lys + 3×CH_3 Boc + δ-CH_2 + β-CH_2 Lys); 1.645 (3H, d, *J* = 7.2 Hz, γ-CH_3 ΔAbu); 2.985 (2H, t, *J* = 6.4 Hz, ε-CH_2 Lys); 3.583 (3H, s, OCH_3 ΔAbu); 3.999 (1H, d, *J* = 4.8 Hz, α-C*H* Lys); 4.988 (2H, s, CH_2 Cbz); 6.509 (1H, q, *J* = 7.2 Hz, β-C*H* ΔAbu); 6.832 (1H, d, *J* = 8.0 Hz, α-N*H* Lys); 7.210 (1H, t, ξ-N*H* Lys); 7.290-7.373 (5H, m, Ar*H* Cbz); 9.116 (1H, s, N*H* ΔAbu).

Synthesis of the methyl ester of lysyl(*N*-benzyloxycarbonyl)-*Z*-dehydroaminobutyric acid [H-L-Lys(Cbz)-*Z*-ΔAbu-OMe (7)]. Trifluoroacetic acid (TFA) (2 mL, 26.14 mmol) was added to Boc-L-Lys(Cbz)-*Z*-ΔAbu-OMe (0.62 g, 1.30 mmol), and the mixture was left stirring 1 h at room temperature. TFA was removed under reduced pressure and ethyl ether was added. The solvent was removed under reduced pressure and the process was repeated until a white solid of compound **7** was formed (0.61 g, 95.5%).

^{1}H NMR (400 MHz, DMSO-d_6) δ (ppm): 1.362-1.447 (4H, m, γ-CH_2 Lys + δ-CH_2 Lys); 1.695-1.781 (5H, m, β-CH_2 Lys + γ-CH_3 ΔAbu); 2.994 (2H, t, *J* = 6.4 Hz, ε-CH_2 Lys); 3.645 (3H, s, OCH_3 ΔAbu); 3.902 (1H, d, *J* = 5.6 Hz, α-C*H* Lys); 4.987 (2H, s, CH_2 Cbz); 6.643 (1H, q, *J* = 7.2 Hz, β-C*H* ΔAbu); 7.213 (1H, t, *J* = 5.6 Hz, ξ-N*H* Lys); 7.310-7.335 (5H, m, Ar*H* Cbz); 8.153 (3H, s, α-NH_3^+ Lys); 9.747 (1H, s, N*H* ΔAbu).

Synthesis of the methyl ester of *N*-2-naphthylacetyl-L-lysyl(*N*-benzyloxycarbonyl)-*Z*-dehydroaminobutyric acid [Nap-L-Lys(Cbz)-*Z*-ΔAbu-OMe (8)]. H-L-Lys(Cbz)-*Z*-ΔAbu-OMe (0.61 g,

1.24 mmol) was dissolved in acetonitrile (4 mL) in an ice bath. HBTU (1.10 equiv, 0.52 g, 1.36 mmol), 2-naphthaleneacetic acid (1.00 equiv, 0.23 g, 1.24 mmol) and triethylamine (3.00 equiv, 0.52 mL, 3.72 mmol) were added. The mixture was left stirring at room temperature overnight. The solid was filtered under reduced pressure, washed with $KHSO_4$ (1 M, 2 × 12 mL), $NaHCO_3$ (1 M, 2 × 12 mL) and brine (2 × 12 mL) and identified as Nap-L-Lys(Cbz)-*Z*-ΔAbu-OMe (0.65 g, 96.1%).

^{1}H NMR (400 MHz, DMSO-*d*$_6$) δ (ppm): 1.304-1.416 (4H, m, γ-C*H*$_2$ Lys + δ-C*H*$_2$ Lys); 1.601-1.704 (5H, m, β-C*H*$_2$ Lys + γ-C*H*$_3$ ΔAbu); 2.941 (2H, t, *J* = 6.4 Hz, ε-C*H*$_2$ Lys); 3.602 (3H, s, OC*H*$_3$ ΔAbu); 3.650 (2H, d, *J* = 1.6 Hz, C*H*$_2$ Nap); 4.340-4.395 (1H, m, α-C*H* Lys); 4.989 (2H, s, C*H*$_2$ Cbz); 6.507 (1H, q, *J* = 7.2 Hz, β-C*H* ΔAbu); 7.201 (1H, t, *J* = 5.6 Hz, ξ-N*H* Lys); 7.309-7.348 (5H, m, Ar*H* Cbz); 7.414-7.858 (7H, m, Ar*H* Nap); 8.317 (1H, d, *J* = 8.0 Hz, α-N*H* Lys); 9.274 (1H, s, N*H* ΔAbu).

^{13}C NMR (100.6 MHz, DMSO-*d*$_6$) δ (ppm): 13.41 (CH_3, γ-*C*H$_3$ ΔAbu); 22.54 (CH_2, γ-*C*H$_2$ Lys); 29.16 (CH_2, δ-*C*H$_2$ Lys); 31.88 (CH_2, β-*C*H$_2$ Lys); 40.22 (CH_2, ε-*C*H$_2$ Lys); 42.17 (CH_2, *C*H$_2$ Nap); 51.81 (CH_3, O*C*H$_3$ ΔAbu); 52.56 (CH, α-*C*H Lys); 65.16 (CH_2, *C*H$_2$ Cbz); 125.51 (CH, *C*H Nap); 126.07 (CH, *C*H Nap); 127.31 (CH, *C*H Nap); 127.37 (CH, *C*H Nap); 127.49 (CH, *C*H Nap); 127.55 (CH, *C*H Nap); 127.67 (CH, *C*H Cbz); 127.72 (C, α-*C* ΔAbu); 127.75 (CH, *C*H Cbz); 127.78 (CH, *C*H Nap); 128.39 (CH, *C*H Cbz); 131.78 (C, *C* Nap); 132.58 (CH, β-*C*H ΔAbu); 133.00 (C, *C* Nap); 134.19 (C, *C* Nap); 137.29 (C, *C* Cbz); 156.14 (C, *C*=O Cbz); 164.58 (C, *C*=O ΔAbu); 170.15 (C, *C*=O Lys); 170.99 (C, *C*=O Nap).

Synthesis of *N*-2-naphthylacetyl-L-lysyl(*N*-benzyloxycarbonyl)-*Z*-dehydroaminobutyric acid [Nap-L-Lys(Cbz)-*Z*-ΔAbu-OH (1)]. Compound **8** (0.65 g, 1.19 mmol) was dissolved in 1,4-dioxane (10 mL) and a solution of NaOH 1 M (1.5 equiv, 1.79 mL) was added. The reaction was followed by thin-layer chromatography (TLC) until no starting material was detected. The organic solvent was removed under reduced pressure, and the reaction mixture was acidified to pH 2 – 3 with $KHSO_4$ (1 M). The solid was filtered and identified as Nap-L-Lys(Cbz)-*Z*-ΔAbu-OH (0,41 g, 64.7%) The synthetic procedure was adapted from previous works (20,216).

^{1}H NMR (400 MHz, DMSO-*d*$_6$) δ (ppm): 1.297-1.404 (4H, m, γ-C*H*$_2$ Lys + δ-C*H*$_2$ Lys), 1.573-1.705 (5H, m, β-C*H*$_2$ Lys + γ-C*H*$_3$ ΔAbu); 2.937 (2H, q, *J* = 6.4 Hz, ε-C*H*$_2$ Lys); 3.652 (2H, dd, *J* = 18.0 Hz and *J* = 14.0 Hz, C*H*$_2$ Nap); 4.352-4.407 (1H, m, α-C*H* Lys); 4.990 (2H, s, C*H*$_2$ Cbz); 6.528 (1H, q, *J* = 7.2 Hz, β-C*H* ΔAbu); 7.194 (1H, t, *J* = 5.6 Hz, ξ-N*H* Lys); 7.327-7.349 (5H, m, Ar*H* Cbz);

7.457-7.834 (7H, m, Ar*H* Nap); 8.291 (1H, d, *J* = 8.0 Hz, α-N*H* Lys); 9.103 (1H, s, N*H* ΔAbu); 11.521 (1H, s, CO_2H ΔAbu).

^{13}C NMR (100.6 MHz, DMSO-d_6) δ (ppm): 13.61 (CH_3, γ-*C*H_3 ΔAbu); 22.61 (CH_2, γ-*C*H_2 Lys); 29.14 (CH_2, δ-*C*H_2 Lys); 31.97 (CH_2, β-*C*H_2 Lys); 40.21 (CH_2, ε-*C*H_2 Lys); 42.18 (CH_2, *C*H_2 Nap); 52.54 (CH, α-*C*H Lys); 65.14 (CH_2, *C*H_2 Cbz); 125.49 (CH, *C*H Nap); 126.05 (CH, *C*H Nap); 127.29 (CH, *C*H Nap); 127.36 (CH, *C*H Nap); 127.48 (CH, *C*H Nap); 127.54 (CH, *C*H Nap); 127.66 (CH, *C*H Cbz); 127.74 (CH, *C*H Cbz); 127.77 (CH, *C*H Nap) ; 128.21 (C, α-*C* ΔAbu); 128.37 (CH, *C*H Cbz); 131.76 (C, *C* Nap); 132.23 (CH, β-*C*H ΔAbu); 132.99 (C, *C* Nap); 134.20 (C, *C* Nap); 137.29 (C, *C* Cbz); 156.10 (C, *C*=O Cbz); 165.46 (C, *C*=O ΔAbu); 170.11 (C, *C*=O Lys); 170.64 (C, *C*=O Nap).

HR-MS (ESI) *m/z*: $[M + H]^+$ calcd for $C_{30}H_{34}N_3O_6$: 532.24; found: 532.2415.

2.1.1.2 *N*-2-naphthylacetyl-L-lysyl(*N*-benzyloxycarbonyl)-*Z*-dehydrophenylalanine (Nap-L-Lys(Cbz)-*Z*-ΔPhe-OH) (compound 2)

Synthesis of the methyl ester of β-hydroxyphenylalanine [H-D,L-Phe(*β*-OH)-OMe (9)]. β-hydroxyphenylalanine [H-D,L-Phe(β-OH)-OH] (4.53 g, 25 mmol) was added to 40 mL of methanol in an ice bath. Thionyl chloride (3.4 equiv, 6.17 mL) was added dropwise, and the reaction mixture was left stirring for 4 h at 40 °C. The solvent was removed under reduced pressure and ethyl ether was added. The process was repeated until a white solid of compound **9** was formed (4.72 g, 81.5%).

^{1}H NMR (400 MHz, DMSO-d_6) δ (ppm): 3.568 (3H, s, OC*H*$_3$); 4.097 [1H, d, *J* = 5.6 Hz, α-C*H* Phe(β-OH)]; 5.002 [1H, d, *J* = 5.6 Hz, β-C*H* Phe(β-OH)]; 6.555 [1H, s, β-O*H* Phe(β-OH)]; 7.303-7.385 [5H, m, Ar*H* Phe(β-OH)]; 8.594 [3H, s, N*H*$_3^+$ Phe(β-OH)].

Synthesis of the methyl ester of *N-tert*-butyloxycarbonyl-L-lysyl(*N*-benzyloxycarbonyl)-D,L-*β*-hydroxyphenylalanine [Boc-L-Lys(Cbz)-D,L-Phe(*β*-OH)-OMe (10)]. Boc-L-Lys(Cbz)-OH (**4**) (1.14 g, 3 mmol) was dissolved in acetonitrile (7 mL) in an ice bath. HBTU (1.10 equiv, 1.25 g, 3.3 mmol), H-D,L-Phe(β-OH)-OMe (1.00 equiv, 0.70 g, 3 mmol) and triethylamine (3.00 equiv, 1.25 mL, 9 mmol) were added. The mixture was left stirring at room temperature overnight. The solvent was removed under reduced pressure, resulting in a residue that was partitioned between ethyl acetate (25 mL) and $KHSO_4$ (1 M, 25 mL). The organic phase was carefully washed with $KHSO_4$ (1 M, 2 × 25 mL), $NaHCO_3$ (1 M, 2 × 25 mL) and brine (1 × 35 mL) and dried with $MgSO_4$. Removal of the solvent afforded compound **10** as a diastereomeric mixture (1.54 g, 92.1%).

^{1}H NMR (400 MHz, DMSO-*d*$_6$) δ (ppm): 0.996 (2H, s, γ-C*H*$_2$ Lys); 1.312-1.373 (13H, m, 3×C*H*$_3$ Boc + δ-C*H*$_2$ Lys + β-C*H*$_2$ Lys); 2.886 (2H, t, *J* = 6.4 Hz, ε-C*H*$_2$ Lys); 3.598 and 3.637 [3H, 2 s, OC*H*$_3$ Phe(β-OH)]; 3.805-3.920 (1H, m, α-C*H* Lys); 4.547 [1H, t, *J* = 5.2 Hz, α-C*H* Phe(β-OH)]; 4.993 (2H, s, C*H*$_2$ Cbz); 5.119 [1H, q, *J* = 4.8 Hz, β-O*H* Phe(β-OH)]; 5.917 [1H, t, *J* = 6.4 Hz, β-C*H* Phe (β-OH)]; 6.964 (1H, d, *J* = 8.0 Hz, α-N*H* Lys); 7.181-7.367 [11H, m, ξ-N*H* Lys + Ar*H* Cbz + Ar*H* Phe(β-OH)]; 7.744 [1H, d, *J* = 8.4 Hz, N*H* Phe(β-OH)].

Synthesis of the methyl ester of *N*-*tert*-butyloxycarbonyl-L-lysyl(*N*-benzyloxycarbonyl)-*Z*-dehydrophenylalanine [Boc-L-Lys(Cbz)-*Z*-ΔPhe-OMe (11)]. To a solution of compound **10** (1.54 g, 2.76 mmol) in dry acetonitrile (5 mL), DMAP (0.11 equiv, 0.037 g, 0.30 mmol) and Boc_2O (1.1 equiv, 0.66 g, 3.04 mmol) were added under stirring at room temperature. The mixture was monitored by ^{1}H NMR until all reactant was consumed. *N,N,N',N'*-tetramethylguadinine (2% in volume, 0.1 mL) was added under continuous stirring. The mixture was left stirring at room temperature and monitored by ^{1}H NMR until all reactant was consumed. Evaporation at reduced pressure gave a residue that was partitioned between ethyl acetate (25 mL) and $KHSO_4$ (1 M, 25 mL), washed with $KHSO_4$ (1 M, 2 × 25 mL), $NaHCO_3$ (1 M, 3 × 25 mL) and brine (1 × 30 mL) and dried with $MgSO_4$. Removal of the solvent afforded compound **11** (1.06 g, 71.0%).

^{1}H NMR (400 MHz, DMSO-*d*$_6$) δ (ppm): 1.372-1.574 (13H, m, *J* = 8.0 Hz, γ-C*H*$_2$ Lys + 3×C*H*$_3$ Boc + δ-C*H*$_2$ Lys); 1.540-1.669 (2H, m, β-C*H*$_2$ Lys); 2.970 (2H, t, *J* = 6.4 Hz, ε-C*H*$_2$ Lys); 3.671 (3H, s, OC*H*$_3$ ΔPhe); 3.990-4.051 (1H, m, α-C*H* Lys); 4.990 (2H, s, C*H*$_2$ Cbz); 6.939 (1H, d, *J* = 8.0 Hz, α-N*H* Lys); 7.221 (1H, s, β-C*H* ΔPhe); 7.290-7.370 (10H, m, Ar*H* Cbz + Ar*H* ΔPhe); 7.684 (1H, t, *J* = 3.6 Hz, ξ-N*H* Lys); 9.591 (1H, s, N*H* ΔPhe).

Synthesis of the methyl ester of lysyl(*N*-benzyloxycarbonyl)-*Z*-dehydrophenylalanine [H-L-Lys(Cbz)-*Z*-ΔPhe-OMe (12)]. TFA (2 mL, 26.14 mmol) was added to Boc-L-Lys(Cbz)-*Z*-ΔPhe-OMe (1.06 g, 1.96 mmol), and the mixture was left stirring 1 h at room temperature. TFA was removed under reduced pressure and ethyl ether was added. The solvent was removed under reduced pressure and the process was repeated until a white solid of compound **12** was formed (1.01 g, 93.1%).

^{1}H NMR (400 MHz, DMSO-*d*$_6$) δ (ppm): 1.369-1.457 (4H, m, γ-C*H*$_2$ Lys + δ-C*H*$_2$ Lys); 1.803 (2H, d, *J* = 6.4 Hz, β-C*H*$_2$ Lys); 2.983 (2H, t, *J* = 6.4 Hz, ε-C*H*$_2$ Lys); 3.709 (3H, s, OC*H*$_3$ ΔPhe); 3.967 (1H, d, *J* = 5.2 Hz, α-C*H* Lys); 4.988 (2H, s, C*H*$_2$ Cbz); 7.225 (1H, t, *J* = 5.6 Hz, ξ-N*H* Lys); 7.297-7.657 (11H, m, β-C*H* ΔPhe + Ar*H* Cbz + Ar*H* ΔPhe); 8.175 (3H, s, α-N*H*$_3^+$ Lys); 10.164 (1H, s, N*H* ΔPhe).

Synthesis of the methyl ester of *N*-2-naphthylacetyl-L-lysyl(*N*-benzyloxycarbonyl)-*Z*-dehydrophenylalanine [Nap-L-Lys(Cbz)-*Z*-ΔPhe-OMe (13)]. H-L-Lys(Cbz)-*Z*-ΔPhe-OMe (1.01 g, 1.82 mmol) was dissolved in acetonitrile (5 mL) in an ice bath. HBTU (1.10 equiv, 0.76 g, 2.00 mmol), 2-naphthaleneacetic acid (1.00 equiv, 0.34 g, 1.82 mmol) and triethylamine (3.00 equiv, 0.76 mL, 5.46 mmol) were added. The mixture was left stirring at room temperature overnight. The solid was filtered under reduced pressure, washed with $KHSO_4$ (1 M, 2 × 12 mL), $NaHCO_3$ (1 M, 2 × 12 mL) and brine (2 × 12 mL) and identified as Nap-L-Lys(Cbz)-*Z*-ΔPhe-OMe (0.77 g, 69.8%).

^{1}H NMR (400 MHz, DMSO-d_6) δ (ppm): 1.331-1.433 (4H, m, γ-CH_2 Lys + δ-CH_2 Lys); 1.575-1.754 (2H, m, β-CH_2 Lys); 2.962 (2H, q, J = 6.4 Hz, ε-CH_2 Lys); 3.664 (3H, s, OCH_3 ΔPhe); 3.679 (2H, s, CH_2 Nap); 4.379 (1H, t, J = 5.6 Hz, α-CH Lys); 4.991 (2H, s, CH_2 Cbz); 7.220 (1H, s, β-CH ΔPhe); 7.265-7.346 (10H, m, ArH Cbz + ArH ΔPhe); 7.457-7.826 (8H, m, ξ-NH Lys + ArH Nap); 8.391 (1H, d, J = 7.6 Hz, α-NH Lys); 9.742 (1H, s, NH ΔPhe).

^{13}C NMR (100.6 MHz, DMSO-d_6) δ (ppm): 22.53 (CH_2, γ-CH$_2$ Lys); 29.18 (CH_2, δ-CH$_2$ Lys); 31.33 (CH_2, β-CH$_2$ Lys); 40.22 (CH_2, ε-CH$_2$ Lys); 42.10 (CH_2, CH$_2$ Nap); 52.12 (CH_3, OCH$_3$ ΔPhe); 52.64 (CH, α-CH Lys); 65.15 (CH_2, CH$_2$ Cbz); 125.48 (CH, CH Nap); 125.94 (C, α-C ΔPhe); 126.03 (CH, CH Nap); 127.30 (CH, CH Nap); 127.36 (CH, CH Nap); 127.47 (CH, CH Nap); 127.53 (CH, CH Nap); 127.66 (CH, CH Cbz); 127.74 (CH, CH Cbz); 128.36 (CH, CH Cbz) ; 128.50 (CH, CH Nap); 128.65 (CH, CH ΔPhe); 129.39 (CH, CH ΔPhe); 130.09 (CH, CH ΔPhe); 131.77 (C, C Nap); 132.10 (CH, β-CH ΔPhe); 132.99 (C, C Nap); 133.21 (C, C ΔPhe); 134.14 (C, C Nap); 137.27 (C, C Cbz); 156.11 (C, C=O Cbz); 165.35 (C, C=O ΔPhe); 170.21 (C, C=O Lys); 171.93 (C, C=O Nap).

Synthesis of *N*-2-naphthylacetyl-L-lysyl(*N*-benzyloxycarbonyl)-*Z*-dehydrophenylalanine [Nap-L-Lys(Cbz)-*Z*-ΔPhe-OH (2)]. Compound **13** (0.77 g, 1.27 mmol) was dissolved in 1,4-dioxane (10 mL) and a solution of NaOH 1 M (1.5 equiv, 1.91 mL) was added. The reaction was followed by TLC until no starting material was detected. The organic solvent was removed under reduced pressure, and the reaction mixture was acidified to pH 2 – 3 with $KHSO_4$ (1 M). The solid was filtered and identified as Nap-L-Lys(Cbz)-*Z*-ΔPhe-OH (0.65 g, 86.2%).

^{1}H NMR (400 MHz, DMSO-d_6) δ (ppm): 1.319-1.416 (4H, m, γ-CH_2 Lys + δ-CH_2 Lys); 1.579-1.751 (2H, m, β-CH_2 Lys); 2.947 (2H, q, J = 6.4 Hz, ε-CH_2 Lys); 3.672 (2H, dd, J = 14.0 Hz and J = 21.2 Hz, CH_2 Nap); 4.360-4.414 (1H, m, α-CH Lys); 4.993 (2H, s, CH_2 Cbz); 7.199-7.347 (11H, m, β-CH ΔPhe +

Ar*H* Cbz + Ar*H* ΔPhe); 7.436-7.859 (8H, m, ξ-N*H* Lys + Ar*H* Nap); 8.363 (1H, d, *J* = 7.6 Hz, α-N*H* Lys); 9.483 (1H, s, N*H* ΔPhe).

^{13}C NMR (100.6 MHz, DMSO-*d*$_6$) δ (ppm): 22.60 (CH_2, γ-*C*H_2 Lys); 29.17 (CH_2, δ-*C*H_2 Lys); 31.38 (CH_2, β-*C*H_2 Lys); 40.23 (CH_2, ε-*C*H_2 Lys); 42.15 (CH_2, *C*H_2 Nap); 52.68 (CH, α-*C*H Lys); 65.15 (CH_2, *C*H_2 Cbz); 125.48 (CH, *C*H Nap); 126.04 (CH, *C*H Nap); 126.76 (C, α-*C* ΔPhe); 127.32 (CH, *C*H Nap); 127.39 (CH, *C*H Nap); 127.48 (CH, *C*H Nap); 127.54 (CH, *C*H Nap); 127.69 (CH, *C*H Cbz); 127.75 (CH, *C*H Cbz); 128.37 (CH, *C*H Cbz); 128.67 (CH, *C*H Nap); 129.07 (CH, *C*H ΔPhe); 129.20 (CH, *C*H ΔPhe); 129.96 (CH, *C*H ΔPhe); 131.65 (CH, β-*C*H ΔPhe); 131.78 (C, *C* Nap); 133.00 (C, *C* Nap); 133.65 (C, *C* ΔPhe); 134.17 (C, *C* Nap); 137.29 (C, *C* Cbz); 156.11 (C, *C*=O Cbz); 166.25 (C, *C*=O ΔPhe); 170.21 (C, *C*=O Lys); 171.54 (C, *C*=O Nap).

HR-MS (ESI) *m/z*: $[M + H]^+$ calcd for $C_{35}H_{36}N_3O_6$: 594.26; found: 594.2621.

2.1.2 Nanoparticles

2.1.2.1 Manganese ferrite nanoparticles

2.1.2.1.1 By regular co-precipitation

This synthesis was based on a co-precipitation method previously reported (213). Manganese sulphate monohydrate ($MnSO_4.H_2O$) and iron sulphate heptahydrate ($FeSO_4.7H_2O$) were used as starting reagents and different concentrations (several manganese/iron ratios: 0.4, 0.5, 0.6 in a total final salt concentration of 0.1 mM) were tested. The metal sulphates were simultaneously dissolved in a minimum amount of water (1 mL) to obtain a clear solution. The mixture was then added dropwise to 19 mL of an aqueous solution of trisodium citrate dihydrate in different final concentrations (0 and 0.05 mM) and NaOH (0.2 mM), under magnetic stirring at 90 °C. The reaction was completed in 2 h. Purification of manganese ferrite nanoparticles was carried out by successive cycles of centrifugation and dispersion in a mixture of water/ethanol (v/v 1:1), followed by drying at 100 °C.

2.1.2.1.2 By reverse co-precipitation

$MnSO_4.H_2O$ (111.55 mg, 0.66 mmol) and $FeSO_4.7H_2O$ (369.75 mg, 1.33 mmol) were used as starting reagents. The metal sulphates were simultaneously dissolved in a minimum amount of water (1 mL), to obtain a clear solution. The mixture was then added to 19 mL of an aqueous solution of trisodium citrate dihydrate (294.1 mg, 1 mmol), under magnetic stirring at 90 °C. After homogenization, an aqueous solution of NaOH (18.94 M, 211.19 μL) was added dropwise and the reaction was completed in 2 h.

Purification of manganese ferrite nanoparticles was carried out by successive cycles of centrifugation and dispersion in a mixture of water/ethanol (v/v 1:1), followed by drying at 100 °C.

The summary of the different reaction conditions is shown in **table 3.4**, Chapter 3.

2.1.2.2 APTES-coated manganese ferrite nanoparticles

Previously synthesised manganese ferrite nanoparticles (manganese/iron ratio=0.4, described in section 2.1.2.1.1) were selected to be further functionalized; for this purpose, 150 mL of ethanol, 3 mL of water, an ammonium hydroxide solution (5 M, 5.1 mL) and 944 μL of APTES were added to a flask and heated to 40°C, under magnetic stirring. After 20 minutes, a solution of the above nanoparticles (4 mg/mL, 6 mL) was added, and the reaction continued for 5 h. The nanoparticles were subjected to three cycles of magnetic decantation followed by redispersion in water (217).

2.1.2.3 Gold nanoparticles

Gold (III) chloride ($HAuCl_4$) (1 mM, 25 mL) was heated to 100°C. When the solution began to reflux, a trisodium citrate dihydrate solution (125 mM, 1 mL) was added and the mixture was allowed to reflux, under magnetic stirring. After 15 minutes, the heating was removed. This procedure was recently described by Nakagawa and Takagai (218).

2.1.2.4 Gold-decorated manganese ferrite nanoparticles

An aqueous solution of APTES-$MnFe_2O_4$ NPs (4 mg/mL, 0.7 mL) was sonicated until well dispersed. Under vortex vigorous agitation, the same solution was added dropwise to 5 mL of the previously prepared gold NPs.

2.1.2.5 Manganese ferrite/gold core/shell nanoparticles

An aqueous solution of gold-decorated APTES-$MnFe_2O_4$ (2 mg/mL, 1 mL) was diluted with water to a total of 40 mL. Here, 400 μL of a 1% trisodium citrate dihydrate solution and 200 μL of a 1% of $HAuCl_4$ solution were introduced. Finally, a hydroxylamine solution (80 mM, 200 μl) was added dropwise under vigorous magnetic stirring. After 15 minutes, the resulting nanoparticles were purified with three cycles of magnetic decantation followed by redispersion in water. This procedure consists of a modification of Natan's methodology, reported by Zhai (219,220).

2.1.2.6 Liposome nanoparticles

Liposome nanoparticles were prepared according to the ethanol injection method (221). A 20 mM DPPC ethanolic solution was injected, dropwise and under vigorous vortexing, in the volume of water required for a final lipid concentration of 1 mM, kept above DPPC melting transition temperature (41 °C).

2.1.2.7 Aqueous plasmonic magnetoliposomes

Similarly, aqueous magnetoliposomes were prepared (222). For such, a 20 mM solution of DPPC in ethanol was injected, dropwise at 70 °C, in an aqueous solution of core/shell $MnFe_2O_4$/Au NPs for a final concentration of 1 mM in lipids and 0.1 wt% in core/shell nanoparticles.

2.2 PREPARATION OF pH BUFFER SOLUTIONS

Buffer solutions in the pH range 2 – 10 were prepared from a 0.1 M sodium phosphate solution and a mixed solution of citric acid 0.05 M and boric acid 0.2 M in ultrapure water (Milli-Q grade), for a final volume of 50 mL. Table 1 shows the volumes required for such (223). The pH was measured with Metrohm 691 pH Meter, and the required adjustments were made using a solution of HCl 1 M or NaOH 1 M.

Table 2.1 – Calculated volumes for the preparation of different pH buffer solutions (224).

pH	Sodium phosphate (mL)	Citric/boric acid (mL)
2	1.250	48.750
3	6.000	44.000
4	11.250	38.375
5	16.500	33.500
6	20.500	29.500
7	25.250	24.750
8	28.750	21.250
9	32.750	17.250
10	36.500	13.500

2.3 HYDROGELATORS' CHARACTERIZATION

2.3.1 Critical gelation concentration

Critical gelation concentration (CGC) values were determined using the tube inversion test. For such, hydrogelator solutions were prepared in the concentration range 0.05 – 0.4 wt% (1 mL) by increasing the pH using a NaOH solution (1 M, 20 μL). Gelation was triggered by the addition of different amounts of glucono-δ-lactone (GdL) (3, 4 and 5 mg) to promote a slow pH drop (225).

2.3.2 Spectroscopic measurements

All fluorescence measurements were made using a HORIBA Jobin Yvon Fluorolog 3 spectrofluorimeter, with excitation and emission double monochromators, Glan-Thompson polarizers, and thermo-controlled cuvette holder. The emission spectra have been corrected for the system's instrumental response. For the self-assembly pH dependence studies, the hydrogelators were excited at 280 nm (naphthalene) and the emission spectra were collected between 290 and 600 nm, with 6.0 nm slits in both excitation and emission. In determining the critical aggregation concentration, Nile Red was used as a fluorescent probe, whereby the system was excited at 520 nm and the fluorescence intensity from 530 to 750 nm was collected, using 6.0 nm slits.

2.3.2.1 Self-assembly dependence on pH

A solution of the hydrogelator in ethanol (0.033 wt%) was used as stock for the preparation of the corresponding aqueous solutions (2 μM, 2 mL) in the pH range 2 – 10. To evaluate the effect of pH on the hydrogelator behaviour, the emission spectra were obtained for each hydrogelator solution.

2.3.2.2 Critical aggregation concentration

A fixed volume of an ethanolic solution of Nile Red (0.25 mM, 8 μL) was placed in several vials and the solvent was evaporated. To these vials, hydrogelator solutions at concentrations ranging from 0.00001 to 0.01 wt%, for a final volume of 2 mL, were added. After sonication, the mixture was allowed to stand for 2 h prior to spectroscopic measurements. Fluorescence emission spectra were obtained for each solution. This procedure was adapted from (226).

2.4 NANOPARTICLES' CHARACTERIZATION

2.4.1 Structural characterization

2.4.1.1 Dynamic Light Scattering

Hydrodynamic diameter, polydispersity index (PDI) and zeta potential measurements were carried out with an Anton Paar Litesizer 500 equipment, for a maximum of 1000 runs at 25 °C, using back scattering and a semiconductor laser diode with a 658 nm wavelength. The aqueous suspension containing the nanoparticles was filtered using a 0.22 μm filter-equipped syringe.

2.4.1.2 Transmission electron microscopy

High resolution-transmission electron microscopy (TEM) images were recorded with a JEOL JEM 2010F transmission electron microscope (at C.A.C.T.I. – Centro de Apoio Cientifico e Tecnolóxico á Investigación, Vigo, Spain), operating at 200 kV, and coupled to an electron dispersive spectroscopic analyser (EDS). The nanoparticles were dispersed in water and a drop of that solution was placed on the TEM 400 mesh copper grid with Formvar/Carbon (Ref. S162-4 from Agar Scientific), held by tweezers and allowed to dry. The images were treated with the *ImageJ* software, which consisted of adjusting contrast and selecting the particles.

2.4.1.3 X-ray diffraction

The X-ray diffraction (XRD) analysis was performed using the Malvern PAN'alytical X'Pert PRO diffractometer (at UME-UTAD), in the Bragg-Brentano configuration, operating with Cu K_α radiation. The results were analysed with *FullProf* software, on the basis of Rietveld refinement.

2.4.2 SQUID measurements

Magnetic properties were investigated with an MPMS3 Superconducting Quantum Interference Device (SQUID) (Quantum Design) magnetometer. Hysteresis cycles were determined using the appropriate range of magnetic fields for each sample. The trapped flux in the superconducting coil was corrected for an accuracy of residual less than 2 Oe.

2.4.3 Magnetic Hyperthermia

The heating capacity of magnetic nanoparticles was investigated through the preparation of an aqueous solution of $MnFe_2O_4$ NPs at 1 mg/mL, using the nanoTherics magneTherm equipment, at C.A.C.T.I. – Centro de Apoio Cientifico e Tecnolóxico á Investigación, Vigo, Spain.

2.4.4 UV-Vis-NIR absorption spectroscopy

The absorption spectra of nanoparticles' solutions were recorded with the Shimadzu UV-3600 Plus UV-VIS-NIR spectrophotometer, with 2.0 nm slits.

2.5 HYDROGEL AND MAGNETOLIPOGEL CHARACTERIZATION

2.5.1 Incorporation of nanoparticles into hydrogel matrix

First, hydrogelator solutions (0.3 wt%) were prepared at pH 9 – 10 to a final volume of 200 μL. For magnetolipogels, plasmonic magnetoliposomes (1 mM in lipids, 0.1 wt% in $MnFe_2O_4$/Au NPs, 100 μL) were introduced to a final concentration of 0.5 mM in lipids and 0.05 wt% in $MnFe_2O_4$/Au nanoparticles; for magnetogels, $MnFe_2O_4$/Au nanoparticles (26.4 mg/mL, 3.8 μL) were added for a final concentration of 0.05 wt%; for lipogels, a liposome solution (1 mM, 100 μL) was added for a final DPPC concentration of 0.5 mM. Hydrogelation was achieved with the addition of GdL (0.5 wt%).

2.5.2 Scanning transmission electron microscopy

Gels' scanning transmission electron microscopy (STEM) recordings were made with the NanoSEM—FEI Nova 200, with an integrated system of X-ray microanalysis (EDS) and backscattered electron diffraction patterns analysis (EBSD – Electron Backscatter Diffraction) EDAX – Pegasus X4M, operating at 15 kV. A portion of each gel sample was placed on a TEM 400 copper mesh grid with Formvar/Carbon (Ref. S162-4 from Agar Scientific), held by tweezers, and allowed to dry. Images were processed with *ImageJ* software to adjust contrast and select fibres/nanoparticles.

2.5.3 Rheology

The viscoelastic properties of the gels were determined using a stress-controlled rotational rheometer Anton Paar MCR300. Gel-forming solutions were placed in a Couette cell with 1 mL volume and 0.5 mm gap, and both elastic (G') and viscous (G'') moduli measurements were performed at 25 °C. Gelation kinetics was monitored during 10 h by applying a low amplitude oscillatory shear (1×10^{-3}% for hydrogels; 1×10^{-4}% for the magnetolipogel) at 1 Hz. Mechanical spectra were obtained with a constant strain amplitude (1×10^{-3}% and 1×10^{-2}% for hydrogels; 1×10^{-4}% and 1×10^{-3}% for the magnetolipogel), sweeping the frequency from 0.024 to 100 Hz. To evaluate the influence of temperature on the viscoelastic properties of compound **1**-based hydrogel, a heating-cooling cycle between 25 and 80 °C (at a rate of 2 – 3 °C/min) was performed. Finally, the linear viscoelasticity (SAOS) and the large amplitude oscillatory

shear (LAOS) regimes were determined sweeping the strain amplitude in the range 1×10^{-4} – 200% at 1 Hz.

2.5.4 Photophysical studies

With the exception of self-assembly kinetics studies, all fluorescence measurements were made using a HORIBA Jobin Yvon Fluorolog 3 spectrofluorimeter, with double excitation and emission monochromators, Glan-Thompson polarizers, and thermo-controlled cuvette holder. The emission spectra have been corrected for the system's instrumental response.

2.5.4.1 Local environment of composite gel fibres

2.5.4.1.1 Hydrogelator emission spectra

The effect of the different nanoparticles on the hydrogel fibres was evaluated by collecting the emission spectra of the hydrogel, magnetolipogel, magnetogel and lipogel. For this purpose, the composite gel solutions were transferred to a microcuvette, and after gelation, fluorescence intensity was scanned in the range 290 – 600 nm, using an excitation wavelength of 280 nm (naphthalene).

2.5.4.1.2 Fluorescence anisotropy

The local viscosity of fibres in the different composite hydrogels was studied by fluorescence anisotropy. Thus, composites were prepared according to the conditions described in section 2.5.1 and Nile Red was added to a final concentration of 2.5 μM. After gelation, an excitation wavelength of 520 nm was used to collect fluorescence intensity from 530 to 750 nm. Steady-state fluorescence anisotropy values, r, were determined by the following equation,

$$r = \frac{I_{VV} - GI_{VH}}{I_{VV} + 2GI_{VH}} \qquad (2.1)$$

where I_{VV} and I_{VH} are the fluorescence intensities of the emission spectra obtained with vertical and horizontal polarization for vertically polarized excitation light, I_{HV} and I_{HH} are the fluorescence intensities obtained with vertical and horizontal polarization for horizontally polarized excitation light, respectively, and $G = I_{HV}/I_{HH}$ is the experimental correction factor.

2.5.4.1.3 Self-assembly kinetics

To understand the impact of each component on the self-assembly process of the gel, the four different systems were prepared as described above. Each composite gel solution was transferred to a fluorescence cuvette and gelation was followed by exciting the fluorophore at 520 nm and collecting the

fluorescence intensity at a fixed wavelength (620 nm) during 6 h. Steady-state spectra were obtained in a SPEX Fluorolog 2 spectrofluorimeter with 4.0 nm slits on both the excitation and emission monochromators.

2.5.4.2 Raman spectroscopy

To study the effect of the different nanoparticles in the intramolecular bonding pattern/secondary structure of the hydrogel fibres, Raman spectroscopy was performed on the samples described in section 2.5.1, using a HORIBA LabRAM HR Evolution Raman Spectrometer, equipped with liquid nitrogen cooled charge couple device (CCD) detector, with a resolution above 1 cm^{-1}. The excitation line, 532 nm of a solid-state laser, was focused on the sample using a ×100 objective of an Olympus Microscope BXFM-ILHS in a backscattering geometry and with the configuration of 600 grooves/mm gratings. The spectra were collected with a measured power of 5% × 7 mW, an acquisition time of 45 seconds averaged over 10 scans, in the range of 770 – 1800 cm^{-1}.

2.5.4.3 Drug release studies

2.5.4.3.1 Incorporation of drugs into hydrogel and magnetolipogel matrices

Hydrogels were prepared according to the procedure described in section 2.5.1, by adding 5(6)-carboxyfluorescein (CF) to the hydrogel solution for a final concentration of 10 μM.

Regarding magnetolipogels, three different magnetoliposome solutions were formulated. The first one was prepared as described in section 2.1.2.7, in which CF was added to the $MnFe_2O_4$/Au NPs solution for a final concentration of 20 μM; the second formulation was produced under the same conditions, after which three centrifugation cycles (4000 rpm, 30 min) were carried out in order to remove the carboxyfluorescein external to the magnetoliposomes (the volume of solvent was then replaced); for the third solution, $MnFe_2O_4$/Au NPs and CF were used for a final concentration of 0.3 wt% and 20 μM, respectively. Then, 100 μL of the required magnetoliposome solution was introduced into the hydrogel one, to a final concentration of 0.5 mM in DPPC.

A summary of the composition of the different drug-loading gels is given in **table 3.13**, Chapter 3.

2.5.4.3.2 Fluorescence anisotropy

To ascertain the microstructure in which CF is located in both the hydrogel and magnetolipogels, precursor gel solutions described above were transferred to a microcuvette. After gelation, fluorescence intensity was measured by exciting the fluorophore at 495 nm and collecting the emission spectra in the

range 505 – 650 nm with vertical and horizontal polarization for vertically polarized excitation light and with vertical and horizontal polarization for horizontally polarized excitation light.

2.5.4.3.3 Drug release assays

Cargo release from hydrogels and magnetolipogels loaded with CF was assessed. The prepared gels were allowed to stabilize overnight at room temperature, after which phosphate buffer pH=7.4 (0.01 M, 800 μL) was carefully added to their surface. Aliquots of the layered liquid (200 μL) were taken at 0.5, 1, 1.5, 2, 3, 4, 5, 6, 26, 32, 48 and 54 h from the time the buffer solution was placed on top of the gels; after removing each aliquot, the volume of buffer solution equal to that removed was immediately replaced. The concentration of CF in each aliquot was determined by collecting the fluorescence intensity at 517 nm, at an excitation wavelength of 495 nm (5(6)-carboxyfluorescein). The result was converted to percentage of release using a standard calibration curve. Each assay was performed in triplicate and the mean percentage CF release was plotted against time.

For the active CF release tests, the same procedure was adopted, in which two cycles of stimulation were included for the magnetolipogels at 26 and 48 h. Accordingly, an AMF (100 Hz, 2.09 mT – solenoid with 584 turns per metre, 5.75 cm in radius and 28.4 cm long), a laser (808 nm, 500 mW, 1.67 W/cm^2) and a lamp (600 nm cut-on, 0.1 mW) or a second laser (808 nm, 800 mW, 5.00 W/cm^2) were applied separately, during 30 min, to three equivalent sets of gels.

2.5.4.4 Complementary studies

To understand the changes in the matrix of the magnetolipogels upon stimulation, hydrogels and magnetolipogels were prepared as detailed in section 2.5.1. Phosphate buffer pH=7.4 (0.01 M, 800 μL) was placed on the surface of the gels; 200 μL aliquots were removed, and the equivalent volume of buffer solution was replaced at time intervals equivalent to those in the CF release assays. At 26 and 48 h, the magnetolipogels were submitted to 30 minutes of laser irradiation (808 nm, 500 mW, 1.67 W/cm^2). The fibre release profile was followed by collecting the fluorescence intensity at 337 nm, using an excitation wavelength of 280 nm (naphthalene). Again, each experiment was performed in triplicate.

Chapter 3

RESULTS AND DISCUSSION

3.1 DEHYDRODIPEPTIDE-BASED HYDROGELS

3.1.1 Dehydrodipeptide synthesis

The rational design of the hydrogelator candidates considered the preponderance of π-π stacking and hydrophobic interactions in gelation and properties of low molecular weight peptides, as well as the additional advantages provided by dehydroamino acids, such as backbone conformational constraints and resistance to proteolysis.

In this regard, we took advantage of the methodologies developed within our research group for the synthesis of *N*-capped dehydrodipeptides in order to adjust hydrophobicity/hydrophilicity balance and thus favour their gelation at low concentrations. Accordingly, two dehydrodipeptides with a L-(*N*-ε-benzyloxycarbonyl)lysine residue and a (*C*-terminus) dehydroamino acid – dehydroaminobutyric acid ΔAbu, interesting for antimicrobial nanomaterials (227), and dehydrophenylalanine ΔPhe, known for stabilizing β-turns of short peptides (228) – were *N*-protected with 2-naphthaleneacetic acid, resulting in the amphipathic molecules schematized in **figure 3.1**.

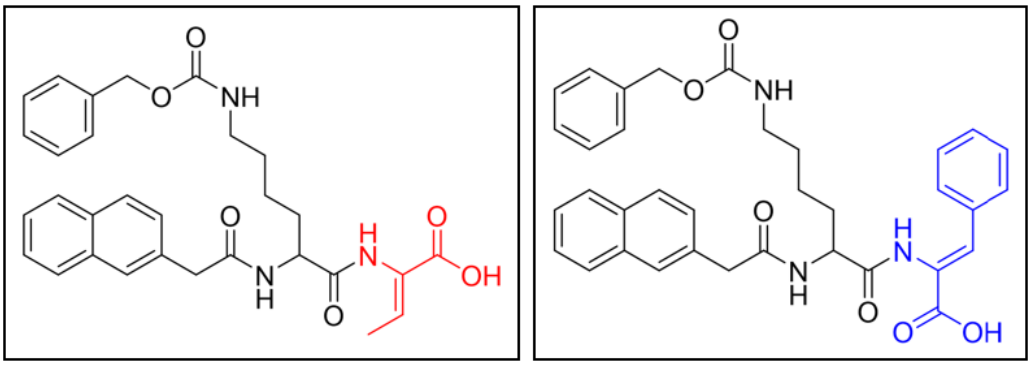

Figure 3.1 – Structure of the designed hydrogelator candidates: Nap-L-Lys(Cbz)-*Z*-ΔAbu-OH (**1**) and Nap-L-Lys(Cbz)-*Z*-ΔPhe-OH (**2**).

In these structures, it is possible to identify a central aromatic moiety, consisting of the protected lysine residue, and a more hydrophilic terminus owing to the carboxylic acid function.

Concerning the synthesis of the dehydrodipeptide Nap-L-Lys(Cbz)-*Z*-ΔAbu-OH (**1**) (**scheme 3.1**), the coupling of *N*-*tert*-butyloxycarbonyl-L-lysine(*N*-benzyloxycarbonyl)-OH (Boc-L-Lys(Cbz)-OH, **4**) with the methyl ester of threonine (H-L-Thr-OMe, **3**) afforded compound **5** in moderate-high yield. A standard HBTU methodology was used, which involves the deprotonation of the carboxylic acid, followed by attack on the carbonyl carbon of HBTU, forming an *O*-acyl urea derivative and the anion of

1-hydroxybenzotriazole. The latter reacted with each other to give rise to tetramethylurea and the activated ester. Finally, the ester reacts with the amine, forming the amide and 1-hydroxybenzotriazole (229).

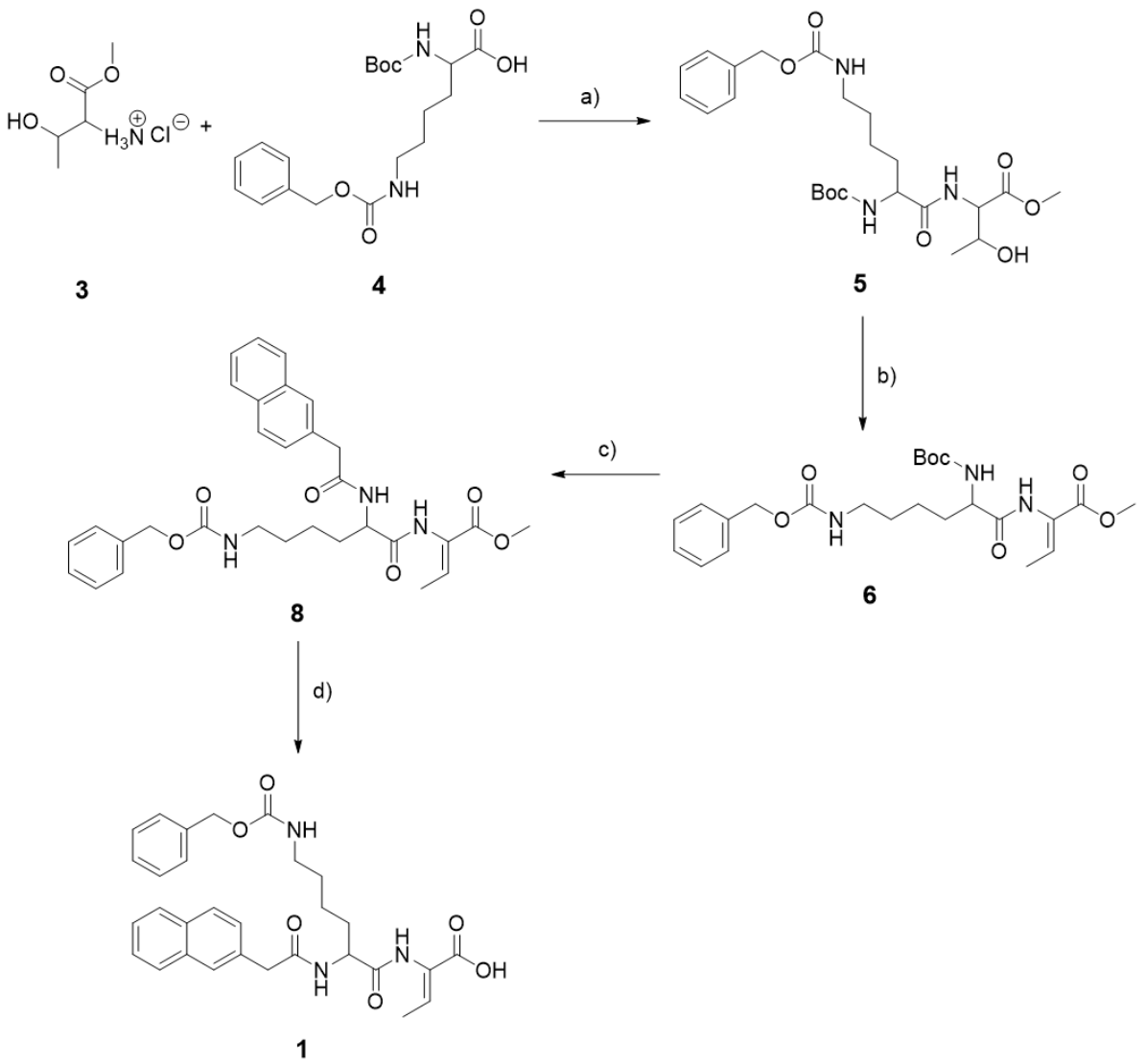

Scheme 3.1 – Synthetic route for compound **1**. a) HBTU, Et_3N, MeCN; b) (i) Boc_2O, DMAP, dry MeCN, (ii) TMG; c) (i) TFA, (ii) 2-*n*aphthaleneacetic acid, HBTU, Et_3N, MeCN; d) (i) NaOH (1 M), 1,4-dioxane, (ii) $KHSO_4$ (1 M).

Compound **6** was obtained by dehydration of compound **5** using a two-step protocol developed by our research group (**scheme 3.2**). This involves the formation of a carbonate as intermediate after the addition of Boc_2O in the presence of DMAP. Elimination occurs by the addition of TMG (230). At this stage, the disappearance of the ^{1}H NMR signals assigned to the *β*-hydroxy group (δ 4.988 ppm) and α-CH proton of threonine and to the shift of the β-C*H*-corresponding signal of threonine (δ 4.259 – 4.289 ppm) were followed. This reaction leads to the thermodynamically more stable *Z*-isomer. The Boc protecting group of compound **6** was removed with TFA, exposing lysine α-amine, and

thus making it available for coupling. Its protection with 2-naphthaleneacetic acid was done again using the HBTU strategy.

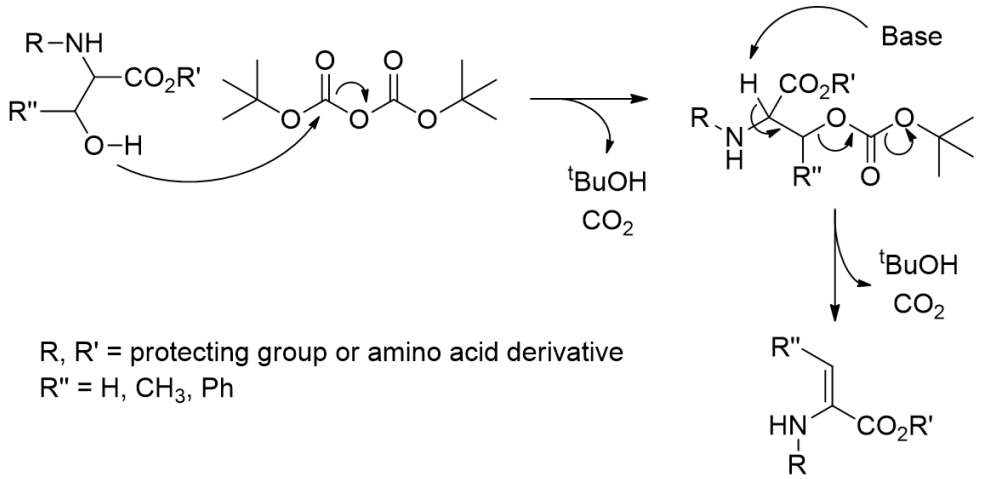

Scheme 3.2 – Mechanism of dehydration of β-hydroxyamino acid derivatives with Boc_2O/DMAP and TMG.

The synthesis ended with alkaline hydrolysis of the methyl ester in 1,4-dioxane using a 1 M NaOH solution, followed by pH adjustment to 2. Here, compound **1** was afforded as a white solid in 64.7% yield.

The ^{1}H NMR spectrum of Nap-L-Lys(Cbz)-*Z*-ΔAbu-OH (**1**) dehydrodipeptide in DMSO-d_6 (**figure 3.2**) shows all the expected signals. It is possible to observe that both the protons from the lysine side chain and from the γ-CH_3 of dehydroaminobutyric acid (duplet) emerge at low chemical shifts. The CH_2 of naphthalene appears as an AB-X system (double duplet) since the two strongly coupled non-equivalent protons are weakly coupled to a third non-equivalent nucleus (231). The α-CH of lysine appears as a multiplet and the signal at δ 4.990 ppm is assigned to the CH_2 of the benzyloxycarbonyl protecting group. Also noteworthy are the quartet (δ 6.501 – 6.554 ppm) and the singlet due to the protons from β-CH and the carboxylic acid of dehydroamino butyric acid, respectively.

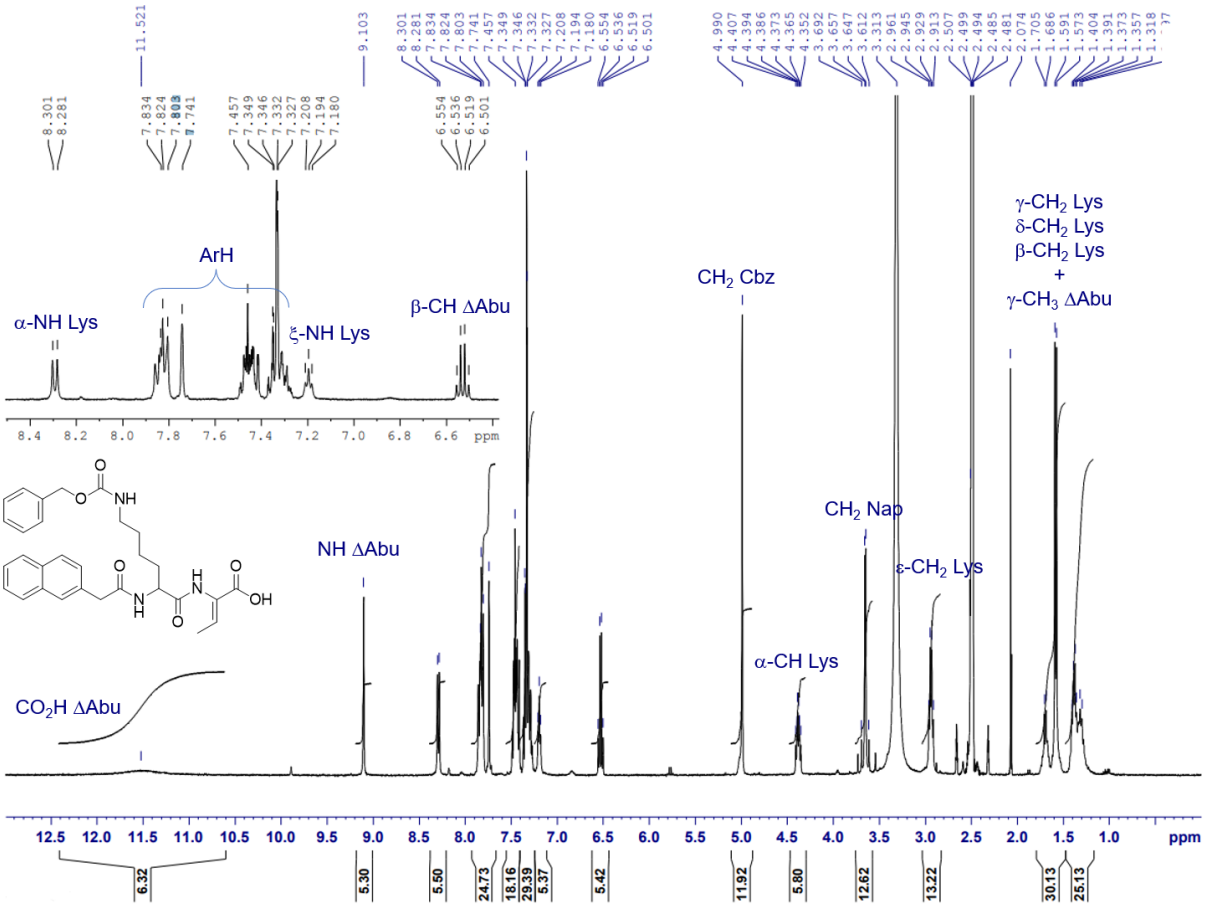

Figure 3.2 – ^{1}H NMR spectrum of Nap-L-Lys(Cbz)-*Z*-ΔAbu-OH (**1**), in DMSO-d_6.

Nap-L-Lys(Cbz)-*Z*-ΔPhe-OH (**2**) dehydrodipeptide was prepared following a synthetic strategy similar to that described for compound **1** (**scheme 3.3**). This time, coupling of compound **4** with the methyl ester of *β*-hydroxyphenylalanine (H-D,L-Phe(*β*-OH)-OMe, **9**) was performed, using the HBTU methodology to give a diastereomeric mixture of the corresponding *β*-hydroxydipeptide. The stereospecific dehydration reaction with Boc2O/DMAP and TMG gave compound **11**. Next, the *N*-protecting group removal was carried with TFA, followed by coupling with 2-naphthaleneacetic acid in the presence of HBTU. Finally, saponification of compound **13** and pH adjustment afforded compound **2** as a white solid (86.2% yield).

The ^{1}H NMR spectrum of hydrogelator **2** (**figure 3.3**) shows the CH_2 of naphthalene as a double duplet and the α-CH of the lysine residue as a multiplet at δ 4.360 – 4.414 ppm. Next, one can see the well-defined singlet from CH_2 of benzyloxycarbonyl capping group, followed by a region that includes both the aromatic nuclei and the β-CH of dehydrophenylalanine. Lastly, a duplet and a singlet were recorded at 8.354 – 8.373 and 9.483 ppm, assigned to the α-NH of lysine and dehydrophenylalanine, respectively.

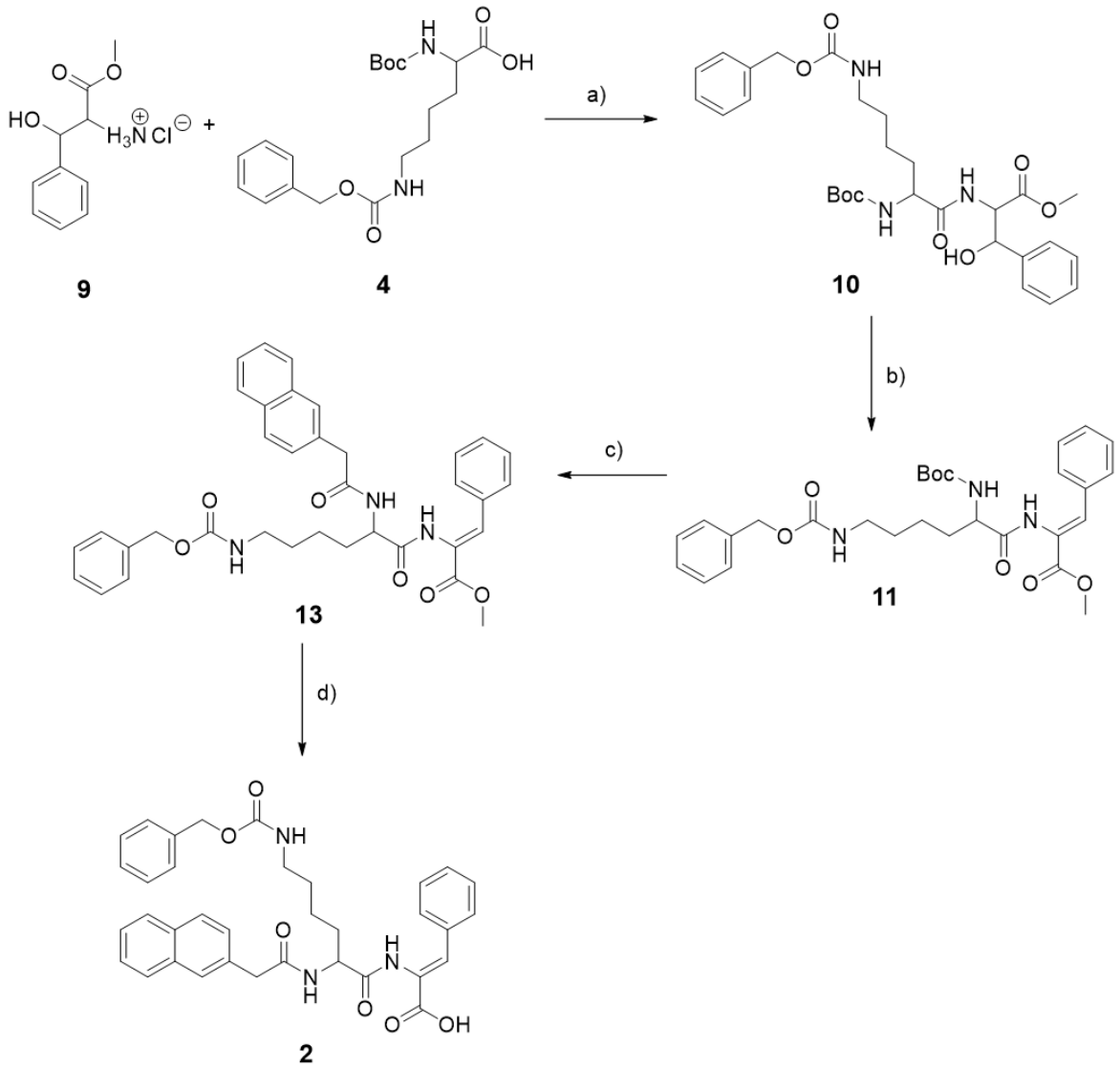

Scheme 3.3 – Synthetic route for compound **2**. a) HBTU, Et_3N, MeCN; b) (i) Boc_2O, DMAP, dry MeCN, (ii) TMG; c) (i) TFA, (ii) 2-naphthaleneacetic acid, HBTU, Et_3N, MeCN; d) (i) NaOH (1 M), 1,4-dioxane, (ii) $KHSO_4$ (1 M).

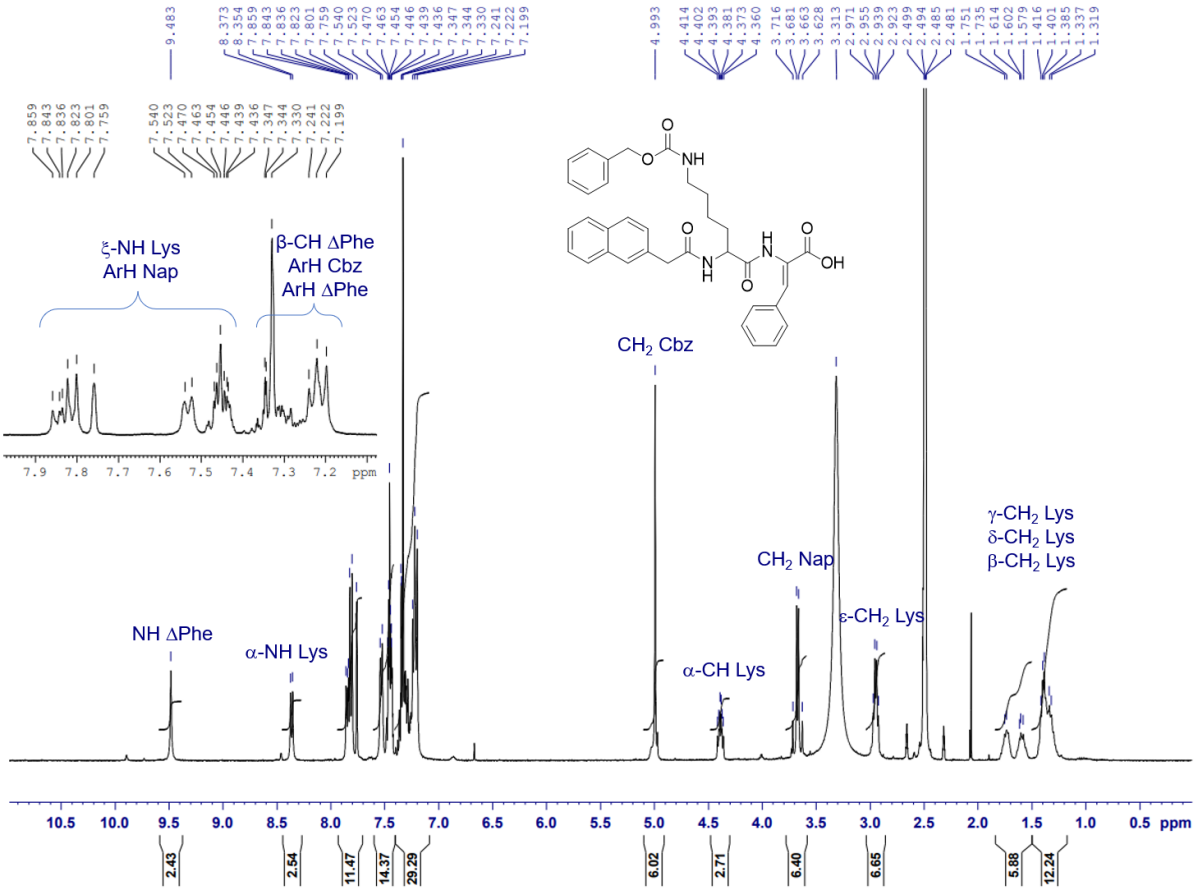

Figure 3.3 – ^{1}H NMR spectrum of Nap-L-Lys(Cbz)-Z-ΔPhe-OH (**2**), in DMSO-d$_6$.

3.1.2 Evaluation of dehydrodipeptides as potential hydrogelators

3.1.2.1 Gelation and critical gelation concentration

The gelling capability of compounds **1** and **2** was tested. Several gelation-inducing stimuli for *N*-capped peptides are reported in literature, among which are solvent exchange, temperature, and pH (232). Given the extremely low solubility of compound **2** at neutral pH, the gelation approach involved dissolving both hydrogelators independently in the concentration range 0.07 – 0.4 wt% at pH 10 with a solution of NaOH (1 M, 2 % (v/v)). Then, a gradual decrease of pH was promoted using GdL (in the concentration range 0.3 – 0.5 wt%). Gelation was evaluated using the tube inversion test and **figures 3.4** and **3.5** show the results obtained for the different assayed conditions.

Regarding Nap-L-Lys(Cbz)-*Z*-ΔAbu-OH, gelation was achieved in a concentration range of 0.08 – 0.4 wt% (**figure 3.4**). This low CGC is useful considering that it allows obtaining a gel with small amounts of compound, which makes it economically feasible and more biocompatible in case the hydrogelator shows some cytotoxicity (233). On the other hand, we anticipated by the tube inversion test that the hydrogelator concentration has a direct impact on hydrogel viscoelastic properties, as will be confirmed by downstream

rheological studies. Furthermore, the higher the concentration of GdL, the lower the pH of the hydrogel, which limits its biomedical application (234,235).

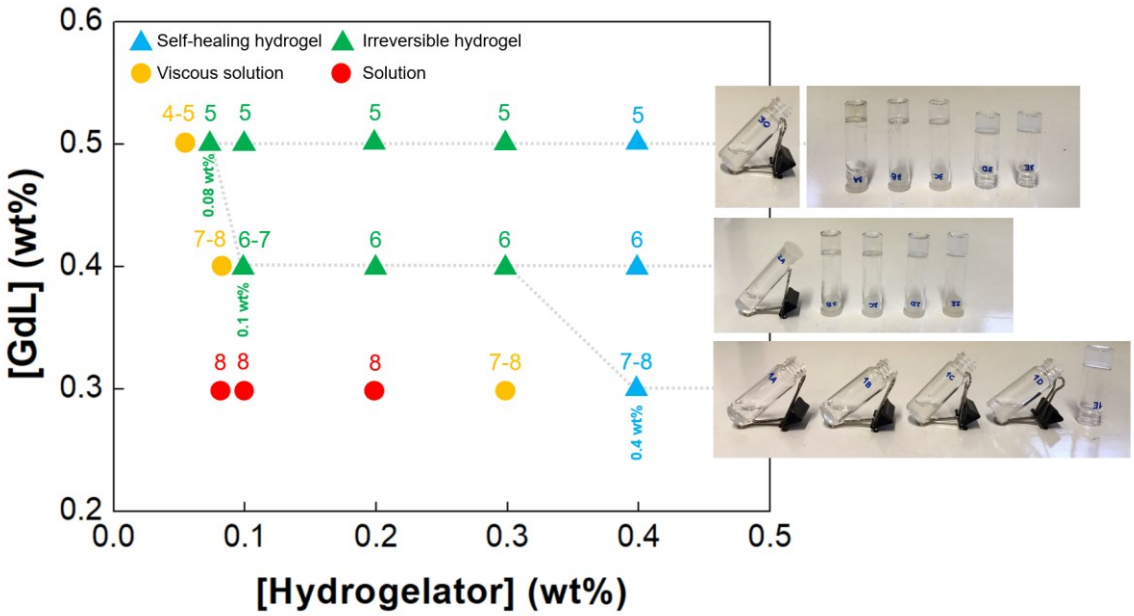

Figure 3.4 – Phase transition diagram of hydrogelator **1** (Nap-L-Lys(Cbz)-*Z*-ΔAbu-OH) through addition of GdL to a basic hydrogelator solution (NaOH 1 M, 2% (v/v)). The dimensionless numbers indicate the measured pH of the hydrogel.

Interestingly, Nap-L-Lys(Cbz)-*Z*-ΔPhe-OH dehydrodipeptide formed milky-looking hydrogels in the same concentration range: 0.08 – 0.4 wt% (**figure 3.5**). Unlike peptide **1**, the low CGC resulted from the addition of an intermediate amount of GdL (0.4 wt%), indicating that pH individually impacts de gelling ability of the synthesised compounds. This topic will be further discussed in section 3.1.2.2.

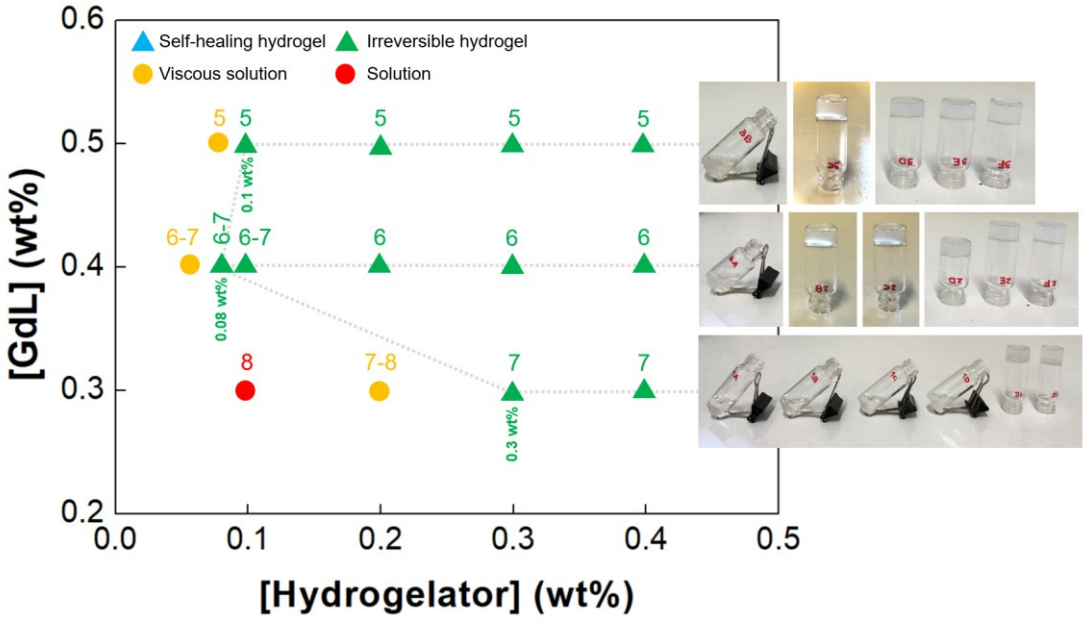

Figure 3.5 – Phase transition diagram of hydrogelator **2** (Nap-L-Lys(Cbz)-*Z*-ΔPhe-OH) through addition of GdL to a basic hydrogelator solution (NaOH 1 M, 2% (v/v)). The dimensionless numbers indicate the measured pH of the hydrogel.

In the context of our research group, the synthesised hydrogelators have a significantly lower CGC compared to the established library of hydrogel-forming dehydrodipeptides *N*-capped with naproxen (including Npx-L-Phe-*Z*-ΔPhe-OH and Npx-L-Phe-*Z*-ΔAbu-OH) (236). Given the possibility of functionalizing lysine with Cbz protecting group, we were able to play with π-π stacking and hydrophobic interactions, which underlie peptide self-assembly (237).

The addition of 3 mg of GdL per millilitre of hydrogelator solution results in a final pH of 7 – 8. Here, there is a slight difference in the relative CGC values of peptides **1** and **2**, assigned to the dehydroamino acid moiety. In fact, at this pH, both peptides are deprotonated at the terminal carboxylic acid, which gives an advantage to dehydropeptide **2** in establishing anion-π interactions beyond aromatic stacking, given the presence of an additional aromatic ring. This kind of attractive non-covalent interactions have become vital in supramolecular chemistry, and several reports have already described their ability to direct and stabilize the molecular self-assembly process (238–240).

The same phenomenon occurs (although at a smaller scale) when we use a concentration of 0.4 wt% in GdL (final pH 6 – 7), which is visible by the 0.2 mg difference in the CGC values (compound **1**: 0.1 wt%; compound **2**: 0.08 wt%).

Nevertheless, a twist in the gelation results is observed when 5 mg of GdL are added to 1 mL of the hydrogelator solutions. For a pH *ca.* 5, the dehydrodipeptide Nap-L-Lys(Cbz)-*Z*-ΔAbu-OH holds the lowest CGC (0.08 wt% versus 1.0 wt% of hydrogelator **2**). Here, the protonation of the monomers gains a significant expression, making them more hydrophobic: the degree of solubility comes to control their gelation ability. Indeed, Adams and co-workers argue that the hydrophobic/hydrophilic balance of the hydrogelator is the dominant element for the formation of self-supporting gels, and intermediate logP values (between 3.4 and 5.5) are desirable (241,242). So, we computed the predicted logP value and noticed that the one of compound **2** exceeds that range, indicating that the thermodynamic stability of the nanofibers may be compromised. Under these conditions, this effect is not as evident for dehydrodipeptide **1** (cLogP of 4.54), allowing it to gel at a lower concentration. The optimum gelling conditions for both compounds are summarized in **table 3.1**.

Table 3.1 – Optimized gelling conditions for the synthesised dehydrodipeptides. *Obtained from *ChemDraw* software.

Peptide	CGC (wt%)	CGC (mM)	GdL concentration (wt%)	pH	cLogP*
1	0.08	1.50	0.5	5	4.54
2	0.08	1.35	0.4	6-7	5.54

3.1.2.2 Self-assembly dependence on pH

To better understand the gelation profile of the synthesised hydrogelators, the fluorescence emission of the intrinsic probe naphthalene was followed in the pH range 2 – 10 (**figure 3.6**), exciting at 280 nm and thus avoiding direct electronic excitation of dehydrophenylalanine.

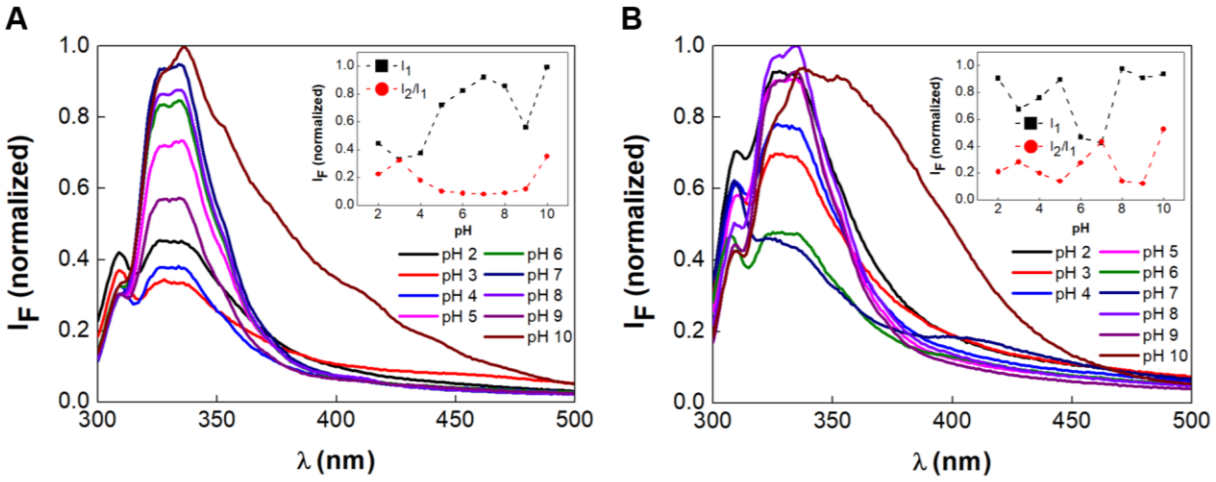

Figure 3.6 – Fluorescence emission spectra of Nap-L-Lys(Cbz)-*Z*-ΔAbu-OH (A) and Nap-L-Lys(Cbz)-*Z*-ΔPhe-OH (B) in the pH range 2 –10. Insets: variation of maximum fluorescence intensity (I_1 – black squares) and intensity ratio (I_2/I_1 – red circles) of naphthalene aggregate (I_2, 400 nm) and monomer band (I_1, 340 nm) within the studied pH range. λ_{exc}=280 nm.

Overall, a main band is observed at 340 nm and a subtle second band around 400 nm, attributed to the monomer and aggregate state, respectively. Although the maximum emission wavelength remains stable over the entire pH range and for both hydrogelators, there are considerable fluctuations in fluorescence intensity.

In regard to Nap-L-Lys(Cbz)-*Z*-ΔAbu-OH (**figure 3.6 A**), an increasing fluorescence emission (λ=340 nm) was recorded up to pH=7, explained by the successively higher concentration of deprotonated species, which favour the monomer state. For Nap-L-Lys(Cbz)-*Z*-ΔPhe-OH, the same occurs up to pH=5 (**figure 3.6 B**), after which a dramatic reduction in the maximum fluorescence intensity is found.

Concerning the aggregate-to-monomer band ratio, there is a relative maximum at pH=3 for both hydrogelators, close to the predicted pK_a of the terminal carboxylic acid: 3.87 for compound **1** and 3.66 for compound **2** (determined using *Marvin Sketch* software). Indeed, it is well-known that dipeptides are likely to aggregate when the carboxylic acid is protonated, which occurs to a 100% extension when the pH is below their pK_a.

A new maximum appears in the aggregate-to-monomer band ratio of compound **2** at pH=7, identified as its sol-gel transition pH (243). The extent of deprotonation of the terminal carboxylic acid is pH dependent

and dictates its solubility; thus, considering the greater hydrophobicity of that hydrogelator compared to Nap-L-Lys(Cbz)-*Z*-ΔAbu-OH (as supported by the cLogP values), it is reasonable the need of the latter for a wider pH drop to achieve gelation. This may explain the higher CGC of compound **1** under neutral conditions and that of compound **2** under acidic environments.

For both compounds, there is also an increase in the aggregate-to-monomer band ratio at pH=10, which may be related to the generation of additional organized molecular structures, such as micelles.

3.1.2.3 Critical aggregation concentration

The aggregation and self-assembly properties of the synthesised dehydrodipeptides were evaluated with a constant concentration of a fluorescent probe (Nile Red) for increasing amounts of compound, at pH=6. **Figure 3.7** shows fluorescence intensity of Nile Red plotted against dehydrodipeptide concentration. The former is higher when the probe is located in the hydrophobic core of aggregates, so we can assume that the formation of nanoassemblies capable of capitalizing hydrophobic molecules takes place after the inflection point; here, CAC is found (226).

Overall, one can note the residual fluorescence for very low concentration values, which markedly enhances with increasing amounts of compound. Regarding dehydrodipeptide **1** (Nap-L-Lys(Cbz)-*Z*-ΔAbu-OH), the inflection point appears at 115.7 μM (**figure 3.7 A**), while that of dehydrodipeptide **2** (Nap-L-Lys(Cbz)-*Z*-ΔPhe-OH) emerges at a concentration 16 times lower (7.1 μM) (**figure 3.7 B**). This considerable difference may be related to the solubility of the compounds. By observing their structure, one can notice the higher capacity of Nap-L-Lys(Cbz)-*Z*-ΔPhe-OH for hydrophobic interactions and aromatic stacking due to the extra aromatic ring in the dehydroamino acid moiety, which privileges intersolute interactions over interactions with water. Furthermore, the predicted LogP values (4.54 and 5.54 for Nap-L-Lys(Cbz)-*Z*-ΔAbu-OH and Nap-L-Lys(Cbz)-*Z*-ΔPhe-OH, respectively) support this conjecture as they demonstrate the higher affinity of compound **1** for water. Interestingly, the large difference in the CAC of compounds **1** and **2** does not translate into a difference of the same order of magnitude in the previously reported CGC values at pH=6; this can be explained by the occurrence of pre-fibrillar nanostructures for compound **2**, such as micelles, vesicles, and nanotubes. The latter also reveals a concentration beyond which Nile Red fluorescence intensity decays; here, the monomer state might be favoured again, given the energy cost involved in forming higher self-assembled structures (e.g., hydrogel) (244).

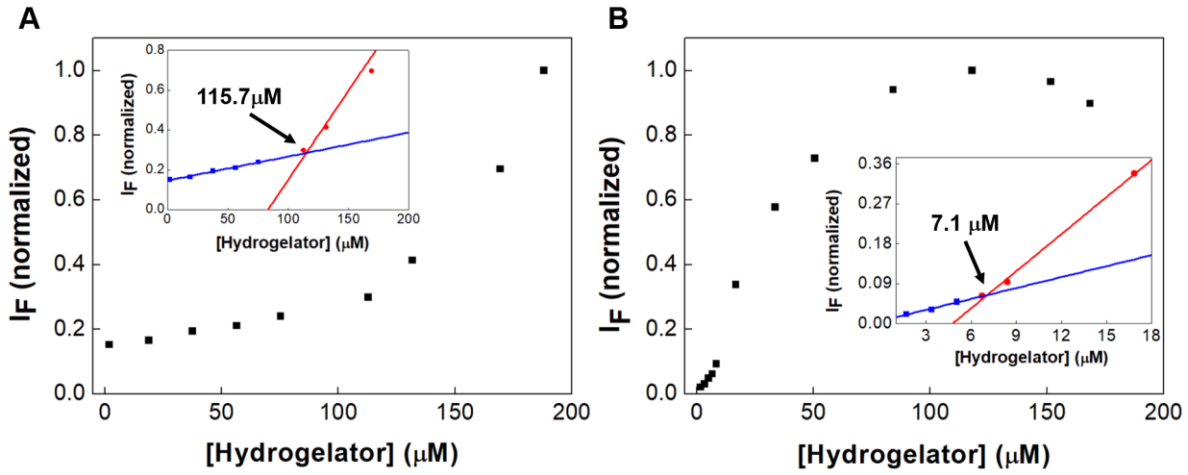

Figure 3.7 – CAC determination for Nap-L-Lys(Cbz)-*Z*ΔAbu-OH (A) and Nap-L-Lys(Cbz)-*Z*ΔPhe-OH (B) at pH=6, using Nile Red as fluorescent probe. λ_{exc}=520 nm, λ_{em}=620 nm.

3.1.3 Hydrogels' microstructure

To study hydrogels' microstructure by STEM, hydrogelator solutions were prepared to a concentration of 0.3 wt% and the final pH was adjusted with the addition of GdL to a final concentration of 0.4 wt%. For both gels, a network of long fibres ranging from 16 to 117 nm in thickness is visible, differing in density and extent of entanglement (**figure 3.8**).

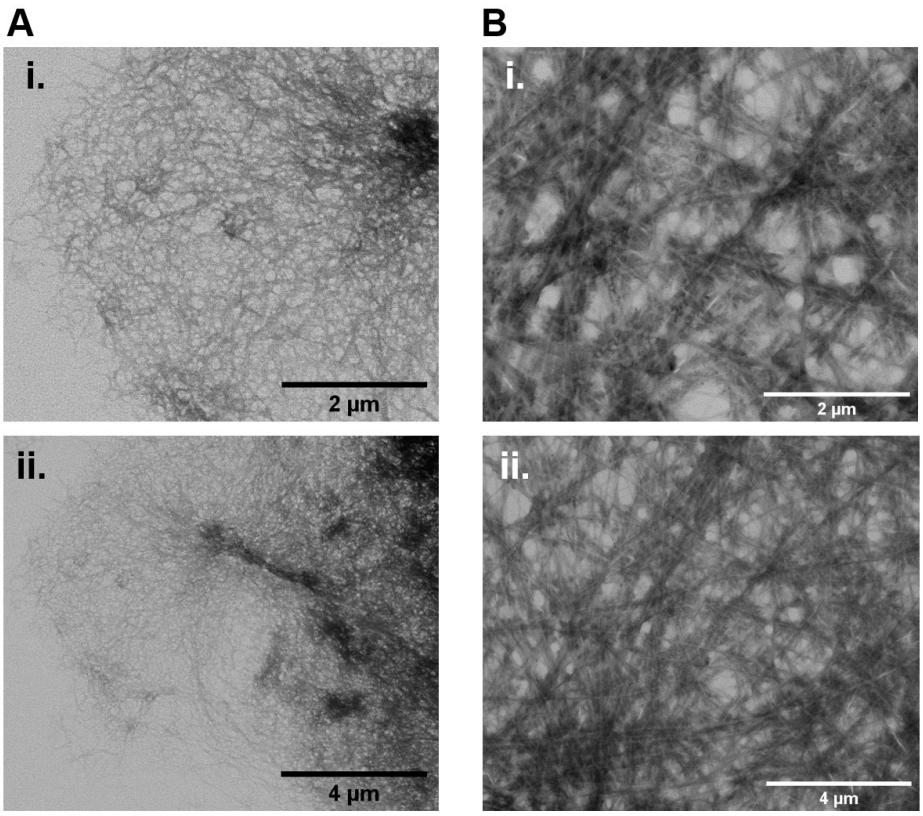

Figure 3.8 – STEM images of dehydrodipeptide **1**- (A) and dehydrodipeptide **2** (B) -based hydrogels at 0.3 wt% (0.4 wt% in GdL) at different magnifications – scale bar: 2 μm (i) and 4 μm (ii).

The network of peptide **1**-based hydrogel presents a flexible ball-like structure (**figure 3.8 Ai**) due to the higher degree of fibre entanglement, where nucleation and fibre branching points are observed. In contrast, peptide **2**-based hydrogel displays a predominantly homogeneous network shaped by the rigid and regular arrangement of the fibres (**figures 3.8 Bi** and **3.8 Bii**). One can also note the higher network density of Nap-L-Lys(Cbz)-*Z*-ΔAbu-OH-corresponding hydrogel, resulting in a smaller mesh size.

We investigated the fibre thickness distribution and found that hydrogel **1** shows slightly thinner fibres than hydrogel **2**, with an average cross section of 42 ± 13 nm (versus an average of 56 ± 15 nm). **Figure 3.9** reveals that approximately 75% of the fibres feature a diameter between 20 and 50 nm in the former gel and between 40 and 70 nm in the latter.

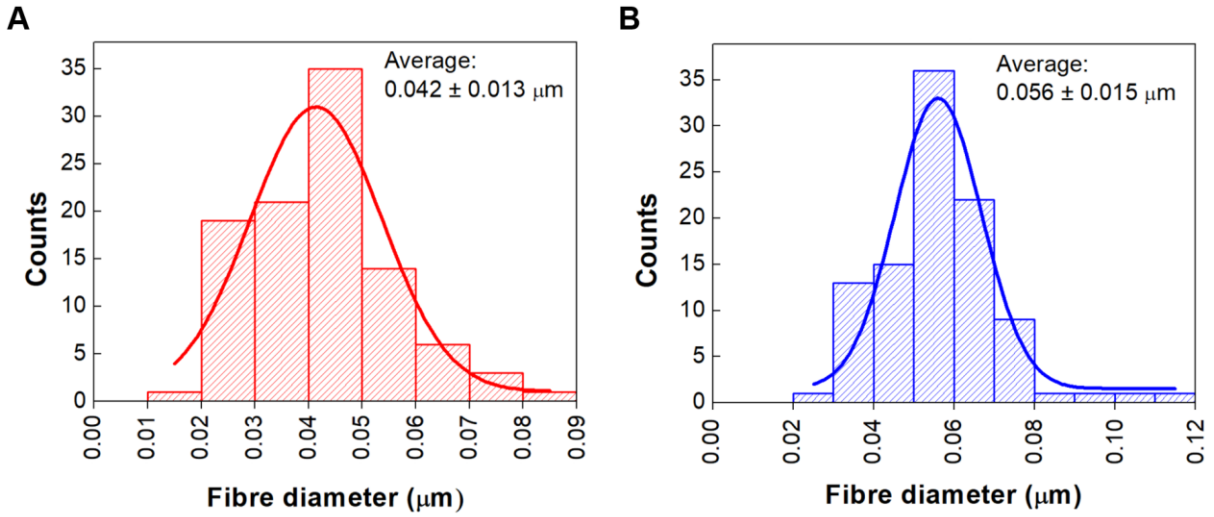

Figure 3.9 – Fibre diameter distribution of dehydrodipeptide **1**- (A) and dehydrodipeptide **2** (B) -based hydrogels at 0.3 wt% (0.4 wt% in GdL). Both histograms are fitted with a Gaussian function.

Indeed, the synthesised hydrogelators compose a more robust fibril network compared to similar *N*-capped dipeptides previously developed in our research group, including Npx-L-Phe-*Z*-ΔAbu-OH and Npx-L-Phe-*Z*-ΔPhe-OH (243). Such morphological characteristics are expected to impact and even regulate the mechanical behaviour of the hydrogels, as will be discussed below.

3.1.4 Hydrogels' rheological properties

Rheology is known as flow science. It focuses not only on studying the flow of fluids but also on the response of solids to deformation. In fact, these two states are often related because some deformation induced by shear forces causes solid-like materials to start flowing (245). Rheological studies often involve measuring the elastic modulus (G'), which represents the stiffness of the material, and the viscous modulus (G''), i.e., its flow properties, as function of time, oscillatory frequency, and oscillatory strain

amplitude (246,247). With these data, we have access to gelation kinetics, linear viscoelastic regions, and relaxation timescales. The main drawback of this technique is that it requires a trial-and-error approach because it is not possible to know *a priori* which values of stress, frequency and time are needed to reach equilibrium conditions and thus make the correct measurements (248). In this work, the rheological properties of hydrogels **1** and **2** were determined using the same preparation conditions (0.3 wt% compound and 0.4 wt% GdL) and protocol.

3.1.4.1 Time sweep

To study gelation kinetics, gel setting was followed for 10 h by applying an oscillatory strain amplitude of 10^{-3}% and a frequency of 1 Hz. The results are expressed in **figure 3.10**. Overall, G' and G'' values are well defined after 3 h for both gels, with hydrogel **1** requiring more time to reach equilibrium compared to compound **2**-based hydrogel.

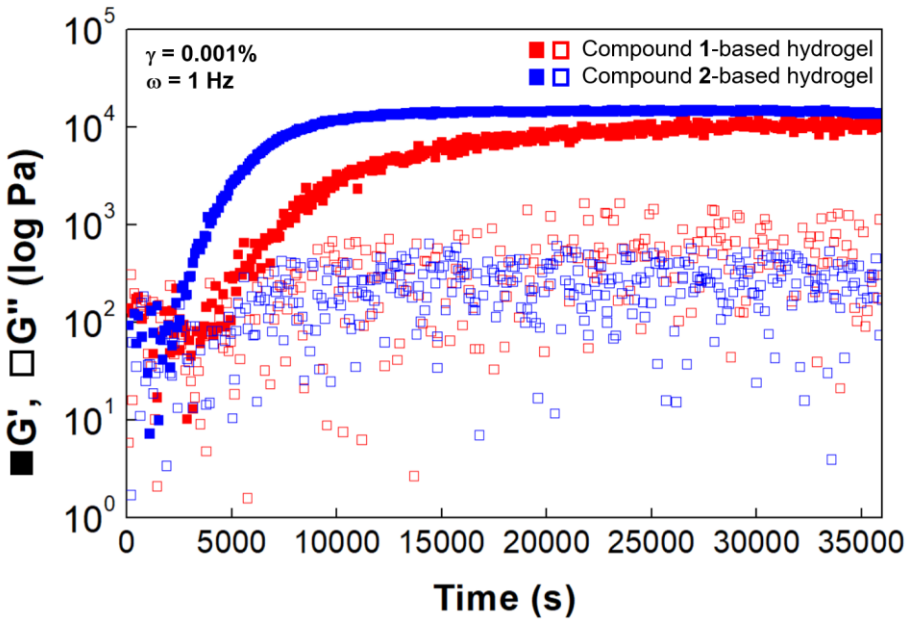

Figure 3.10 – Time dependence of elastic (solid symbols) and viscous (empty symbols) moduli for compound **1**- (red) and compound **2**- (blue) based hydrogels.

The gelation process of hydrogel **1** seems to be more complex. Initially, a lag time of approximately 5000 seconds is observed, in which the hydrogel elastic character is not measurable. Here, we testify the set of lower hierarchical structures whose elastic properties are not resolved by the rheometer; such assemblies are characteristic of a very weak gel, which is actually a "structure liquid" (249). This phenomenon is followed by a near-exponential growth of the elastic modulus, indicating a sol-gel transition, which slows down around 10000 and stabilizes after 25000 seconds from the beginning of the experiment; here, the G' is one order of magnitude larger than G'', demonstrating the formation of a

true self-supporting hydrogel. With a distinctly different behaviour, hydrogel **2** self-assembly occurs almost immediately after the addition of GdL – G' stands out from G'' in the first moments of the experiment (t<5000 seconds). After this period, there is a flattening of both moduli where the elastic modulus is about 50 times higher than the viscous one.

The longer sol-gel transition time of the peptide **1**-based hydrogel is expected given the deficit of an aromatic ring in the corresponding monomer structure regarding compound **2**. With the charge density decreasing after GdL addition, the primordial assemblies formed by hydrogelator **2** may undergo increased lateral association, in a process driven by its high hydrophobicity (237,250). Although the hydrogels turn out to display very similar elasticities during the timescale of the experiment, in the future, the gelation kinetics of hydrogel **1** should be followed for a longer period of time since some doubts remain concerning the reach of its equilibrium phase.

3.1.4.2 Frequency sweep

To obtain hydrogels' mechanical spectra (**figure 3.11**), the oscillatory frequency was swept from 0.024 to 100 Hz, with a strain amplitude fixed at 0.01%.

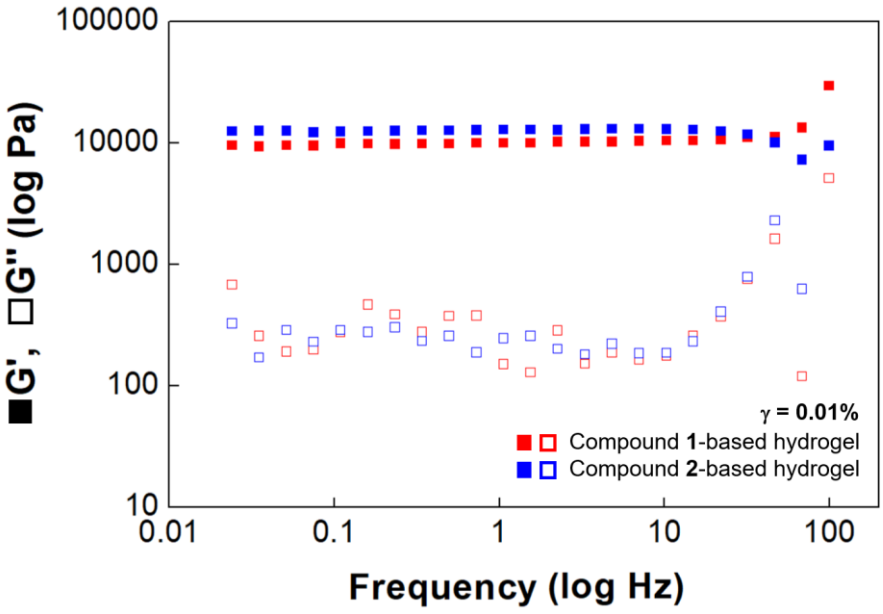

Figure 3.11 – Frequency dependence of elastic (solid symbols) and viscous (empty symbols) moduli for compound **1**- (red) and compound **2**- (blue) based hydrogels.

Despite the different gelation kinetics, the mechanical spectra confirm the similarity of the elastic moduli of hydrogels **1** and **2**. Accordingly, the additional aromatic ring of compound **2** does not significantly impacts the strength of the network neither its response under increasing oscillatory frequencies. In fact, both hydrogels exhibit a frequency-independent elastic modulus, 50 – 70 times higher than the

corresponding viscous modulus (**table 3.2**), which makes up mechanical spectra characteristic of solid-like materials.

Table 3.2 – Rheological properties of hydrogels collected from the corresponding mechanical spectra.

	Dynamic frequency sweep	
	G' (Pa)	*G''* (Pa)
Compound 1-based hydrogel	9990	151
Compound 2-based hydrogel	12900	246

At a lower compound concentration (0.3 wt%), these hydrogels achieve elastic moduli considerably higher than those of the reported *N*-capped dehydrodipeptides, e.g., Npx-L-Trp-*Z*-ΔAbu-OH (0.4 wt%, 5.74×10^3 Pa) and Npx-L-Phe-*Z*-ΔPhe-OH (0.4 wt%, 1.6×10^3 Pa) (236). This consistency matches that described for tissues subjected to high mechanical activity, such as bone, muscle, and cartilage. Further, tumorigenesis often involves an increase in tissue hardness (251), which makes both hydrogels promising for application in cancer treatment.

3.1.4.3 Amplitude sweep

Although the hydrogels demonstrate similar inertia towards strain frequency, the amplitude sweeps proved that compounds **1** and **2** produce networks quite different in terms of response to increasing strain intensities. This was concluded by changing the strain amplitude from 0.001 to 200% at a fixed frequency of 1 Hz (**figure 3.12**).

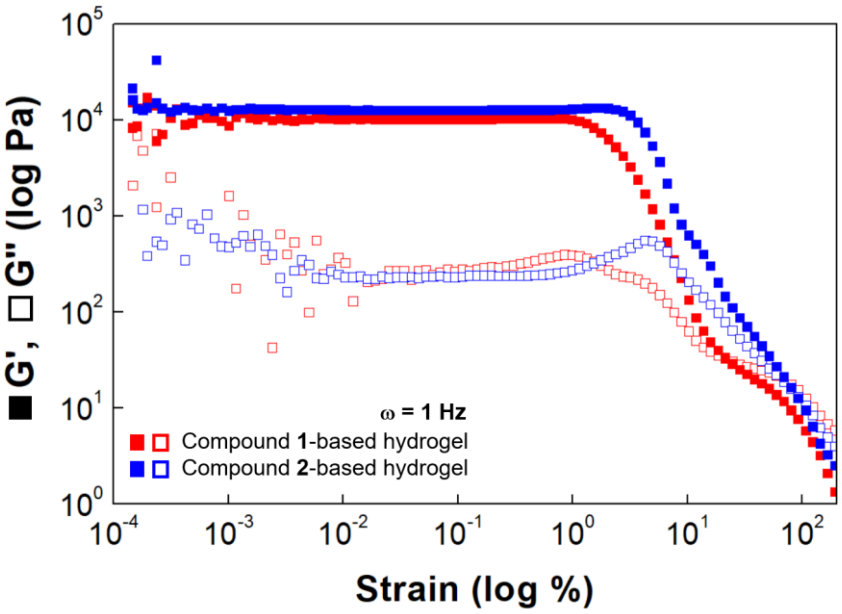

Figure 3.12 – Amplitude dependence of elastic (solid symbols) and viscous (empty symbols) moduli for compound **1**- (red) and compound **2**- (blue) based hydrogels.

The results show that the elastic moduli of the hydrogels are similar and remain stable up to an amplitude of 1%, which allows us to define such interval as the SAOS regime (252). By increasing the amplitude, both gels switch to a non-linear regime and the so-called LAOS response takes off (252). Here, both G' and G'' of hydrogel **1** start to gradually decrease until they cross. This profile is common in strain-thinning or type I materials, as classified by Hyun in 2002 (253). It consists of the soft reduction of both moduli as the amplitude increases and results from fibre disentanglement and alignment according to flow direction. This phenomenon is found in shear-thinning polymers and characterizes simple viscoelastic materials (254,255). On the contrary, LAOS of hydrogel **2** is marked by a local maximum in the viscous modulus at intermediate amplitudes (weak strain overshoot), followed by a decrease of both G' and G''. This behaviour is described as the Payne effect and results from the resistance of plastic-like materials to structural rupture. The explanation of strain overshoot remains a mystery, but several theories include amplitude-dependent build up/break down, intra- and interparticle transitions, length scale-dependent rearrangement and forced strain relaxation (254,255).

Ultimately, hydrogel **1** exhibits a softer character, while hydrogel **2** undergoes rearrangements in structure before seeing its fibres align in the direction of flow. **Table 3.3** also shows the higher energy required for the breakdown of the latter which is justified by the higher stiffness of the fibres (visible in **figure 3.8 B**) resulting from the larger number of interactions between the corresponding monomers (225).

Table 3.3 – Hydrogels' moduli under SAOS and breaking strain. The latter corresponds to the point where G' equals G''.

	Dynamic amplitude sweep		
	G' (Pa)	G'' (Pa)	Breaking strain (%)
Compound 1-based hydrogel	10300	343	24.9
Compound 2-based hydrogel	12700	241	93.1

Although the hydrogels arising from the synthesised dehydrodipeptides present differences in several aspects, their magnitude is not determinant for the selection of the hydrogelator that will proceed to the next stage of this work. However, given the extreme hydrophobicity of dehydrodipeptide **2** and challenging preparation of the respective hydrogel precursor solutions, we chose hydrogelator **1** for further functionalization. So henceforth, any mention of a hydrogelator and/or hydrogel in this thesis will refer to compound **1** and the corresponding hydrogel, respectively.

3.2 PLASMONIC MAGNETOLIPOSOMES

3.2.1 Manganese ferrite nanoparticles

3.2.1.1 Synthesis, size, and magnetic properties

Manganese ferrite nanoparticles are attractive regarding other spinel structures due to their high magnetic susceptibility, good biocompatibility, and toxicity against HeLa cells (74). Naturally, the synthesis method influences their shape, size, surface chemistry and magnetic properties. Thus, in view of the low cost and short timescale, in this work, the aqueous co-precipitation method was adopted (256). As the tuning of particle size and magnetic properties remains a challenge (256), we chose to vary the salts molar ratio, ionic strength and sequence of reagents addition around the conditions already reported for $MnFe_2O_4$ NPs' synthesis (MF5) (213), as summarized in **table 3.4**.

Table 3.4 – Reaction conditions of the different synthesised manganese ferrite nanoparticles and those described in (213) (highlighted).

Label	Mn^{2+}/Fe^{2+} molar ratio	Citrate concentration (M)	Synthetic methodology
MF4	0.4	0.05	Co-precipitation
MF5 (213)	*0.5*	*0.05*	*Co-precipitation*
MF6	0.6	0.05	Co-precipitation
MF5_C0	0.5	0	Co-precipitation
MF5_rev	0.5	0.05	Reverse co-precipitation

MF4 and **MF6** syntheses consisted in ranging the Mn^{2+}/Fe^{2+} molar ratio from 0.4 to 0.6 in order to enhance the magnetic properties of $MnFe_2O_4$ precipitates. In addition, the impact of (the absence of) citrate ions and of the sequence of reagents addition on NP size distribution in water was studied with **MF5_C0** and **MF5_rev** nanoparticles. Actually, we first characterized the NPs with respect to the hydrodynamic diameter distribution, as listed in **table 3.5**.

Table 3.5 – Hydrodynamic diameter and polydispersity index of the synthesised manganese ferrite nanoparticles.

	Hydrodynamic diameter (nm)	PDI (%)
MF4	20.23	21.07
MF6	15.97	29.43
MF5_C0	99.27	37.06
MF5_rev	7.13	32.12

The extremes in size stand out, with **MF5_C0** showing the largest diameter and **MF_rev** displaying the smallest. For increasing Mn^{2+} concentrations, where citrate and normal co-precipitation were employed, the size reduction of **MF6** regarding **MF4** is probably related to the lower rate of crystal growth caused by the reduced concentration of Fe^{2+} ions (257). The NPs synthesised in the absence of citrate (**MF5_C0**) turned out to be larger than the others, also presenting a higher polydispersity. This can result from the generation of large clumps after nucleation conducted by van der Waals forces (258). In fact, citrate ions provide a negative charge to NPs' surface in opposition to those attractive forces, allowing a uniform crystal growth. Differently, the reduced size of **MF_rev** NPs was expected, considering some literature reports. Aono *et al.* demonstrated that the gradual pH increase carried out in normal co-precipitation reactions causes the enlargement of crystallites and particles' final size; now, if reverse co-precipitation involves the introduction of the precursor salts in an alkaline solution, the small dimensions found for **MF5_rev** NPs are reasonable (259,260).

Regarding the magnetic properties, the observable reaction of the synthesised NPs to the approach of a magnet consisted of an increasing intensity in the following order: MF6 < MF5_rev < MF4 ≈ MF5_C0. Indeed, by placing the magnet at the same distance from each sample (6 – 7 cm), we noticed that **MF6** and **MF5_rev** NPs did not show significant magnetism, as illustrated in **figures 3.13 B** and **3.13 D**. Contrarily, **MF4** and **MF5_C0** NPs were clearly aligned under the effect of a magnetic field (**figures 3.13 A** and **3.13 C**).

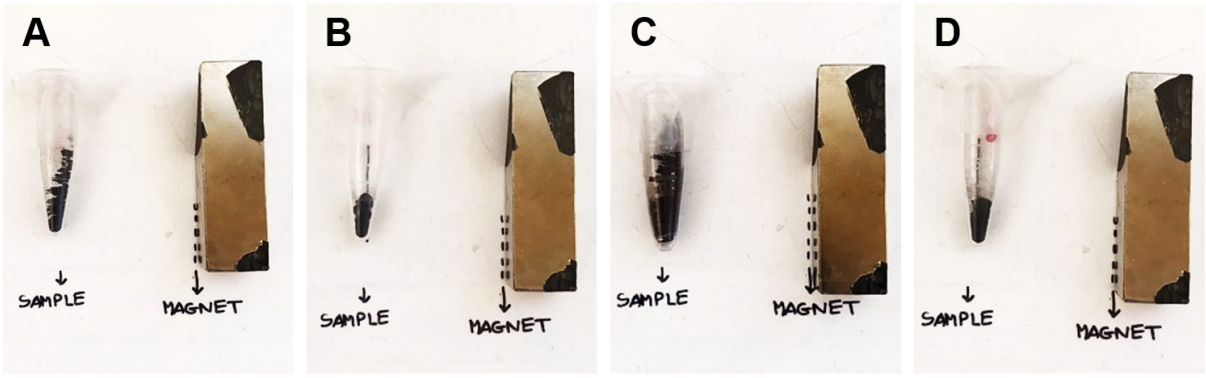

Figure 3.13 – Observable magnetic behaviour of **MF4** (A), **MF6** (B), **MF5_C0** (C) and **MF5_rev** (D) nanoparticles under the effect of a magnet placed at a distance of 6 – 7 cm.

To resolve the magnetic properties of the latter, we quantitatively investigated their magnetisation as a function of the applied magnetic field (**figure 3.14**) and compared the results with the reference particles MF5. The corresponding magnetic parameters are tabulated in **table 3.6**.

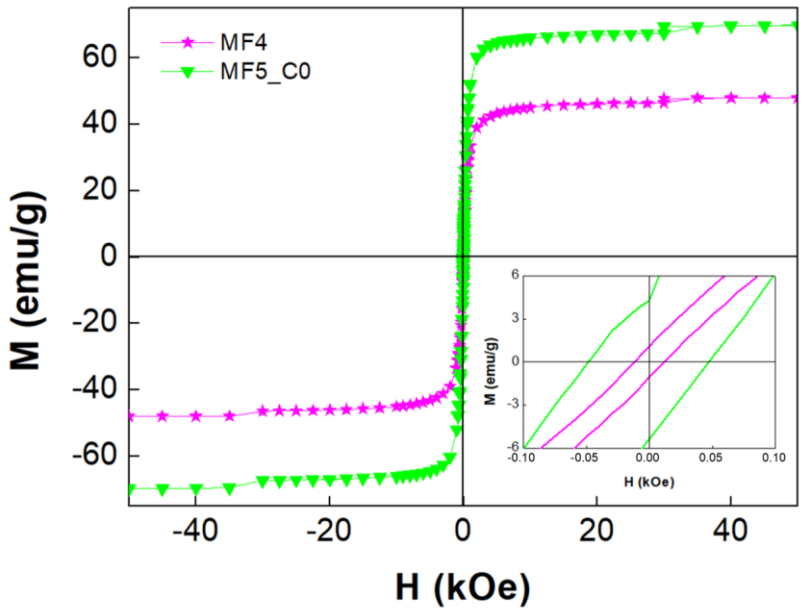

Figure 3.14 – Hysteresis loops of the synthesised **MF4** (pink stars) and **MF5_C0** (green triangles) nanoparticles. The inset shows the small coercivity of the materials.

Both M–H loops are quite narrow at room temperature. Although the **MF5_C0** particles demonstrate higher coercivity and remanent magnetisation, both nanoparticles exhibit superparamagnetic behaviour as indicated by the M_r/M_s ratio less than 0.1 (75). Overall, the highest saturation magnetisation is observed for the nanoparticles synthesised with no citrate and the lowest M_s is assessed to the nanoparticles with smaller manganese content.

Table 3.6 – Saturation magnetization (M_s), coercivity (H_c), remanent magnetization (M_r) and M_r/M_s ratio of the synthesised **MF4** and **MF5_C0** and of the reported MF5 nanoparticles (highlighted).

	$M_s\ (emu/g)$	$H_c\ (kOe)$	$M_r\ (emu/g)$	M_r/M_s
MF4	48.04	12.08	1.05	0.022
MF5_C0	69.89	46.69	4.27	0.061
MF5 (213)	*52.0*	*33.4*	*5.4*	*0.10*

We shall first discuss the magnetic differences observed for the **MF4** and the reported MF5 particles. Manganese ferrites' magnetic properties depend directly on the particle size and cation distribution in the spinel structure. In $MnFe_2O_4$ nanoparticles, 20% of Mn^{2+} ions occupy octahedral lattice sites, so that the general distribution is $(Mn_{0.8}Fe_{0.2})[Mn_{0.2}Fe_{1.8}]O_4$ (curved brackets represent A sites (tetrahedral) and square brackets denote B sites (octahedral)) (261–263). Comparing **MF4** particles (which actually correspond to $Mn_{0.86}Fe_{2.14}O_4$) with the reported MF5 ($MnFe_2O_4$), it is noted that the increase in manganese content leads to the M_s enlargement. Mn^{2+} ion has 5 unpaired electrons, while the Fe^{2+} has

only 4; thus, when Fe^{2+} is replaced by Mn^{2+} in the octahedral sublattice, the magnetization becomes greater, as it is determined by the exchange interaction between the ions at the A and B sites, according to the following equation (261):

$$\mu_{theor} = \mu_B + \mu_A \qquad (3.1)$$

where μ_{theor} is the net magnetic moment *per formula* and μ_A and μ_B are the magnetic moments of the cations in the A and B voids, respectively. However, when we continue to increase manganese content, manganese ions become oxidized to Mn^{3+} (four unpaired electrons) and start occupying the B voids in the crystal lattice, reducing the exchange interaction between the A and B sites, and thus, decreasing M_S (261,262). This is the reason why **MF6** NPs, which are actually $Mn_{1.64}Fe_{1.36}O_4$, exhibit a small magnetic response, visible in **figure 3.13**.

Nevertheless, when we compare the NPs synthesised in the absence of citrate **MF5_C0** and its MF5 analogues, it is evident that the first ones have a much higher M_S. Indeed, although citrate endows NPs with good dispersibility in water, its diamagnetic organic character cannot be ignored, since it cancels part of the magnetic moments of the particles.

3.2.1.2 Evaluation as magnetic hyperthermia agents

Magnetic hyperthermia experiments were carried in water, at a concentration of 1 mg/mL in NPs (0.1 wt%). The heating curves for different values of external AMF strength and frequency were obtained, considering the $H - f$ product tolerated by living tissues. **Figure 3.15** shows the temperature-time plots for **MF4** and **MF5_C0** nanoparticles and **table 3.7** lists the corresponding achieved SLP and ILP (intrinsic loss power) values. The former is defined as the electromagnetic power loss per mass unit of fluid and expresses in watt per gram. In other words, that term evaluates the magnetic heating efficiency of MNPs and to calculate it, the following equation is usually employed:

$$SLP = \frac{\Delta T \times C}{\Delta t \times m/V_S} \qquad (3.2)$$

where C is the volumetric specific heat capacity of the solution, m is the mass of MNPs in solution and V_S is the sample volume. To make it easier to compare the heat conversion efficiency of MNPs under different magnetic fields, it is necessary to remove H and f factors. This results in ILP (**equation 3.3**), which is independent of the magnetic field parameters.

$$ILP = \frac{SLP}{H^2 \times f} \qquad (3.3)$$

Looking at **figure 3.15**, different behaviours are observed for **MF4** and **MF5_C0** NPs, with the former reaching higher temperatures for all tested conditions. Although we thought that the magnetic properties determined previously would accordingly shape NPs' magnetic hyperthermia profiles, several studies in the literature argue that there is no correlation between the saturation magnetization or magnetic moment of a single particle and the specific absorption power, or SLP, in the superparamagnetic regime.

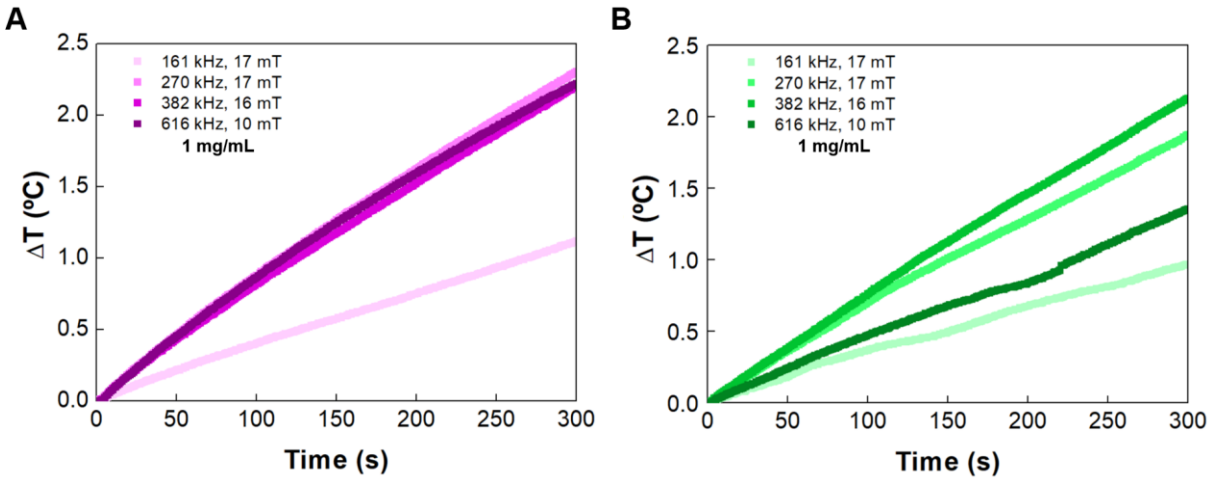

Figure 3.15 – Temperature variation over time of **MF4** (A) and **MF5_C0** (B) nanoparticles (0.1 wt%), in water, under different magnetic field strengths and frequencies.

On the other hand, the heating efficiency strongly depends on the average size, size distribution and agglomeration of MNPs. Interestingly, **table 3.7** reveals that **MF4** NPs, being smaller, have higher SLP than **MF5_C0** NPs and that this difference is enhanced for an AMF of 7.96 kA/m, 616 kHz. In fact, there are data suggesting that the optimal diameter for maximum SLP has to be close to the critical size of the single-to-multi domain transition for the manganese ferrite phase (264,265); in this sense, it is possible that the **MF4** present a closer diameter than **MF5_C0** NPs. Moreover, the wide size distribution of **MF5_C0** NPs indicates that the absence of citrate upon synthesis not only favours interparticle interaction-induced cluster formation, but also the genesis of particles with various sizes. Although those interactions may be favourable due to the eventual transition from the superparamagnetic to a pseudo-single domain regime, the diversity of sizes may involve coercivities that are not exceeded by the AMF amplitude (264,265).

Table 3.7 – Calculated magnetic hyperthermia parameters for the synthesised **MF4** and **MF5_C0** nanoparticles in solution at 0.1 wt%.

	H $(kA\,m^{-1})$	f (kHz)	$H \times f$ $(\times 10^9 A\,m^{-1}\,s^{-1})$	SLP (W/g)	ILP $(\mathrm{n}Hm^2/kg)$
MF4	13.53	161.00	2.18	15.90	0.54
	13.53	270.00	3.65	35.15	0.71
	12.73	382.00	4.86	32.64	0.53
	7.96	616.00	4.90	35.15	0.90
MF5_C0	13.53	161.00	2.18	14.23	0.48
	13.53	270.00	3.65	28.45	0.58
	12.73	382.00	4.86	31.38	0.51
	7.96	616.00	4.90	19.25	0.49

We further compared these NPs with the reported MF5 (213), where the same experimental conditions were used. It is found that for higher $H \times f$ products, the NPs synthesised in this work reach slightly lower temperatures than the MF5. This can be explained by the different stoichiometry in the spinel ferrite arising from the different Mn/Fe ratio, in the case of **MF4**, and the absence of citrate for **MF5_C0** NPs. Furthermore, the particles are expected to vary in size and propensity to aggregate, as will be confirmed by the upcoming TEM data.

3.2.1.3 Morphology and crystal structure

The TEM micrographs in **figure 3.16** show the morphology (size, shape, and degree of aggregation) of **MF4** and **MF5_C0** nanoparticles. Both syntheses resulted in particles with nearly spherical shape, with the **MF4** NPs presenting individual sizes of 17.54 ± 4.02 nm and the **MF5_C0** of 72.0 ± 32.11 nm with very well-defined edges owing to the absence of the organic coating layer (citrate).

The histograms in **figure 3.17** show the particle size distribution, where **MF4** NPs appear to be more uniform while **MF5_C0** take a much wider size spectrum, with a minimum of 15.62 nm and a maximum of 165.29 nm. These results are in good agreement with the hydrodynamic diameter and dispersity measurements listed in **table 3.5**. The slightly higher values of the latter are explained by the fact that DLS technique considers, in addition to the metal core, the solvation sphere of the nanoparticles as well as the occurrence of infrequent aggregates.

These data are actually very useful in further explaining the different M_s values of the synthesised **MF4** and the reported MF5 NPs since, as stated earlier, along with the cation distribution in the sublattices,

the particle size plays a key role in defining the magnetic properties of the materials. Although MF5 particles present a higher M_S than the synthesised **MF4** due to the higher Mn^{2+}/Fe^{2+} ratio, the difference is smaller than expected. This results from the described smaller size of the former (14.4 ± 2.6 nm) (213); in fact, it is reported elsewhere (262) that smaller particles have lower M_S owing to a higher surface/volume ratio and surface spin disorder. It follows that, to find the optimal NPs in the $Mn_xFe_{3-x}O_4$ series, it is necessary to find a compromise between those two factors.

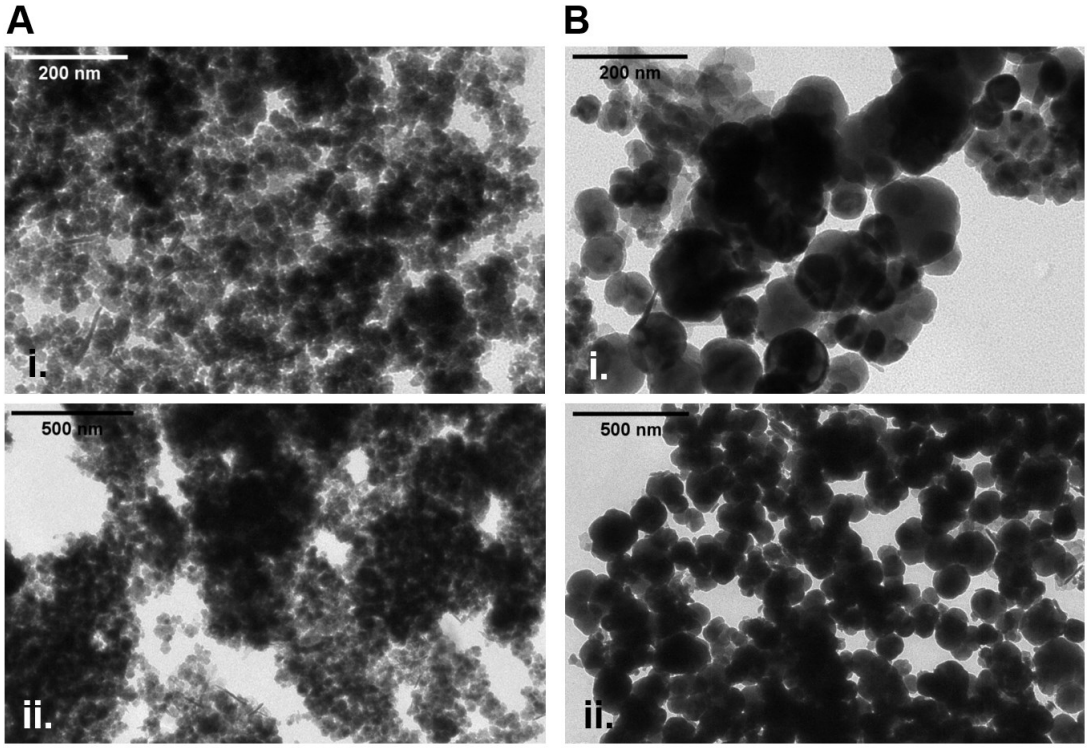

Figure 3.16 – TEM images of **MF4** (A) and **MF5_C0** (B) nanoparticles at different magnifications – scale bar: 200 nm (i) and 500 nm (ii).

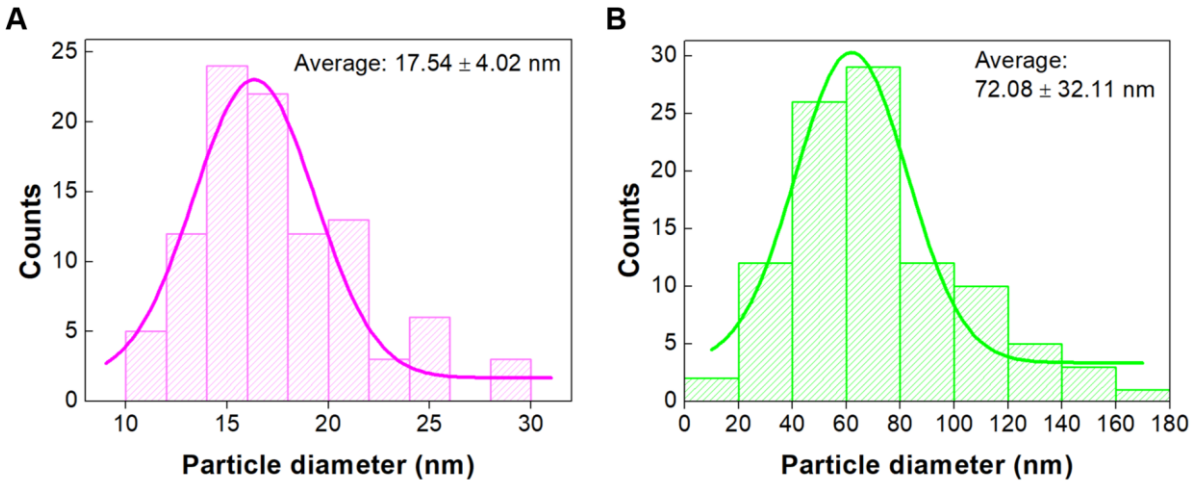

Figure 3.17 – Diameter distribution of **MF4** (A) and **MF5_C0** (B) nanoparticles. Both histograms are fitted with a Gaussian function.

The data discussed so far allowed us to select the manganese ferrite nanoparticles that would proceed to the next stage of the present work, by carefully weighting their magnetic properties and size distribution. We therefore chose **MF4** NPs given their suitable size, good dispersity, negligible remanent magnetization, and promising heating capabilities, which are very important aspects for biomedical applications besides the saturation magnetization.

To achieve further insight into the spinel structural information of the selected nanoparticles, X-ray diffraction technique was performed, and the results were fitted by *FullProf software* (266) on the basis of Rietveld refinement (**figure 3.18**).

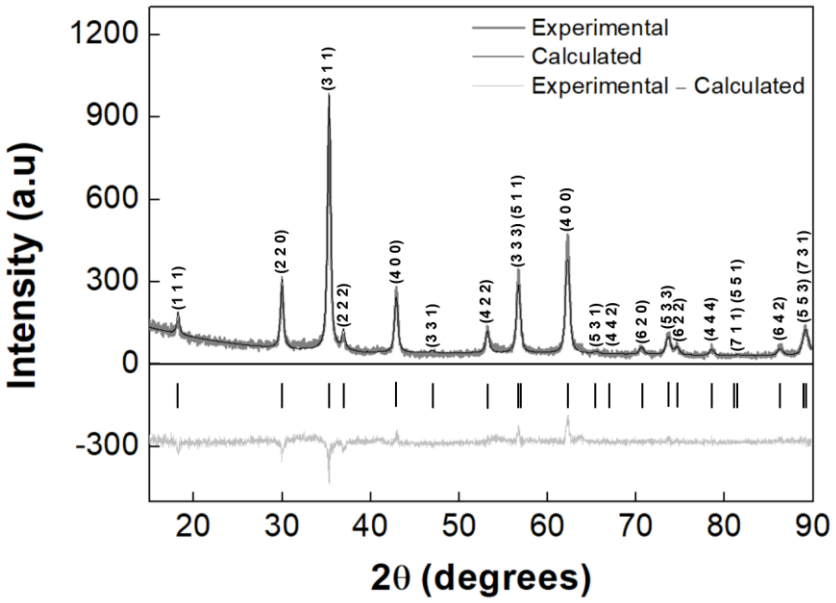

Figure 3.18 – X-ray diffraction pattern of **MF4** nanoparticles. Dark grey lines: experimental pattern; black lines: calculated pattern; light grey lines: calculated pattern subtracted to the experimental one; vertical lines: Bragg diffraction positions. Miller indices are indicated in black.

The background used in the fit is described by a linear interpolation. A well-defined pattern is observed, with the peaks of the spinel structure presenting a width at half-maximum less than 2° 2θ, which reveals the crystalline character of **MF4** nanoparticles even without calcination. Those signals are found at 2θ = 18.2 (1 1 1), 29.9 (2 2 0), 35.3 (3 1 1), 36.9 (2 2 2), 42.9 (4 0 0), 46.9 (3 3 1), 53.2 (4 2 2), 56.7 (3 3 3) and (5 1 1), 62.2 (4 4 0), 65.4 (5 3 1), 66. 5 (4 4 2), 70.6 (6 2 0), 73.6 (5 3 3), 74.6 (6 2 2), 78.5 (4 4 4), 81.4 (7 1 1) and (5 5 1), 86.2 (6 4 2), 89.1 (5 5 3) and (7 3 1), according to CIF file 1528316 (space group Fd-3m). **Table 3.8** shows the parameters determined for the refinement and the R_F value translates a reasonable fit. The calculated particle size (18.6 nm) must be highlighted given its similarity with the experimental value determined by TEM data.

Table 3.8 – Calculated particle size, R_F and χ^2 obtained by Rietveld refinement of the X-ray diffraction pattern of **MF4** nanoparticles. SD: standard deviation.

Phase size ± SD (nm)	R_F	χ^2
18.6 ± 0.12	4.41	1.57

3.2.2 Manganese ferrite/gold core/shell nanoparticles

3.2.2.1 Synthesis and spectroscopic characterization

We first passivated **MF4** NPs with APTES in view of extra advantages, such as, enhanced dispersion in water, prevention of leaching under acidic environments and the possibility of conjugation with biomolecules or metals, namely gold (Au) (217). As previously mentioned, the combination of magnetic materials with metals is of interest as it allows to obtain simultaneously magnetic and optical responses. In order to prepare these nanocomposites in the form of gold-decorated manganese ferrite spheres, we promoted the adsorption of the co-precipitated **MF4** to gold nanoparticles that were previously synthesised in the presence of citrate, which acted both as reducing agent and stabilizer. The UV-Vis absorption profile of the latter is shown in **figure 3.19**.

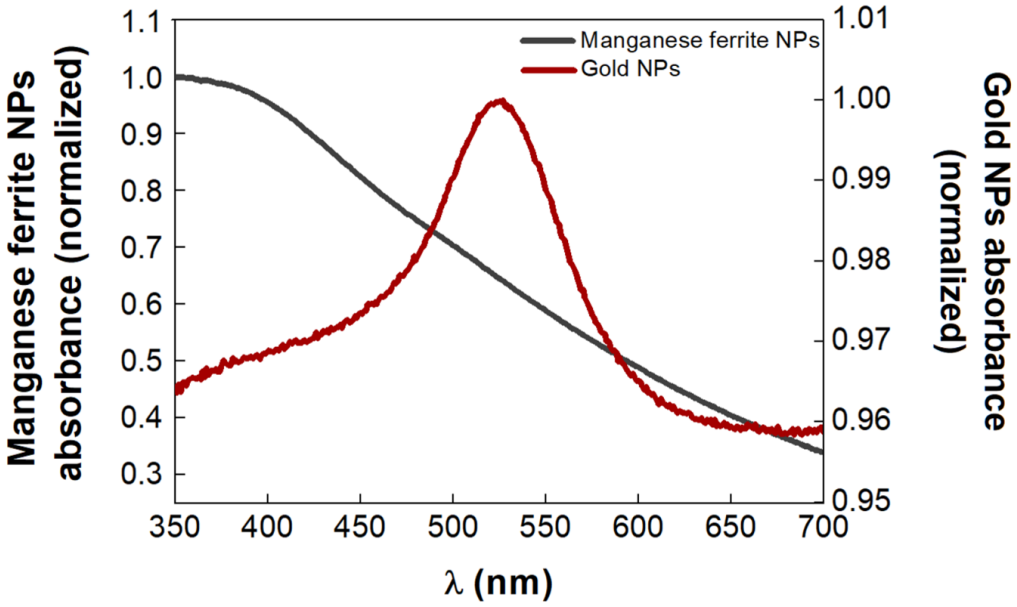

Figure 3.19 – UV-Vis absorption spectra of **MF4** nanoparticles (grey line) and citrate-capped gold nanoparticles (deep red line) in ultrapure water.

Those Au NPs display resonance at a wavelength of 530 nm, which can be associated with spheres of approximately 10 – 13 nm in diameter, as explained in literature (267,268), making them suitable for subsequent coating of the visible-silent magnetic cores. The adsorption resulted from the successive injection of **MF4** aliquots into the aqueous solution of gold nanoparticles, under vigorous stirring, until a

colour change was noticed. **Figure 3.20** illustrates this process, in which each spectrum was obtained after injection of 100 μL of **MF4** NPs (4 mg/mL).

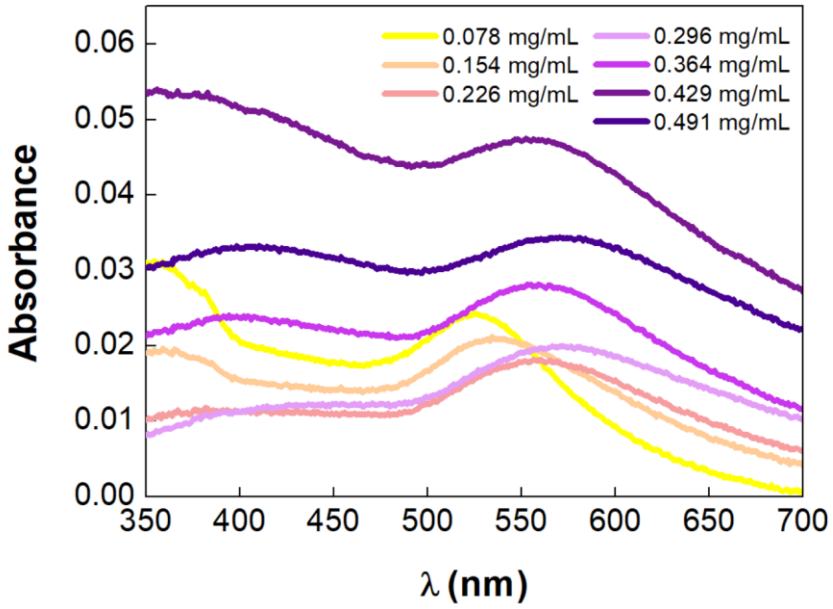

Figure 3.20 – UV-Vis absorption spectra of gold-decorated **MF4** nanoparticles with different manganese ferrite nanoparticles' concentrations in ultrapure water.

It is evident that the absorption spectra in **figure 3.20** express contributions from the magnetic (around 400 nm) and gold (500 – 650 nm) nanoparticles. However, effective adsorption of Au spheres to the surface of the magnetic material is only achieved after a concentration of 0.226 mg/mL in **MF4** NPs because of the red shift in gold plasmon band (from 530 to 570 nm); the latter is induced by the powerful interactions and coupling of surface plasmons between adjacent gold nanoparticles (269,270).

This unreported method is attractive, considering its simplicity, reduced timescale, and the fact that it is done in an aqueous medium. The effective attachment of the metal NPs to the magnetic nanospheres is ascribed to two main factors: the small size of the latter, endowing them with a large surface area available for conjugation, and presence of the positively charged APTES; this aminosilane avoided **MF4** NPs' agglomeration, allowing the homogeneous distribution of gold over their surface, and promoted strong electrostatic interactions between its NH_3^+ moiety and the COO^- groups of citrate ions in Au surface (271).

After **MF4** NPs gold-modification, shell growth was conducted in the presence of hydroxylamine. This reagent only further reduces $HAuCl_4$ on the surface of pre-existing gold nanoparticles, hence the earlier-described procedure. The result is a dense layer that provides a blackberry-like shape to the nanoparticles, as schematised in **figure 3.21**.

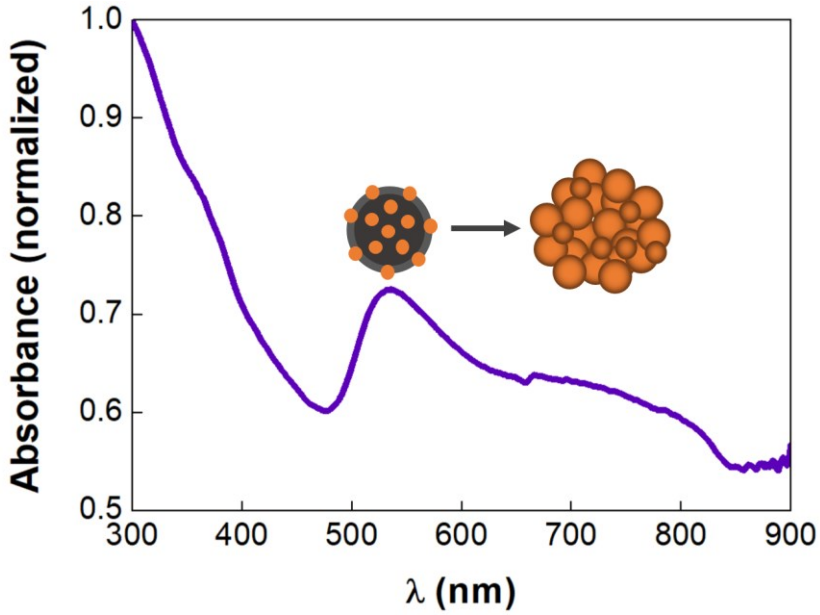

Figure 3.21 – Schematic representation of gold-shell growth and absorption spectrum of manganese ferrite/gold core/shell nanoparticles in ultrapure water.

UV-vis-NIR absorption spectroscopy supported the successful preparation of the core/shell system because of the enhancement of the NIR absorption as described in reference (220). The highly rough topography of the surface is responsible for higher order multipole resonances (220), observed in peaks at 535 and at 670 nm, which extend up to 830 nm. In fact, when the particle/shell becomes radially inhomogeneous and its size increases, a description in terms of dipolar contributions, i.e., the Mie model, is no longer adequate since dipolar localized surface plasmon no longer dominates (143). This kind of structures is promising from a fundamental point of view as they are found in many biological systems such as cell organelles (272). Obviously, the long absorption handrail obtained with the synthesised magnetic-core/plasmonic-shell nanoparticles is very useful as biological tissues have low absorption and high penetration in the 700 – 900 nm window (273); therefore, we envision their application in laser-induced photothermia to destroy cancer cells through a non-invasive approach (274).

3.2.2.2 Evaluation as photothermal agents

The photothermal performance of MF4/Au core/shell NPs was evaluated in aqueous solution (1 mg/mL, 0.1 wt%), under NIR irradiation (808 nm) with two continuous lasers (500 and 800 mW) (**figure 3.22**); for the lower power laser, two power density levels were tested: 2.4 W/cm^2 and 5 W/cm^2, for irradiated areas of 21 and 10 mm^2, respectively.

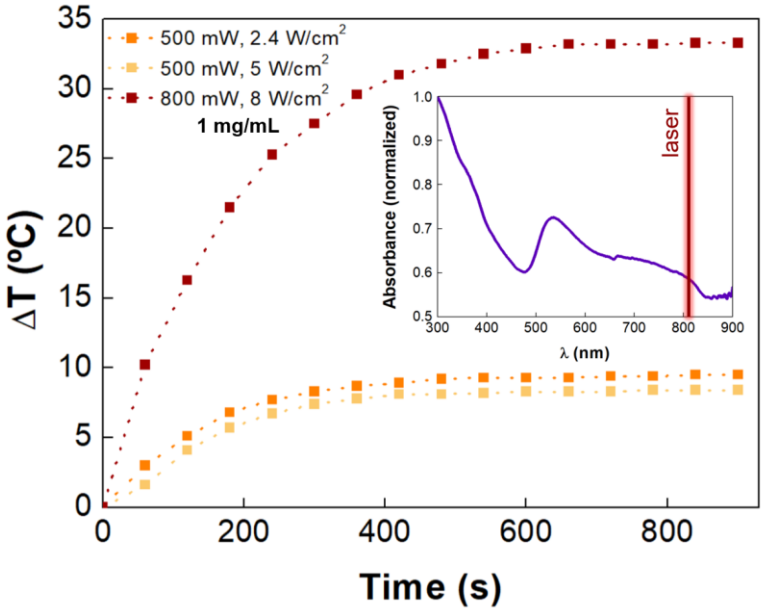

Figure 3.22 – Temperature variation over time of MF4/Au core/shell nanoparticles (0.1 wt%) in ultrapure water under different irradiation conditions. Inset: positioning of the lasers' wavelength on the NPs' absorption spectrum.

The dependence of the temperature increase on the irradiation power was demonstrated. After 15 minutes, core/shell nanoparticles increased the solution temperature by ~10 °C for a power density of 2.4 W/cm^2, 8 °C for 5 W/cm^2 and 33 °C for 8 W/cm^2. Indeed, the condition that promoted the greatest heating efficiency was the one relative to 8 W/cm^2 irradiance, with an initial rate of 7 °C/min. Interestingly, with the 500 mW laser, a lower irradiance results in a higher final temperature of the NP solution. This is attributed to the preponderance of the irradiated area over the power per unit area, as it is more advantageous to cover as many nanoparticles as possible simultaneously. We believe that the irregular gold structures aggregated around the magnetic core are responsible for the significant heating of the medium, through a collective heating effect. Here, each shell unit contacts with its neighbouring unit, forming adherent spots, which locally increase the electromagnetic field and thus the efficiency of radiation-to-heat conversion (275).

For cancer therapy, a balance between photothermal performance and irradiation power is required, as high-power densities cause unnecessary cell damage (276). Accordingly, for 0.1 wt% in MF4/Au NPs, the use of the 500 mW laser at 2.4 W/cm^2 promises a relevant local elevation of body temperature for tumour tissue destruction, without significant side effects. In the future, concentration studies will be carried out to find the optimal particle dose to allow precise control of photothermia by adjusting the irradiation power of the external laser.

3.2.3 Plasmonic magnetoliposomes

3.2.3.1 Synthesis and spectroscopic characterization

Aqueous plasmonic magnetoliposomes (plasmonic AMLs) were prepared by ethanolic injection of the zwitterionic lipid DPPC (for a final concentration of 1 mM) into the aqueous solution of the synthesised magnetic-core/plasmonic-shell nanoparticles (0.1 wt%). This technique was chosen owing to its simplicity and the possibility of loading hydrophobic drugs (e.g., PTX) into the magnetoliposomes by co-injection. UV-Vis absorption spectroscopy was used to characterise the plasmonic AMLs and to investigate the differences with respect to their individual components, i.e., DPPC-based liposomes, MF4/Au core/shell nanoparticles and a mixture of both. These structures were synthesised for the same concentration of lipids and/or magneto-plasmonic nanoparticles as plasmonic magnetoliposomes.

As we saw in section 3.2.2.1, MF4/Au core/shell NPs exhibit a well-defined broad band with a maximum at 535 nm that extends to NIR region. On the other hand, DPPC liposomes exhibit a completely different absorption profile, as visible in **figure 3.23**; this is rather noisy owing to lipids' light scattering and no peak is observed in the studied wavelength range since DPPC has an absorption maximum located at 221 nm (277). When we place liposomes and the core/shell nanoparticles in the same cuvette, it is observed that the higher-order multipole bands are quenched, while the 535 nm peak is kept. Differently, measuring the absorption of plasmonic AMLs, the contribution of the gold shell is proportionally attenuated for all resonances, which indicates that the incorporation of MF4/Au NPs into liposomes was successful.

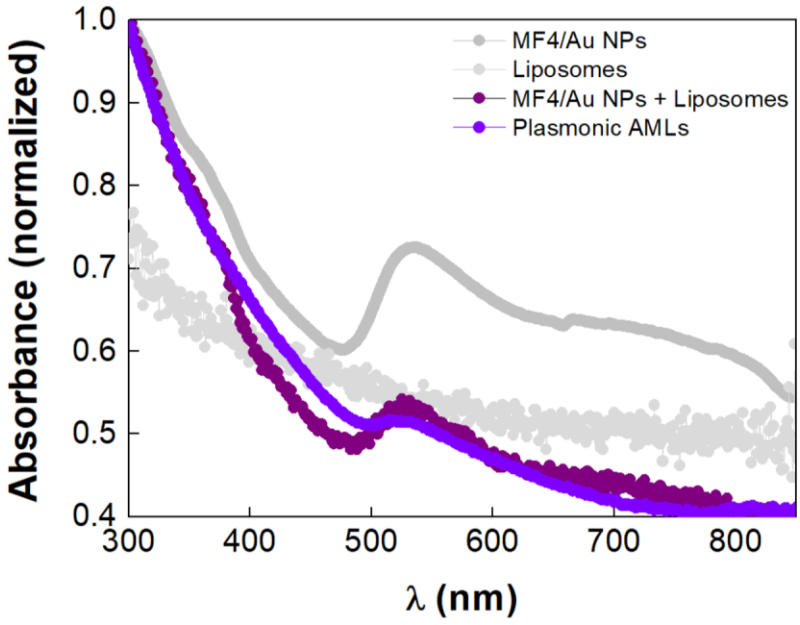

Figure 3.23 – UV-Vis absorption spectra of MF4/Au core/shell nanoparticles, DPPC-based liposomes, mixture of MF4/Au nanoparticles and liposomes and plasmonic AMLs in ultrapure water.

3.2.3.2 Size and surface charge

The hydrodynamic size of the plasmonic AMLs (359.76 nm), shown in **table 3.9**, turn out to be almost 5 times larger than bare core/shell NPs and approximately three times larger than liposomes (without MF4/Au nanoparticles). This demonstrates the possibility of incorporation of several nanoparticles by each AML. A second diameter contribution (64.51 nm) with large expression in number is attributed to core/shell nanoparticles that were not encapsulated. The size of the synthesised AMLs is considerably higher than those reported in (278) and (75) for plasmonic MLs, owing to smaller magnetoplasmonic nanoparticles, different lipid coatings and particular architectures; the former author used a mixture of DPPC and octadecylamine and the latter dioleoylphosphatidylglycerol (DOPG). Nonetheless, the application of a DPPC bilayer is advantageous, as DPPC membranes present a phase transition at 41 °C (78), which coincides with the temperature of mild hyperthermia, thus promoting a potential increase in drug release (222).

Table 3.9 – Hydrodynamic diameter, polydispersity index and ζ-potential of MF4/Au core/shell nanoparticles, DPPC-based liposomes and plasmonic AMLs.

	Hydrodynamic diameter (nm)	**PDI (%)**	**ζ – potential (mV)**
MF4/Au NPs	74.98	26.64	-25.67
Liposomes	125.83	28.61	-5.38
Plasmonic AMLs	359.76; 64.51	25.09	-18.48

Table 3.9 also lists the zeta potential results for the same structures, measured via electrophoretic light scattering technique. All samples hold a negative surface charge, with the core/shell nanoparticles displaying the highest potential in modulus, coming from the citrate anions on the gold shell surface. On the other hand, liposomes are the closest to neutrality due to the zwitterionic character of DPPC. This lipid decreases the charge density of the MF4/Au nanoparticles upon synthesis of the AMLs, resulting in composites with a charge of -18.48 mV. This potential prevents their aggregation, stabilizing the colloids through electrostatic and steric repulsion (279).

3.3 PLASMONIC MAGNETOLIPOGEL

3.3.1 Incorporation of particles into hydrogel matrix

After the synthesis and characterization of the hydrogelator and plasmonic magnetoliposomes, the structure initially proposed in this work was developed. It was prepared for a final concentration of 0.3 wt% in Nap-L-Lys(Cbz)-*Z*-ΔAbu-OH hydrogelator (compound **1**), 0.5 mM in DPPC and 0.05 wt% in nanoparticles. The last one was chosen considering some literature reports (280,281); indeed, those studies point to a decrease in healthy cells' viability for increasing concentrations of $MnFe_2O_4$/Au core/shell nanoparticles, even though the gold coating makes manganese ferrite more biocompatible. To achieve gelation, 5 mg/mL of GdL were used, which resulted in a final pH of 6. Considering that part of the MF4/Au core/shell nanoparticles were not trapped in the lumen of the lipid bilayer, we believe that the need for a larger amount of GdL for the gelation of compound **1**, regarding CGC studies described in section 3.1.2.1, is caused by the residual amount of hydroxylamine on the surface of the same nanoparticles, which makes the pH of the hydrogel precursor solution higher. **Figure 3.24** shows the visible differences in compound **1**-based hydrogel (**H**) and the derivative magnetolipogel (**MLG**).

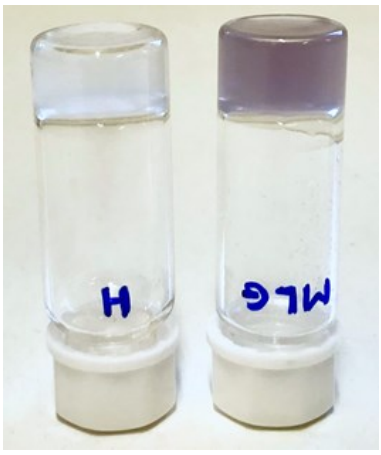

Figure 3.24 – Illustration of the formation of the hydrogel (0.3 wt% Nap-L-Lys(Cbz)-Z-ΔAbu-OH hydrogelator, 2% v/v 1 M NaOH, 0.5 wt% GdL) (left) and magnetolipogel (0.3 wt% Nap-L-Lys(Cbz)-Z-ΔAbu-OH hydrogelator, 2% v/v 1 M NaOH, 0.05 wt% MF4/Au core/shell NPs, 0.5 mM DPPC, 0.5 wt% GdL) (right).

3.3.1.1 Effect of different components in hydrogelator behaviour, local viscosity, secondary structure of hydrogel fibres and self-assembly kinetics

At this stage, we evaluated the effect of incorporating magnetoliposomes as well as their individual constituents (DPPC-based liposomes and bare core/shell magneto-plasmonic nanoparticles) into the hydrogel in order to isolate different contributions. To this end, gels without nanoparticles (**H**), with

MF4/Au nanoparticles (magnetogels, **MG**), with liposomes (lipogels, **LG**) and with magnetoliposomes (magnetolipogels, **MLG**) were developed for the same concentration of each material.

First, we followed the change in the photophysical behaviour of the intrinsic probe naphthalene in order to detect possible changes in the fibres induced by those entities, so the composites were excited at 280 nm (**figure 3.25**). All gels exhibit maximum fluorescence emission at 340 nm, related to Nap monomer state, and the aggregate-corresponding band (420 nm) is only visible for **H** and **LG**. Overall, the maximum fluorescence intensity decreases in the following order: H > LG > MG > MLG.

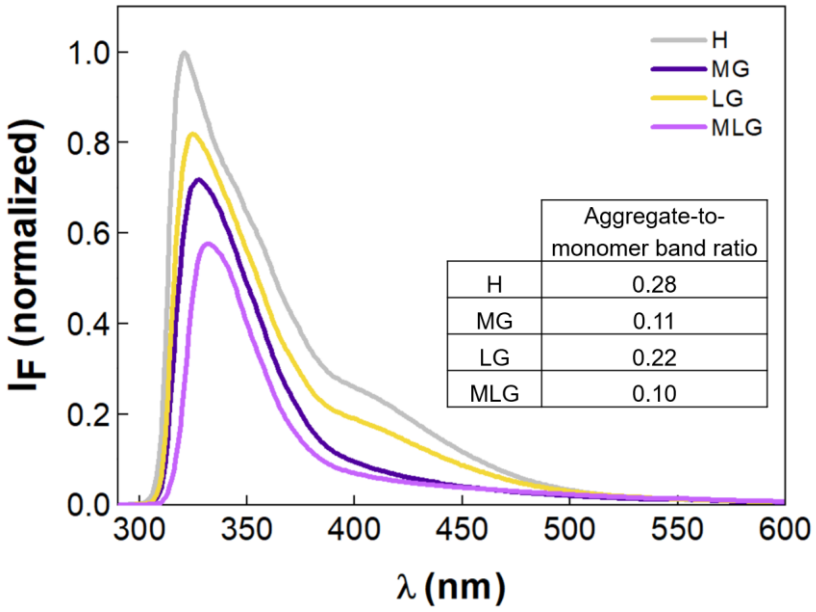

Figure 3.25 – Hydrogel (**H**), magnetogel (**MG**), lipogel (**LG**) and magnetolipogel (**MLG**) emission spectra of the hydrogelator and corresponding aggregate-to-monomer band ratios. λ_{exc}=280 nm.

In fact, one of the effects of the introduction of MF4/Au nanoparticles and plasmonic AMLs is the increase in energy loss by non-radiative processes, such as quenching; the latter can result from two phenomena: electron energy transfer to the nanoparticles due to their broad absorption spectrum and heavy atom effect, which favours intersystem crossing (282). Additionally, liposomes are closely related to light scattering, despite being the smallest effect observed. Thus, one can easily understand that the **MLG** fluoresces the least, since it is the composite gel with the highest density of additional components. The possible contribution of gold-shell localized surface plasmons should also be taken into account; indeed, plasmonic modes may inhibit fluorescence in the vicinity of the nanoparticles due to the coupling of higher order multipolar resonances (283). **Figure 3.25** also shows the aggregate-to-monomer band ratios. It is noticed that the introduction of lipids into the gel does not significantly impact that ratio contrary to

core/shell nanoparticles. Therefore, it is deduced that the latter make peptide packing more difficult, so that the low ratio calculated for the **MLG** is mainly caused by MF4/Au NPs.

The fluorescent probe Nile Red was added to the same composite gels to a final concentration of 2.5 μM in order to study fibres' microenvironment. This molecule was employed given its solvatochromic character, barely fluorescing in polar environments and exhibiting high fluorescence quantum yield in hydrophobic regions (284). **Figure 3.26 A** shows the fluorescence emission spectrum of Nile Red incorporated in the gels and **figure 3.26 B** lists the calculated anisotropy values. The wavelength of maximum emission is identical for all nanosystems, which indicates a similar polarity – between that of water and ethanol (285). Interestingly, the introduction of liposomes and AMLs into the hydrogel matrix equally reduce Nile Red fluorescence. This phenomenon results from the above-mentioned lipid light scattering (component present in the same concentration in the LG and MLG), which makes probe excitation less efficient.

A

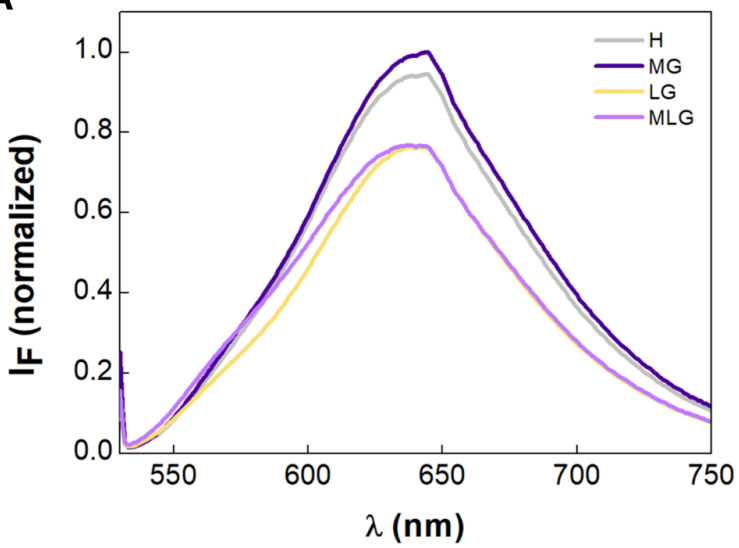

B

	Anisotropy, r
H	0.288
MG	0.296
LG	0.298
MLG	0.281

Figure 3.26 – Nile red fluorescence emission (A) and steady-state anisotropy values (B) for the hydrogel (**H**), magnetogel (**MG**), lipogel (**LG**) and magnetolipogel (**MLG**). λ_{exc}=520 nm.

The generally high anisotropy values also reveal that the microviscosity around the probe is equivalent for all four gels, further pointing to very similar interactions between probe and the surrounding environment (194). Now, if all systems have similar polarity and microviscosity, it is likely that Nile Red is settled on the surface of the fibres. These results encourage the exploration of all structures (**H**, **MG**, **LG** and **MLG**) for modulated delivery of hydrophobic and amphipathic drugs by assuming a distribution of pharmaceuticals similar to that discussed here (194).

To see whether the introduction of MF4/Au NPs, liposomes and magnetoliposomes induces important changes in the secondary structure, conformation and bonding pattern of the hydrogel fibres, Raman spectroscopy was employed. We sweeped the range 700 – 1800 cm^{-1} in order to cover amide I region (1640 – 1680 cm^{-1}), which is widely used to detect changes in the secondary structure of fibres (213). Although this mode of C=O vibration is not clearly detected in any of the spectra, possibly owing to the noisy background, we can assign some peaks, as shown in **figure 3.27**.

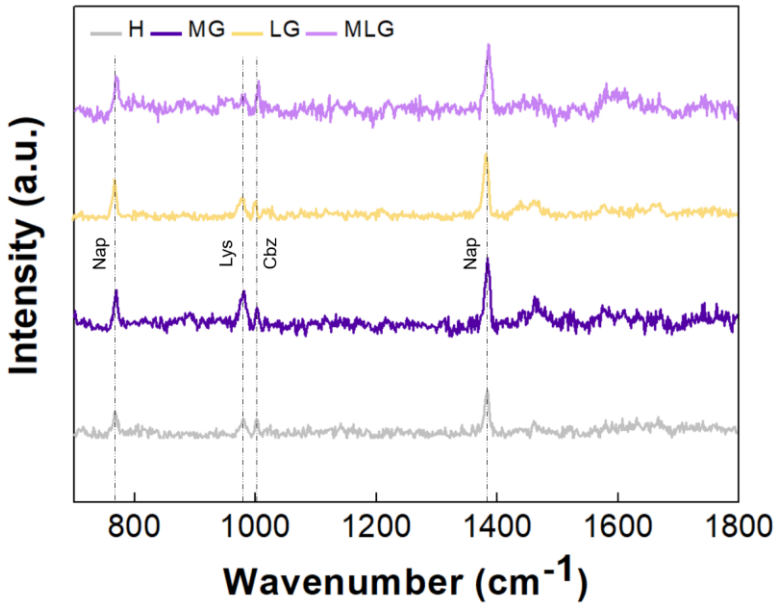

Figure 3.27 – Raman scattering spectra of the hydrogel (**H**), magnetogel (**MG**), lipogel (**LG**) and magnetolipogel (**MLG**). Vertical lines represent the reported Raman shifts of naphthalene, lysine, and benzene derivatives.

A well-defined band with medium intensity appears at 760 cm^{-1} in the region of breathing and puckering modes of naphthalene, and a strong one arises at 1384 cm^{-1}, resulting from the C=C stretching of the same functional group (286–291). The signal around 1003 cm^{-1} is characteristic of phenyl rings, whose vibration mode assignment has not yet been correctly determined (286). Finally, the weak band appearing at 981 cm^{-1} is ascribed to lysine, in a vibrational mode involving C_δ and C_ε (292–294).

Observing the **MG** spectrum, it is remarkable the increase in cross-section of the above-mentioned bands, which may arise from the lower hydration of the fibres (295), mainly at the level of naphthalene protecting group and lysine aliphatic chain. This phenomenon is attenuated when lipids are added to the hydrogel (which may be related to the polar head of DPPC (fibre-contacting moiety)) and is again present for the naphthalene-correponding bands when plasmonic AMLs are introduced. Here, all peaks shift to higher wavenumbers (blue-shift) and a weak broad band appears in the amide I region, which is associated with

hydrogelator-metal/membrane interactions (295) and changes in the peptide backbone conformation (213), respectively.

Several interesting fluorescent molecules are described as molecular rotors since they are sensitive to changes in viscosity of biopolymeric materials, i.e., their fluorescence quantum yield depends on the local viscosity (296). Thus, they have been used to follow the self-assembly process as they allow to compare the results with mechanical data obtained by rheology. Despite not being described as molecular rotor, Nile Red was once again used to probe the self-assembly process upon the introduction of core/shell nanoparticles, lipid bilayers and AMLs, using fluorescence spectroscopy. For such, after the addition of GdL to the different gel precursor solutions, the fluorescence intensity of Nile Red at a fixed wavelength (620 nm) was monitored as a function of time (**figure 3.28**).

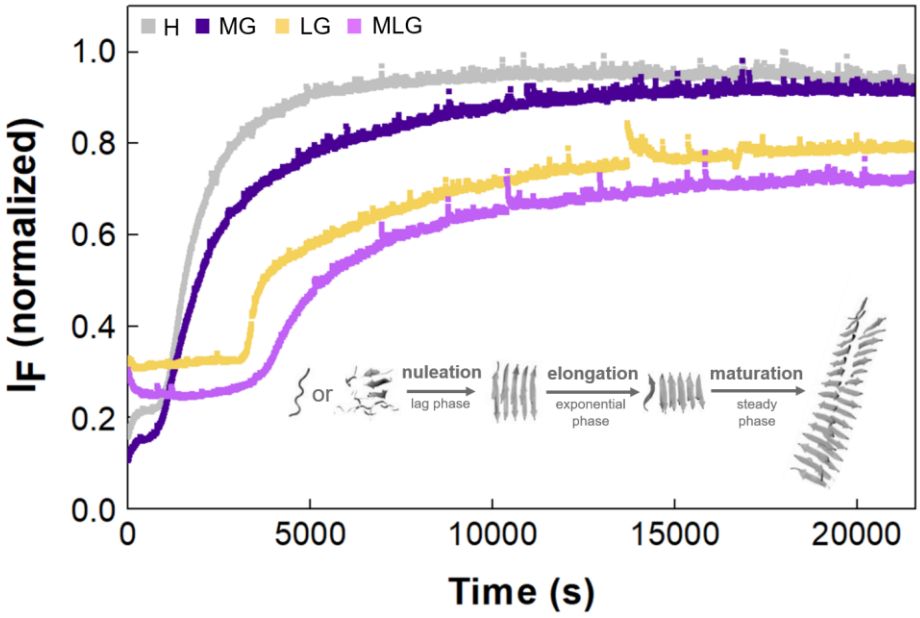

Figure 3.28 – Self-assembly kinetic profile of pristine hydrogel (**H**), magnetogel (**MG**), lipogel (**LG**) and magnetolipogel (**MLG**). λ_{exc}=520 nm, λ_{em}=620 nm.

The lower terminal fluorescence intensities for the lipogel and the magnetolipogel agree with the results presented in **figure 3.26**, where it is revealed that lipid-induced light scattering decreases Nile Red excitation, leading to a lower fluorescence emission. Apart from this, all gels demonstrate sigmoidal kinetics, where the initial lag phase corresponds to nucleation, the exponential one reflects the elongation process, and the plateau translates fibrils' maturation (213,297). Saitô's model describes the influence of certain parameters on nucleation and aggregation rates, assuming a two-step mechanism (297–299), as follows:

$$n_0 M \rightleftharpoons M_{n_0} \overset{k_n}{\rightarrow} P_n$$

$$M + P_n \overset{k_e}{\rightarrow} P_{n+1}$$

where M represents the monomer, n_0 is the micelle aggregation number, M_{n_0} correspond to the micelle (precatalytic form of the monomer), P_n is the nucleus of the fibril with n hydrogelator molecules and k_n and k_e represent the average nucleation and growth rate constants, respectively (298,299). Thus, fibril formation can be described according to:

$$f(t) = \frac{\rho\left(e^{(1+\rho)k_s t} - 1\right)}{1 + \rho e^{(1+\rho)k_s t}} \qquad (3.4)$$

in which $k_s = k_e[M]$ is the effective growth rate constant and ρ equals k_n/k_s (298,299). We fitted this equation to the experimental data, calculating the average nucleation and growth parameters, as shown in **table 3.10**.

Table 3.10 – Curve-fitting parameters obtained from the fitting of Saitô's model to the fluorescence spectroscopy profiles.

	$k_n\ (s^{-1})$	$k_e\ (M\ s^{-1})$	$k_s\ (s^{-1})$
H	1.00	388.66	2.19
MG	1.10	342.20	1.93
LG	0.20	207.26	1.17
MLG	0.04	389.06	2.20

The reader may immediately notice the similarity between the parameters calculated for the hydrogel and magnetogel and for the lipogel and magnetolipogel, which is visible for the kinetic profiles (mainly the lag phase) as well. Although the kinetic curves of **H** and **MG** are not exactly S-shaped, the adoption of Saitô's sigmoidal model allows to quantitatively compare all systems. The short exponential period (in **H** and **MG** curves) lasting up to 300 seconds points to the occurrence of a primordial phenomenon, such as the early-assembly of lower hierarchical structures (e.g., oligomers); the latter may act as homologous seeds, accelerating the nucleation process (300). It seems that the addition of the MF4/Au core/shell nanoparticles has no major impact on this step, contrarily to the elongation phase, whose speed decreases; here, the monomers take longer to join the previously formed nucleus possibly because of their adsorption to the NPs (301).

A completely different scenario is found when DPPC liposomes are added to the hydrogel. Here, the above-mentioned pre-established structures seem to be disturbed by the liposomes, slowing down the nucleation as well as the elongation rate. Indeed, the literature states that lipid bilayers, depending on

composition, size, shape, and curvature, can affect fibrillation in that a slower process may result from fibre unfolding and/or local increases in concentration (which quench or shift the fibre equilibrium toward monomer) (300).

For the addition of plasmonic AMLs, the kinetic constants are polarizing: if on the one hand the nucleation phase is the slowest, on the other hand the shortest elongation period is recorded, with a rate of 2.20 s^{-1}. Here, we have to consider the presence of a DPPC-based bilayer containing core/shell nanoparticles both in the lumen and in the outside. Apparently, hydrogelator-magnetoliposome interplay (suggested by Raman spectroscopy data) disrupts nucleus intermolecular interactions, promoting its fragmentation and, thus, inhibiting nucleation. Although smaller, these fragments provide a larger number of sites for monomer addition, which culminates in the acceleration of the exponential phase (302,303).

Overall, the results show that nucleation is the limiting-step regarding self-assembly kinetics, so the study of the individual effect of core/shell NPs, liposomes and plasmonic AMLs opens new possibilities to control and model that process. This type of experiments allows tracking small-scale phenomena, such as structural rearrangements, that are not resolved by a rheometer (296). However, Nile Red probes the hydrophobicity of the microenvironment during self-assembly and tells nothing about the mechanical properties of the final systems. Thus, the characterization of the target composite gel (magnetolipogel) was complemented with rheology.

3.3.2 Rheological properties

Time, frequency, and strain amplitude sweeps were performed in order to further understand the effect of magnetoliposomes on the rheological properties of the hydrogel. For such, the bare hydrogel and magnetolipogel were prepared as described in section 3.3.1 for a final volume of 1 mL, with the former working as reference.

3.3.2.1 Time sweep

To evaluate the gelation time, the elastic and viscous moduli were monitored for 10 h at a fixed frequency of 1 Hz by applying a strain amplitude of 0.0001% and 0.001% for the magnetolipogel and the bare hydrogel, respectively. The results are shown in **figure 3.29**.

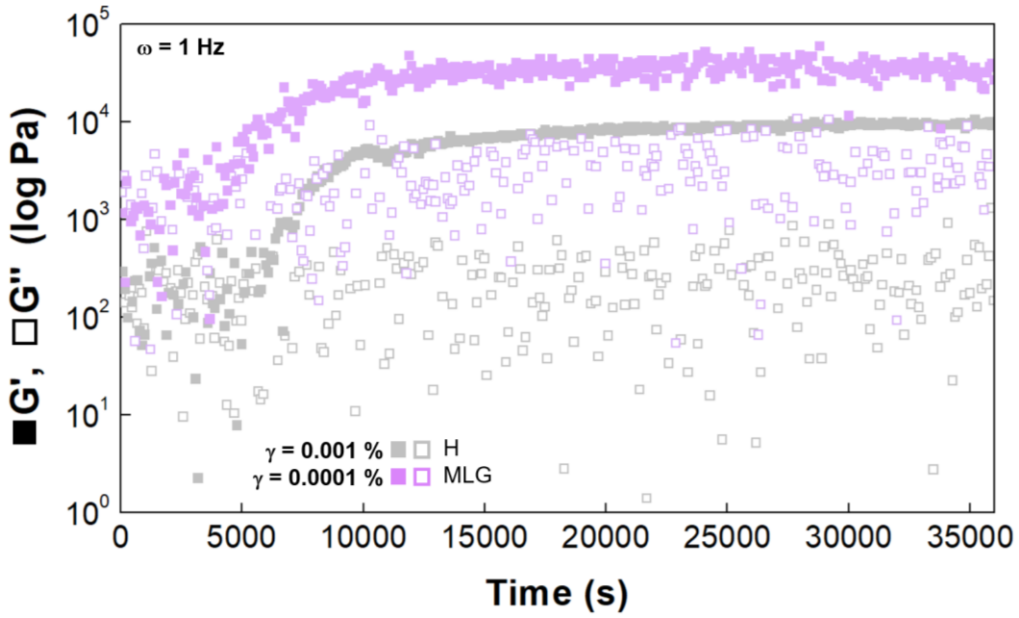

Figure 3.29 – Time dependence of elastic (solid symbols) and viscous (empty symbols) moduli for the hydrogel (**H**) and magnetolipogel (**MLG**).

The initial lag phase, quite noisy for both samples, represents the formation of lower hierarchical structures that are not quantitatively characterised by the rheometer with respect to elasticity. It lasts approximately 6600 seconds for the bare hydrogel and decreases to 4800 seconds for the magnetolipogel. Then, the exponential growth of the elastic modulus takes place and equilibrium is reached after 10200 seconds, decreasing to 9000 seconds with the addition of magnetoliposomes. At this stage, the elastic moduli of the samples are clearly higher than their respective viscous moduli, so we are definitely in the presence of self-supporting gels. For the bare hydrogel, the addition of 5 mg/mL of GdL enables faster gel setting compared with the use of only 0.4 wt% (**figure 3.10**, compound **1**-based hydrogel); this phenomenon has already been described by Veloso *et al.*, who argue that both lag and exponential phase are accelerated if more protons are available over time, assuming that GdL hydrolysis is also a kinetic process (213).

The reader may notice that gelation is further accelerated by introducing plasmonic AMLs into the gel precursor solution. To quantitatively confirm this, as for the previous "Nile red fluorescence intensity vs. time" plots, we fitted Saitô's model to the obtained kinetic curves. The resulting parameters are provided by **table 3.11**.

Table 3.11 – Curve-fitting parameters obtained from the application of Saitô's model to rheological data.

	$k_n\ (s^{-1})$	$k_e\ (M\ s^{-1})$	$k_s\ (s^{-1})$
H	0.058	120.48	0.68
MLG	0.074	143.05	0.81

Overall, these values are considerably smaller than those found in the self-assembly kinetics (except for **MLG** k_n), so it follows that Nile Red does not make up a molecular rotor. This is not surprising in that Nile Red fluorescence of the previous studies results from local hydrophobicity and has nothing to do with the bulk mechanical characteristics of the systems (296). However, as explained in section 3.3.1.1, that molecule allows probing nanoscale structural changes and locating their occurrence in the gelation timescale by comparison with rheological data.

From that, and for the bare hydrogel data (**H**), comes the following interpretation: the nucleation and elongation processes (~5000 seconds) fit in the lag phase of rheology kinetics, not contributing significantly to the increase of the solution elastic modulus. Only during fibril maturation, an exponential increase in G' occurs, prompting us to conclude that a true gel is formed only at the final stage of fibre development.

On the other hand, the nucleation and elongation periods found in **MLG** fluorescence kinetics match with the lag and exponential phases of the corresponding rheological kinetics, respectively. Thus, the presence of not fully developed assemblies has great relevance in terms of elasticity, possibly due to the occurrence of stiffer structures, such as AMLs and core/shell NPs. We believe that the latter are responsible for catalysing the transition of the self-assembled structures from a more random setup to a highly ordered arrangement through electrostatic interactions (304); hence, higher values of k_n and k_s were computed for **MLG** gelation regarding the pristine hydrogel.

3.3.2.2 Frequency sweep

To obtain gels' mechanical spectra, the oscillatory frequency was swept from 0.024 to 100 Hz, with a strain amplitude fixed at 0.01% and 0.001% for the hydrogel and the plasmonic magnetolipogel, respectively.

Besides the different gelation processes, **figure 3.30** demonstrates that the incorporation of magnetoliposomes and core/shell nanoparticles reinforces the elasticity of the gel, increasing G' by a factor of 4 (up to 45 kPa). Given the reported prevalence of rheological enhancement upon introduction

of lipid vesicles into gels' matrices (191,304–306), the present effect can be mostly attributed to the DPPC bilayer constituting the plasmonic AMLs. The interplay between that bilayer and the hydrogelator molecules by hydrophobic interactions is probable due to their competition for hydrophobic regions (307,308). Hydrogen bonds and electrostatic interactions are also possible, given the polar head of DPPC (positive charge) and the negative charge of compound **1** (at neutral-basic pH) (307,308). Therefore, AMLs hypothetically function as nucleation points, enabling a more dispersed network with larger elasticity.

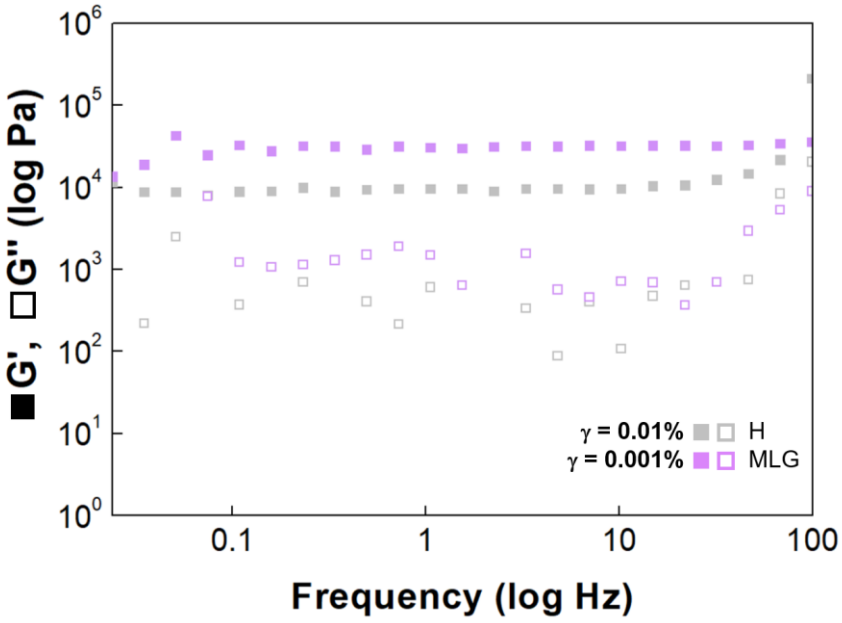

Figure 3.30 – Frequency dependence of elastic (solid symbols) and viscous (empty symbols) moduli for the hydrogel (**H**) and magnetolipogel (**MLG**).

3.3.2.3 Amplitude sweep

To evaluate the mechanical response of the magnetolipogel and the reference hydrogel to an increasing strain, successive amplitudes in the range of 0.001 to 200% were applied at a constant frequency of 1 Hz (**figure 3.31**).

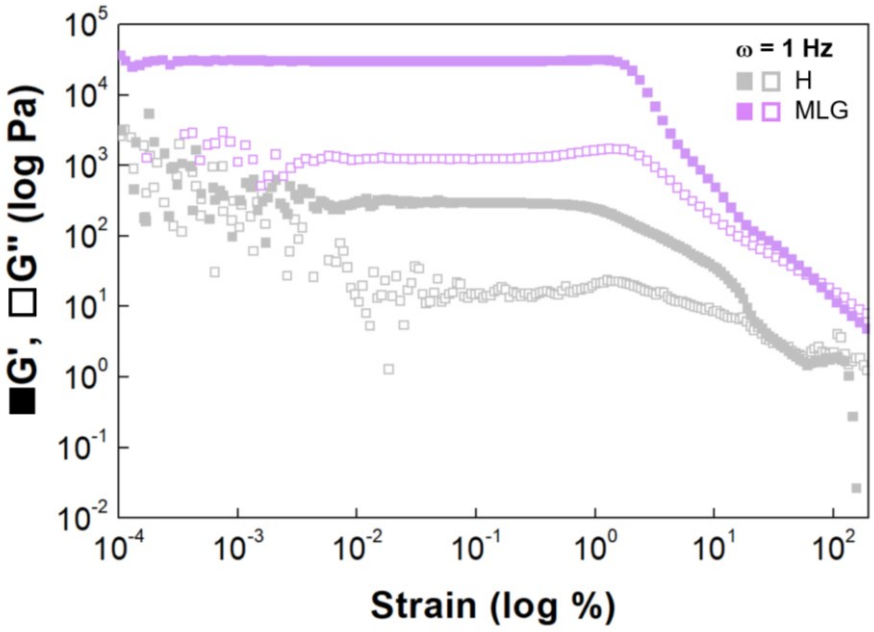

Figure 3.31 – Strain amplitude dependence of elastic (solid symbols) and viscous (empty symbols) moduli for the hydrogel (**H**) and magnetolipogel (**MLG**).

For the pristine hydrogel, SAOS takes place for amplitudes up to approximately 1%. Increasing strain intensity, this gel switches to the LAOS regime, in which both G' and G'' gradually decrease. For the magnetolipogel, LAOS starts for amplitudes exceeding 2% and proceeds under the well-known Payne effect. The latter is primarily related to the gel filler and not to the gel-forming peptide; it involves the transition of a viscous liquid to a fluid state at higher amplitudes (309), which is confirmed by the breaking strain values displayed in **table 3.12**. In this case, the main cause is likely to be structural rearrangements involving the breaking and recovery of weak interactions and/or aggregation/disaggregation of AMLs and core/shell NPs (213).

Table 3.12 – Breaking strain for the hydrogel (**H**) and magnetolipogel (**MLG**), taken at the point where G' equals G''.

	Breaking strain (%)
H	39.5
MLG	69.5

3.3.3 Microstructure

Figure 3.32 shows STEM micrographs of the **MLG** prepared according to the usual method.

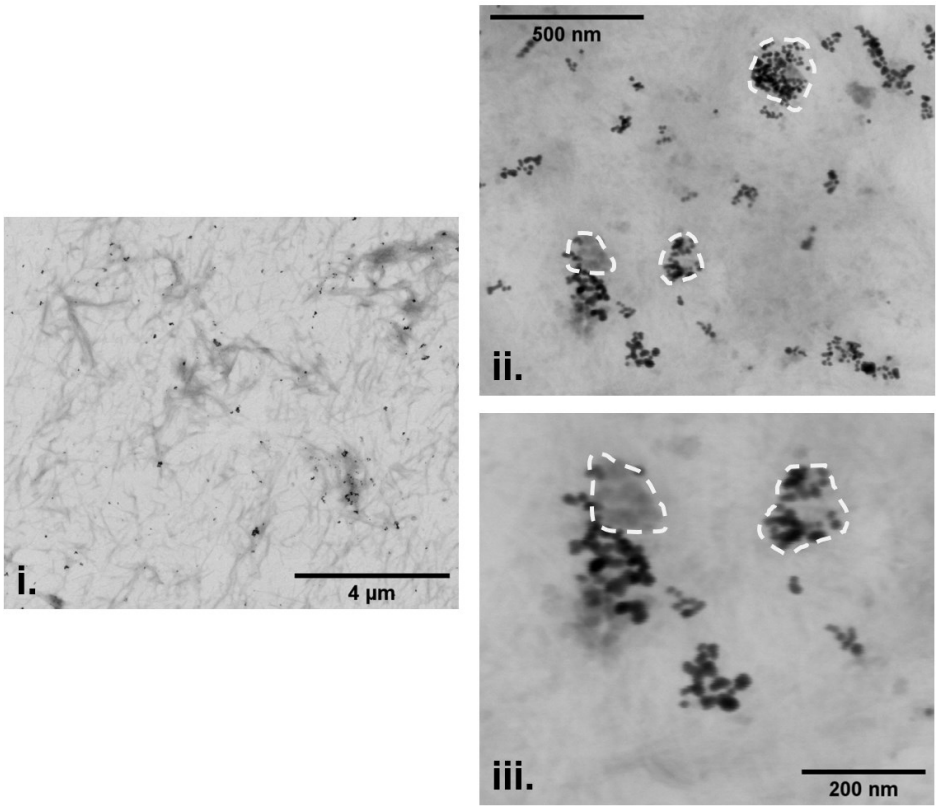

Figure 3.32 – STEM images of the magnetolipogel at different magnifications – scale bar: 4 µm (i), 500 nm (ii) and 200 nm (iii).

The incorporation of plasmonic magnetoliposomes into the hydrogel along with the use of 5 mg/mL of GdL to trigger gelation produces a network with a larger mesh size composed by shorter and thicker fibres (**figure 3.32 i**). The corresponding histogram (**figure 3.33 A**) reveals an average cross-section of 64 nm, being considerably higher than that found for the bare hydrogel with 0.4 wt% in GdL (**figures 3.8 A** and **3.9 A**).

The core/shell nanoparticles are well dispersed in the hydrogel matrix (black spots), with occasional aggregates. By zooming these areas (**figures 3.32 ii** and **3.32 iii**), MF4/Au NPs, with an average diameter near 25 nm (**figure 3.33 B**), seem to be confined by a well-defined boundary, which we believe to be a DPPC lipid bilayer (represented by the white dashed line) with, at least, 150 nm in diameter. These organic structures are best visualised by other microscopy techniques, the most commonly used being cryo-transmission electron microscopy.

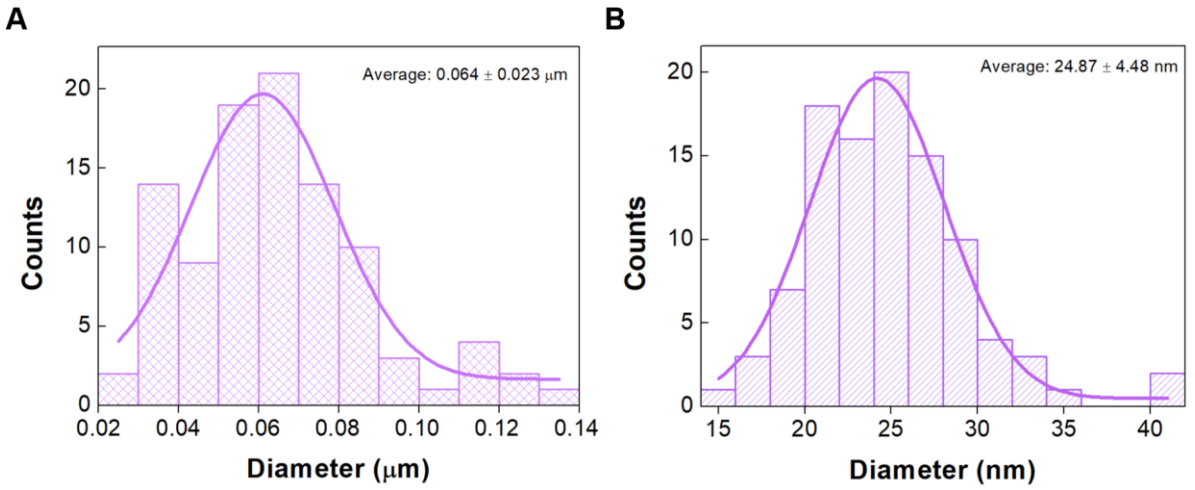

Figure 3.33 – Fibres' (A) and incorporated core/shell nanoparticles' (B) diameter distribution in the magnetolipogel. Both histograms are fitted with a Gaussian function.

Indeed, among other factors, the mesh size is a key parameter for gel swelling and the morphology studies suggest that it is influenced by the presence of core/shell nanoparticles and AMLs. Therefore, it is likely that the concentration of the latter controls the degree of swelling, which, in turn, may have a major impact on the release profile of any drug that is incorporated into the system. This topic will be addressed in detail below.

3.4 EVALUATION OF THE COMPOSITE GEL AS A PLATFORM FOR DRUG DELIVERY

Having demonstrated the successful incorporation of plasmonic magnetoliposomes into the hydrogel matrix, the next step was to perform release assays of content in response to an external trigger in order to assess the performance of the system as a controlled drug delivery platform. To this end, the pristine hydrogel (**H**) – which acted as a reference – and three different magnetolipogels (**MLG**) were prepared and loaded with the model drug 5(6)-carboxyfluorescein (CF), according to **table 3.13**.

Table 3.13 – Summary of the composition of the systems developed for controlled drug delivery and CF location regarding plasmonic AMLs. Gelation was achieved using 5 mg/mL of GdL.

		Compound 1 (wt%)	MF4/Au NPs (wt%)	DPPC (mM)	CF (μM)	CF relative location
H		0.3	0	0	10	in and out
MLG	**1**	0.3	0.05	0.5	10	in and out
	2	0.3	0.15	0.5	10	in and out
	3	0.3	0.05	0.5	6.85	inside

Compared to **MLG1**, **MLG2** has three times its content in core/shell NPs and **MLG3** has no CF in the matrix, only inside the AMLs. From the latter, a CF encapsulation efficiency of 68.5% was determined by measuring and converting fluorescence to concentration with a previously obtained calibration curve.

When the fluorescent dye CF has a high local concentration – for instance, inside magnetoliposomes – self-quenching takes place, making its fluorescence negligible. The opposite occurs when this molecule is released to the outside of the system (310,311), making it easy to convert fluorescence emission intensity into payload concentration. Furthermore, the advantage of using this dye lies in its polyanionic nature (**figure 3.34**), preventing its irreversible retention in the negatively charged hydrogel network and, thus, enabling easy evaluation of the drug release profile.

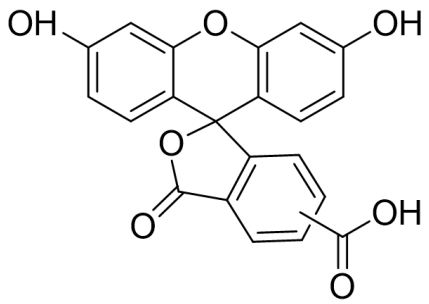

cLogP = 3.16

MW = 376.32 g/mol

λ_{ex} 495 nm; λ_{em} 517 nm in 0.01 M phosphate buffer pH 7.4

Figure 3.34 – Structure and molecular properties of the model drug 5(6)-carboxyfluorescein. cLogP calculated with *ChemDraw* software.

3.4.1 5(6)-Carboxyfluorescein microenvironment

Steady-state fluorescence anisotropy measurements were carried out to study the effect of gelation on CF local microviscosity and eventual differences in model drug location among the developed systems. **Table 3.14** lists the values obtained before and after the addition of GdL to the gel precursor solutions.

Table 3.14 – Steady-state fluorescence anisotropy (r) values of CF incorporated both in the hydrogel (**H**) and in the magnetolipogels (**MLG1**, **MLG2** and **MLG3**) before and after gelation. λ_{exc}=495 nm.

		r	
		Before gelation	**After gelation**
H		- 0.0474	0.0255
MLG	**1**	- 0.0397	0.0183
	2	- 0.0032	0.0322
	3	- 0.0200	0.0179

The lower the anisotropy, the higher the degree of rotation of the dye and therefore the lower the local microviscosity (17). Accordingly, the low anisotropy values of the gels' precursor solutions point to a highly fluid local environment, which translates into almost free rotation of the model drug (17).

After gelation, the anisotropy increases as expected and some changes in the type of interactions established by CF and the surrounding medium can be deduced, which may denote its settling in different locations. With the addition of the AMLs solution with a concentration of 0.05 wt% in core/shell NPs, r decreases, which suggests that CF is mostly located in the aqueous lumen of the plasmonic AMLs. Actually, the similarities between the **MLG1** and **MLG3** (the latter only containing CF within the AMLs) anisotropy values support that same explanation. Interestingly, anisotropy increases when we scale up the concentration of core/shell NPs to 0.15 wt% in the system (**MLG2**). Here, a higher percentage of CF may be in the gel matrix, which presents a higher microviscosity (213). This different distribution of the model drug may result from the synthesis of the respective AMLs: part of CF molecules should have been replaced by MF4/Au nanoparticles (as they are present in higher proportion regarding the AMLs of **MLG1** and **MLG3**) inside the lipid vesicle at the time of its assembly.

Although no major structural changes can be deduced, this analysis may be useful in explaining CF release profiles.

3.4.2 Drug release studies

In the last part of the work, the CF-loaded nanosystems mentioned in section 3.4 – 10 μM for **H**, **MLG1** and **MLG2** and 6.85 μM for **MLG3** – were evaluated regarding their drug delivery ability at pH=7.4, in which the pure hydrogel worked as blank and the magnetolipogels were investigated as to how the concentration of the core/shell NPs and the relative location of the payload influence their performance.

3.4.2.1 Passive release

In a first stage, we studied passive release from those nanosystems during 54 h to ascertain whether the inclusion of AMLs in the matrix influences CF release into the medium itself, i.e., in the absence of stimuli.

To quantitatively assess those effects, the mathematical Ritger-Peppas model (**equation 3.5**) was fitted to "Cumulative CF release vs. time" plots (**figure 3.35**). As discussed in section 1.2.1.1.2 of the thesis introduction, this model – in which M_t/M_∞ represents the fraction of drug released at time t – considers both erosion/swelling of the gel matrix and diffusion, and is described by the constant k and exponent n

(44,45). While the former translates the release rate, the latter defines the diffusion mechanism according to **table 3.15** (45).

$$\frac{M_t}{M_\infty} = kt^n \qquad (3.5)$$

Table 3.15 – Interpretation of diffusional release mechanisms for Ritger-Peppas model.

n	**Drug transport mechanism**
≤ 0.5	Quasi-Fickian diffusion/Case-I transport
0.5	Fickian diffusion/Case-I transport
0.5 < n < 1	Non-Fickian diffusion, anomalous transport
≥ 1	Zero order kinetics/Case-II transport

Overall, all gels exhibit an initial burst release that slows down from 10 h onwards. Such profile is similar for other Cbz *N*-capped peptide-based hydrogels previously developed in our research group (225). After 2 days and 6 h, the fraction of model drug released is less than 30% even for the blank hydrogel. This may be related to constructive interactions between carboxyfluorescein and peptide fibres of the network (e.g., by intercalation), already described elsewhere (28). Apart from this, it is evident that the composites influence drug delivery.

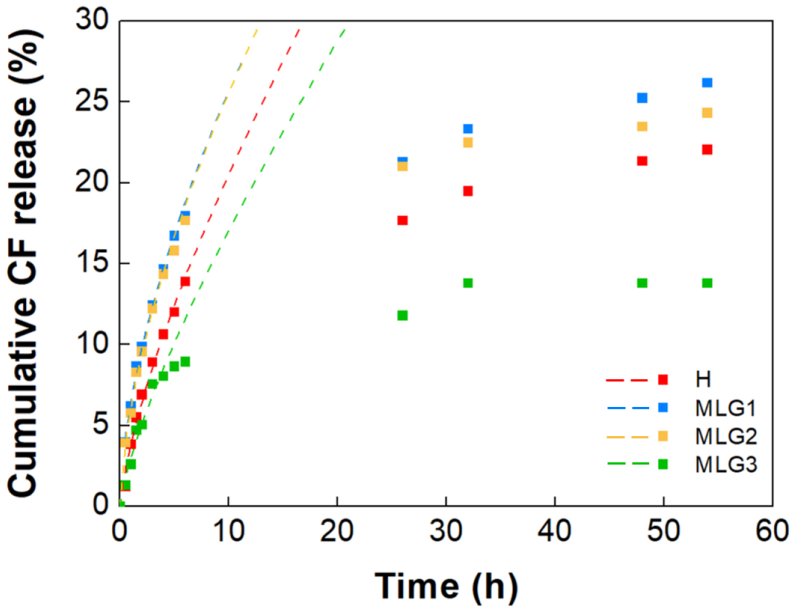

Figure 3.35 – Experimental passive CF release profiles for the gels loaded with 10 μM CF (**H**, **MLG1** and **MLG2**) and 6.85 μM (**MLG3**) (solid symbols) and Ritger-Peppas model fitting for the first 60% release data (dashed line). λ_{exc}=495 nm, λ_{em}=517 nm.

Interestingly, the introduction of AMLs and core/shell NPs and the partial encapsulation of the dye (**MLG1** and **MLG2**) enhance its release compared to the pristine hydrogel. However, this is not verified for **MLG3** (only holding CF inside the AMLs); these differences demonstrate not only the ability of the lipid bilayer to retain CF in the nanosystem, but also the increased flux of the matrix-located dye in the case of **MLG1** and **MLG2**, regarding **H**.

The kinetic model applied to the results provides valuable information to further understand these differences. Therefore, the fitting parameters for the first 60% release data (as recommended by the authors of the model (45)) were computed (**table 3.16**). The coefficients of determination reveal an excellent fit to the experimental points, which allows us to draw some conclusions. All n values are in the range 0.5 – 1, revealing a complex CF transport mechanism (non-Fickian diffusion) based on the combination between drug diffusion and matrix swelling/erosion (312).

Table 3.16 – Coefficients of determination and release parameters according to Ritger-Peppas model obtained for the CF release profiles in the pristine hydrogel (**H**) and the magnetogels (**MLG1**, **MLG2**, **MLG3**).

		R^2	n	$k\ (s^{-1})$
H		0.99	0.72	0.039
MLG	**1**	0.98	0.60	0.064
	2	0.98	0.62	0.062
	3	0.99	0.75	0.030

The hydrogel presents the second highest n, which means that swelling impacts CF release the most. In this system, the mesh size will be similar or slightly smaller than the model drug dimensions, hindering its diffusion (312,313). On the other hand, the lower n of **MLG1** and **MLG2** (closer to 0.5) indicates that the drug release is more diffusion-based. This may be related to a larger mesh size for the composite gels, as confirmed by the previous morphology studies; the smaller size of the molecule relative to those gaps makes it easier to escape from the fibre network into the medium (312,313). Obviously, **MLG3** opposes this theory, presenting the highest n value. Here, the CF migration to the medium by diffusion is less expressive since, initially, there is no dye outside the plasmonic magnetoliposomes. Only matrix swelling/erosion should promote CF flow to the fibre network and from this to the phosphate buffer layer.

3.4.2.2 Active release

In most cases, a high-frequency AMF is employed to promote hyperthermia; however, low frequencies have increasingly been used to investigate solely the field effect and leave aside the temperature

contribution (314), either for magnetic polymer matrices or magnetoliposomes (315,316). Thus, the application of such stimulus is expected to produce oscillating forces originating from the core of MF4/Au nanoparticles, by magneto-mechanical action, increasing AMLs' membrane permeability to small molecules (168). On the other hand, the shell of the same nanoparticles was used for heat production, inducing the phase transition of AMLs' lipid membrane and the rupture of the fibre network (317,318). Interestingly, although plasmonic hydrogels have proven to be very successful in cell transport, they have not shown such good results in drug delivery (318). Thus, this work further seeks to overturn the paradigm of plasmonic control of molecule release.

Considering this, CF release was tracked for 54 h in which a low frequency magnetic field (2.09 mT, 100 Hz) and light (808 nm, 1.67 W/cm^2 (laser 1); 600 nm cut-on, 0.1 mW (lamp) or 808 nm, 5 W/cm^2 (laser 2)) were separately used as dye release triggers and applied at 26 and 48 h for 30 minutes. The experiments were conducted for **MLG1**, **MLG2** and **MLG3** and **figure 3.36** displays the results.

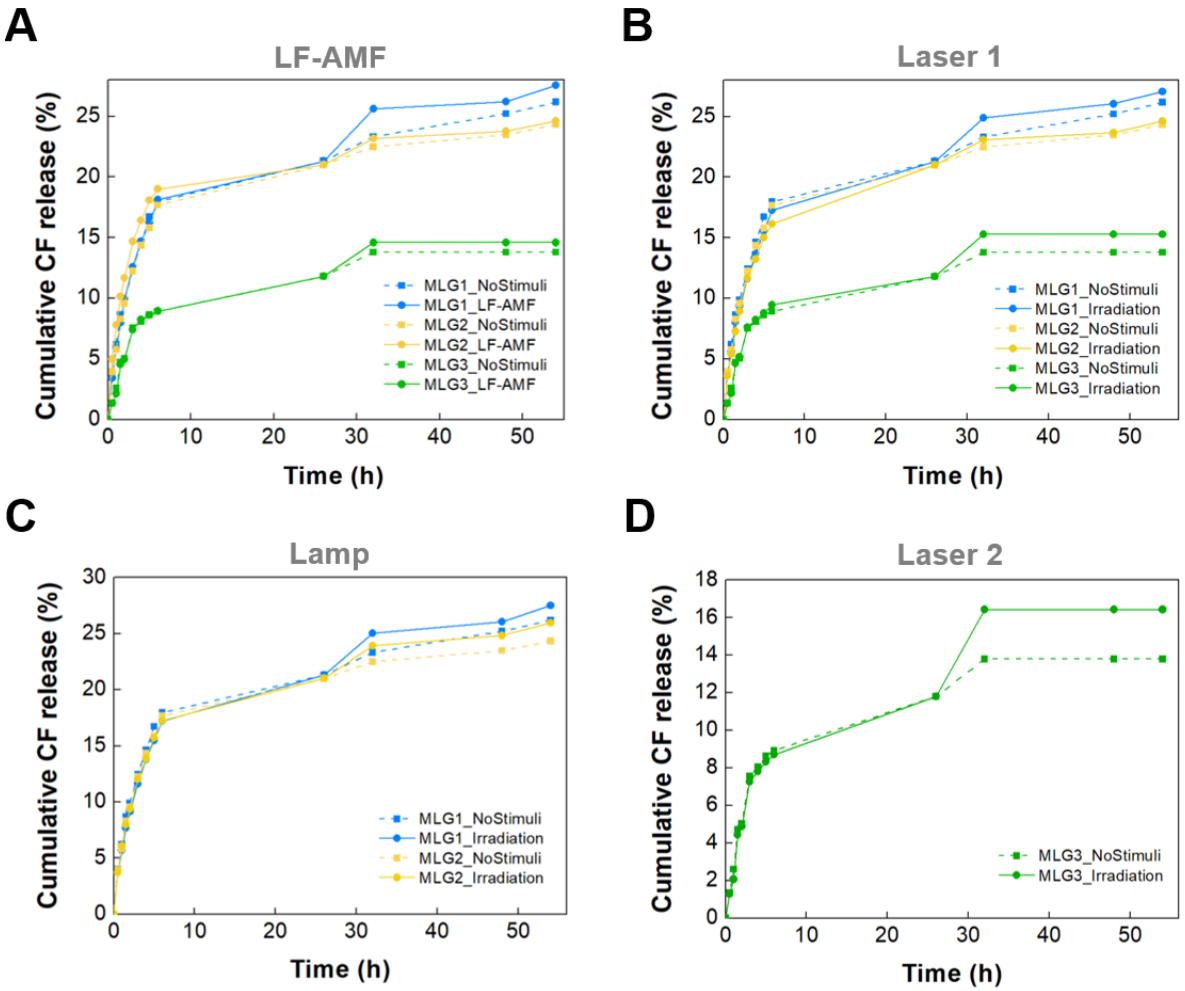

Figure 3.36 – Active CF release profiles (continuous lines) for the gels loaded with 10 μM CF (**MLG1** and **MLG2** (blue and yellow, respectively)) and 6.85 μM (**MLG3**) (green), under different triggers: low frequency-alternating magnetic field (A), 808 nm laser intensity of 1.67 W/cm^2 (B), lamp with cut-on wavelength at 600 nm (C) and 808 nm laser intensity of 5.00 W/cm^2 (D). λ_{exc}=495 nm, λ_{em}=517 nm.

The plots show that all stimuli resulted in an increased final release of the model drug for all magnetolipogels. Regarding the release profiles obtained from the application of a LF-AMF (**figure 3.36 A**), the nanosystem with the most remarkable increase in release is **MLG1**, at 26 h, being a combination of CF output from the AMLs and the matrix. Indeed, although **MLG2** has higher magnetic potential as it is more concentrated in MF4/Au NPs, these can occupy space in the matrix, clogging the pathways through which the model drug tends to evacuate the composite. Moreover, as we have seen in the previous anisotropy studies, CF is possibly more concentrated in the matrix of this magnetolipogel; thus, the negligible increase in dye release at 26 h may also be related to its self-quenching effect. These phenomena should also occur when **MLG2** is exposed to laser light (**figure 3.36 B**), revealing that the optimal concentration of core/shell nanoparticles and drug in the scaffold must rely on a compromise between its magnetoplasmonic performance and the desirable arrangement of the individual components. Meanwhile, in the case of **MLG3**, the smaller increase in CF release at 26 h compared to that of **MLG1** may result from a greater impact of the NPs' magneto-mechanical oscillation on the peptide fibres than on the DPPC membrane.

The picture changes for **MLG3** when we apply NIR radiation with a power density of 1.67 W/cm^2 (**figure 3.36 B**). Here, the enhancement of the release rate after the first stimulation cycle is quite similar to that of **MLG1** (~ 4%). The photothermal effect of MF4/Au NPs' gold shell might induce relevant structural changes in AMLs' membrane, enabling CF flow from the lumen to the matrix. Now, the latter should also undergo some degradation considering the comparable profiles of those composite gels.

When the 600 nm cut-on wavelength lamp was experimented for **MLG1** and **MLG2** (**figure 3.36 C**), an analogous triggered release was detected for both gels. In this instance, the incident wavelength range included the region of the spectrum in which the core/shell NPs have a larger absorption cross section. Thus, the eventual larger plasmonic heating caused by the higher concentration of those NPs in **MLG2** will have counterbalanced the inhibition of CF release seen earlier.

Finally, instead of subjecting **MLG3** to the lamp, we applied an 808 nm laser with a higher power density (5.00 W/cm^2) (**figure 3.36 D**). Remarkably, the greatest increase in triggered release among all assays was observed, which suggests the occurrence of extensive structural changes both in AMLs' and in the gel matrix resulting from the significant temperature increase (as supported by the optical hyperthermia studies for the MF4/Au nanoparticles). This allows to obtain an enhanced drug release control or with shorter irradiation time.

Figure 3.37 shows the change in CF release after the first (26 – 32 h) and the second (48 – 54 h) stimulation cycles, according to the trigger. Despite the double stimulation, the reader will have noticed that, in general, the second cycle had no effect. This was expected considering the morphological change visible in the gels between 26 and 32 h. The same figure allows us to select the best plasmonic magnetolipogel according to the desired stimulus. For the low frequency AMF and 600 nm cut-on wavelength radiation, **MLG1** is clearly the most promising platform. On the other hand, for the 808 nm laser with a power density of 1.67 W/cm^2, the percentage of encapsulated dye (68.5 and 100% for **MLG1** and **MLG3**, respectively) is not preponderant in enhancing drug release. In the future, we will test the lamp as a stimulus for **MLG3** and laser 2 for **MLG2** and **MLG1**.

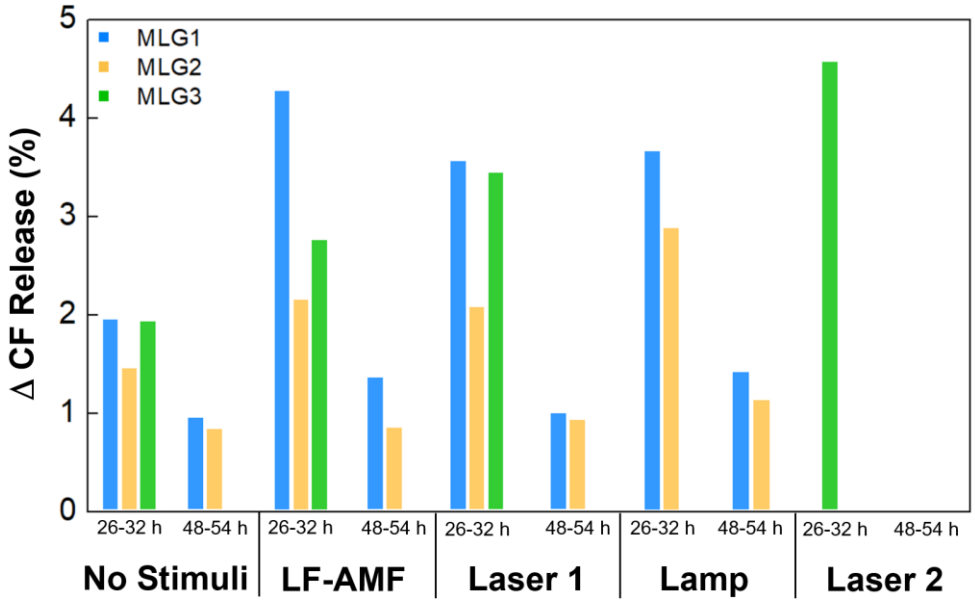

Figure 3.37 – Percentage of CF released in the time ranges 26 – 32 h and 48 – 54 h for the gels loaded with 10 μM CF (**MLG1** and **MLG2** (blue and yellow, respectively)) and 6.85 μM (**MLG3**) (green), without stimulation and under different triggers (low frequency-alternating magnetic field, 808 nm laser intensity of 1.67 W/cm^2, lamp with cut-on wavelength at 600 nm, and 808 nm laser intensity of 5.00 W/cm^2.

In short, the developed nanosystems show great potential for controlled drug delivery, as they can be optimised in several aspects. So far, we highlight three key points: (i) the possibility of modelling passive release by changing the percentage of encapsulated drug, (ii) the fact that the enhancement in triggered drug release does not require an increase in core/shell NPs concentration, and (iii) the possibility of controlling drug release through magneto-mechanical oscillation and photothermia.

3.4.2.3 Hydrogelator release

As stated earlier, we believe that the dramatic changes in the appearance of the magnetolipogels after the first cycle of stimulation (**figure 3.38**) are responsible for the ineffectiveness of the second cycle in inducing CF release.

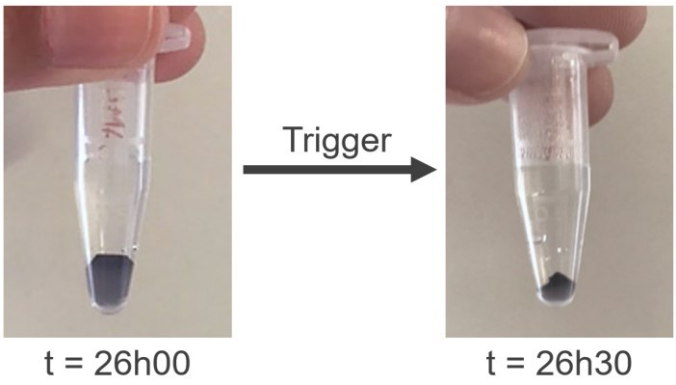

Figure 3.38 – Aspect of plasmonic magnetolipogel before and after the first stimulation cycle.

To ascertain whether those volume losses correspond to gel shrinkage or fibre network degradation, we followed hydrogelator passive release from the pristine hydrogel and active release from the **MLG1,** which was irradiated with laser 1 at 26 and 48 h (magnetolipogel and trigger selected as models). The results are plotted in **figure 3.39**.

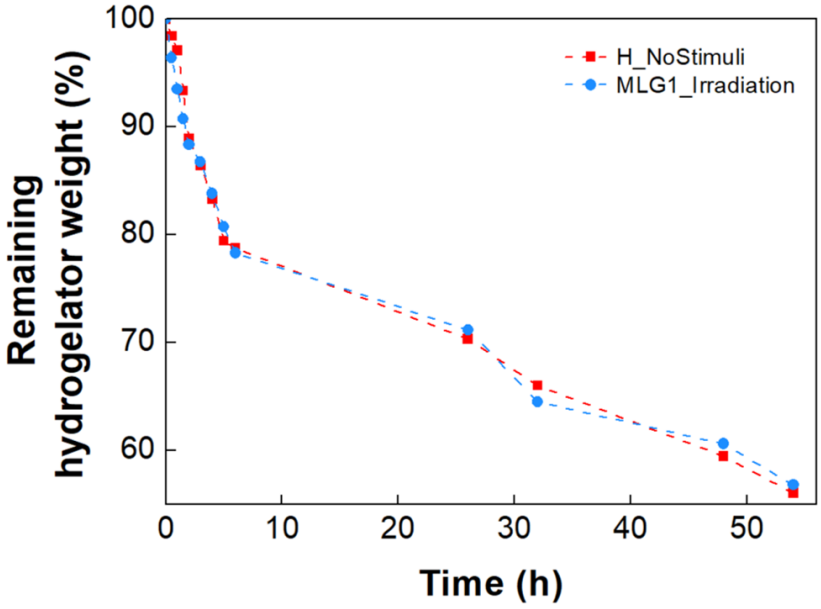

Figure 3.39 – Fraction of hydrogelator (Nap-L-Lys(Cbz)-Z-ΔAbu-OH) remaining in the hydrogel (**H**) (without stimulation) and in the magnetolipogel loaded with 0.05 wt% core/shell NPs (**MLG1**) (irradiated with an 808 nm laser intensity of 1.67 W/cm^2 at 26 and 48 h for 30 minutes). λ_{exc}=280 nm, λ_{em}=340 nm.

It should be noted that, after 54 h, both gels lose almost 50% of the hydrogelator used in their formulation (0.3 wt%) to pH 7.4 buffer, with no equilibrium being reached in the timeframe studied. This suggests the occurrence of erosion/degradation of peptide fibres; however, such phenomenon does not seem to directly influence CF release, since **figure 3.36** show its slowdown from 32 h onwards.

Aside from this, the profiles suggest that neither the presence of AMLs and core/shell MF4/Au NPs nor the action of external stimulus severely affect the network weight reduction. Therefore, the striking volume decrease in the magnetolipogel after 30 minutes of irradiation is probably related to water loss (shrinkage); this might induce some error in the calculations of released CF after the first stimulation cycle due to the dilution effect on the buffer-dissolved model drug. While the fundamental cause of shrinkage in the developed composite gels is still to be investigated, similar phenomena have already been attributed to temperature-induced helix inversion (319). Considering that this phenomenon was observed either with light irradiation or with the application of a LF-AMF, these materials are also interesting for the development of actuators sensitive to temperature and magnetic/mechanical signals (320).

Chapter 4

CONCLUSIONS AND PROSPECTS

4.1 CONCLUSIONS

In this work, we have developed, characterised, and explored a highly complex system with great potential in cancer therapy.

Considering the versatile administration and the advantages of hydrogels' porous structure in encapsulating and modelling drug release, we started by synthesising two hydrogel-forming naphthalene *N*-capped dehydrodipeptides, diverging in the *C*-terminus dehydroamino acid. Although no significant differences were recorded in the rheological properties of the resulting hydrogels, CAC studies revealed that Nap-L-Lys(Cbz)-*Z*-ΔPhe-OH forms aggregates at a much lower concentration than Nap-L-Lys(Cbz)-*Z*-ΔAbu-OH at pH=6, reflecting its extreme hydrophobicity. Magnetoplasmonic nanoparticles with 25 nm size were further developed by growing a blackberry-like gold layer on the surface of manganese ferrite nanoparticles, using the hydroxylamine methodology. The latter endowed the particles with a broad plasmonic band in the visible-NIR region, which, together with the reasonable M_s and SLP values of the core, makes them promising for hyperthermia and magnetic guidance. Coating the particles with a lipid bilayer afforded plasmonic AMLs with negative surface charge, which ensured their good stability in water.

The magnetolipogel was developed to a concentration of 0.05 wt% in core/shell NPs, 0.5 mM in DPPC and 0.3 wt% in the selected hydrogelator (Nap-L-Lys(Cbz)-*Z*-ΔAbu-OH). Its self-assembly process is characterized by a faster fibre elongation, probably impacting the final network. In fact, the introduction of AMLs into the hydrogel matrix enhanced the elastic modulus by a factor of 4, producing a network with shorter and thicker fibres.

By using 5(6)-carboxyfluorescein as a model drug, the effect of the percentage of encapsulated dye and core/shell NPs concentration on the passive and active dye release from the magnetolipogel was studied. Encapsulation of the model drug by a lipid bilayer was found to delay its release, promoting sustained drug delivery. This behaviour changed to a burst release when 5 W/cm^2 NIR radiation was applied, suggesting the occurrence of photothermally-induced structural modifications in both lipids and fibres. On the other hand, increasing the concentration of core/shell NPs did not add any advantage to the control of dye release under the tested conditions.

Considering all this, the structural and functional properties of the developed system hold great promise in changing the paradigm of cancer therapy, enabling several modalities, such as, magnetic guidance, hyperthermia, and controlled drug delivery.

4.2 PROSPECTS

Despite the promising results, to be able to consider transposing the developed system into clinical practice, it is imperative to study it thoroughly from several perspectives. First, and considering the dynamic interaction of the different materials included in the magnetolipogel, it is necessary to investigate the effect of the particles on the gel swelling/shrinking capacity, the influence of the magnetic field-induced rearrangement of core/shell nanoparticles and AMLs on the elasticity of the fibre network, and the impact of the matrix on the heating efficiency of NPs by magnetic hyperthermia and photothermia. Furthermore, biological tests will be carried out in order to evaluate the cytotoxicity of the composite gel on different cell lines, as well as the effect of active and passive drug release on the viability of tumour cells.

Depending on future results, optimisations can be made with regard to the magnetic and plasmonic properties of the core/shell nanoparticles – including the development of anisotropic particles or with different composition – and to the particle and hydrogelator content in the composite.

Finally, Nap-L-Lys(Cbz)-*Z*-ΔPhe-OH dehydrodipeptide will be tested as the hydrogelator element of the magnetolipogel and studied as to the advantages of its combination with Nap-L-Lys(Cbz)-*Z*-ΔAbu-OH.

In fact, this work is just the beginning since, despite the potential applicability of these systems, there is an urgent need to understand them from a fundamental point of view to overcome the challenges that hinder their practical implementation. These problems are mainly related to the need for extensive *in vivo* testing, determination of the number of particles per cell required to destroy certain tumours, identification of formulations that maximise the heating efficiency and minimise the number of nanoparticles and the development of predictive models that allow the rational design of new magnetolipogels.

Chapter 5

REFERENCES

5.1 REFERENCES

(1) Desai P, Thumma NJ, Wagh PR, Zhan S, Ann D, Wang J, et al. Cancer Chemoprevention Using Nanotechnology-Based Approaches. *Front Pharmacol*. 2020;11:323.

(2) Gmeiner WH, Ghosh S. Nanotechnology for cancer treatment. *Physiol Behav*. 2015;3(111):111–22.

(3) Singh R. Nanotechnology based therapeutic application in cancer diagnosis and therapy. *3 Biotech*. 2019;9(11):415.

(4) Airley R. Cancer Chemotherapy: Basic Science to the Clinic. 1st ed. *ChemMedChem*. Oxford: Wiley-Blackwell; 2009.

(5) Liu X, Zhang Y, Wang Y, Zhu W, Li G, Ma X, et al. Comprehensive understanding of magnetic hyperthermia for improving antitumor therapeutic efficacy. *Theranostics*. 2020;10(8):3793–815.

(6) Joo WD, Visintin I, Mor G. Targeted cancer therapy – Are the days of systemic chemotherapy numbered? *Physiol Behav*. 2013;76(4):308–14.

(7) Baudino TA. Targeted Cancer Therapy: The Next Generation of Cancer Treatment. *Curr Drug Discov Technol*. 2015;12(1):3–20.

(8) Yan L, Rosen N, Arteaga C. Targeted cancer therapies. *Chin J Cancer*. 2011;30(1):1–4.

(9) Sindhu S, Murugan S. Challenges and opportunities in repurposing of drugs: Mini review. *Bangladesh J Med Sci*. 2020;19(3):365–71.

(10) Adir O, Poley M, Chen G, Froim S, Krinsky N, Shklover J, et al. Integrating Artificial Intelligence and Nanotechnology for Precision Cancer Medicine. *Adv Mater*. 2019;32(13):1901989.

(11) Mura S, Nicolas J, Couvreur P. Stimuli-responsive nanocarriers for drug delivery. *Nat Mater*. 2013;12(11):991–1003.

(12) Li Y, Wang F, Cui H. Peptide-based supramolecular hydrogels for delivery of biologics. *Bioeng Transl Med*. 2016;1(3):306–22.

(13) Seow WY, Hauser CAE. Short to ultrashort peptide hydrogels for biomedical uses. *Mater Today*. 2014;17(8):381–8.

(14) Kopeček J, Yang J. Peptide-directed self-assembly of hydrogels. *Acta Biomater*. 2009;5(3):805–16.

(15) Jonker AM, Löwik DWPM, Van Hest JCM. Peptide- and protein-based hydrogels. *Chem Mater*. 2012;24(5):759–73.

(16) Coviello T, Matricardi P, Marianecci C, Alhaique F. Polysaccharide hydrogels for modified release formulations. *J Control Release*. 2007;119(1):5–24.

(17) Veloso SRS, Magalhães CAB, Rodrigues ARO, Vilaça H, Queiroz MJRP, Martins JA, et al. Novel dehydropeptide-based magnetogels containing manganese ferrite nanoparticles as antitumor drug nanocarriers. *Phys Chem Chem Phys*. 2019;21(20):10377–90.

(18) Du X, Zhou J, Shi J, Xu B. Supramolecular Hydrogelators and Hydrogels: From Soft Matter to Molecular Biomaterials. *Chem Rev*. 2015;115(15):13165–307.

(19) Thota CK, Yadav N, Chauhan VS. A novel highly stable and injectable hydrogel based on a conformationally restricted ultrashort peptide. *Sci Rep*. 2016;6(1):31167.

(20) Vilaça H, Hortelão ACL, Castanheira EMS, Queiroz MJRP, Hilliou L, Hamley IW, et al. Dehydrodipeptide Hydrogelators Containing Naproxen *N*-Capped Tryptophan: Self-Assembly, Hydrogel Characterization, and Evaluation as Potential Drug Nanocarriers. *Biomacromolecules*. 2015;16(11):3562–73.

(21) Vilaça H, Castro T, Costa FMG, Melle-Franco M, Hilliou L, Hamley IW, et al. Self-assembled RGD dehydropeptide hydrogels for drug delivery applications. *J Mater Chem B*. 2017;5(43):8607–17.

(22) He S, Mei L, Wu C, Tao M, Zhai Z, Xu K, et al. In situ hydrogelation of bicalutamide-peptide conjugates at prostate tissue for smart drug release based on pH and enzymatic activity. *Nanoscale*. 2019;(11):5030–7.

(23) Braun GA, Ary BE, Dear AJ, Rohn MCH, Payson AM, Lee DSM, et al. On the Mechanism of Self-Assembly by a Hydrogel-Forming Peptide. *Biomacromolecules*. 2020;21(12):4781–94.

(24) Pandya MJ, Spooner GM, Sunde M, Thorpe JR, Rodger A, Woolfson DN. Sticky-end assembly of a designed peptide fiber provides insight into protein fibrillogenesis. *Biochemistry*. 2000;39(30):8728–34.

(25) Aggeli A, Nyrkova IA, Bell M, Harding R, Carrick L, McLeish TCB, et al. Hierarchical self-assembly of chiral rod-like molecules as a model for peptide β-sheet tapes, ribbons, fibrils, and fibers. *Proc Natl Acad Sci U S A*. 2001;98(21):11857–62.

(26) Li J, Mooney DJ. Designing hydrogels for controlled drug delivery. *Nat Rev Mater*. 2016;1(12):16071.

(27) Fan Q, Ji Y, Wang J, Wu L, Li W, Chen R, et al. Self-assembly behaviours of peptide–drug conjugates: Influence of multiple factors on aggregate morphology and potential self-assembly mechanism. *R Soc Open Sci*. 2018;5(4):172040.

(28) Pandit G, Roy K, Agarwal U, Chatterjee S. Self-Assembly Mechanism of a Peptide-Based Drug Delivery Vehicle. *ACS Omega*. 2018;3(3):3143–55.

(29) Gupta S, Singh I, Sharma AK, Kumar P. Ultrashort Peptide Self-Assembly: Front-Runners to Transport Drug and Gene Cargos. *Front Bioeng Biotechnol*. 2020;8:504.

(30) Cote Y, Fu IW, Dobson ET, Goldberger JE, Nguyen HD, Shen JK. Mechanism of the pH-controlled self-assembly of nanofibers from peptide amphiphiles. *J Phys Chem C*. 2014;118(29):16272–8.

(31) Swietach P, Vaughan-Jones RD, Harris AL, Hulikova A. The chemistry, physiology and pathology of pH in cancer. *Philos Trans R Soc B Biol Sci*. 2014;369(1638):20130099.

(32) Ghosh G, Barman R, Sarkar J, Ghosh S. pH-Responsive Biocompatible Supramolecular Peptide Hydrogel. *J Phys Chem B*. 2019;123(27):5909–15.

(33) Raza F, Zhu Y, Chen L, You X, Zhang J, Khan A, et al. Paclitaxel-loaded pH responsive hydrogel based on self-assembled peptides for tumor targeting. *Biomater Sci*. 2019;7(5):2023–36.

(34) Raza F, Zafar H, Raza F, Khan A, Ge L, You X, et al. Cancer nanomedicine: focus on recent developments and self-assembled peptide nanocarriers. *J Mater Chem B*. 2019;7(48):7639–55.

(35) Wang Y, Zhang W, Gong C, Liu B, Li Y, Wang L, et al. Recent advances in the fabrication, functionalization, and bioapplications of peptide hydrogels. *Soft Matter*. 2020;16(44):10029–45.

(36) Xian S, Webber MJ. Temperature-responsive supramolecular hydrogels. *J Mater Chem B*. 2020;8(40):9197–211.

(37) Traverso N, Ricciarelli R, Nitti M, Marengo B, Furfaro AL, Pronzato MA, et al. Role of glutathione in cancer progression and chemoresistance. *Oxid Med Cell Longev*. 2013;2013:972913.

(38) Cao M, Wang Y, Hu X, Gong H, Li R, Cox H, et al. Reversible Thermoresponsive Peptide-PNIPAM Hydrogels for Controlled Drug Delivery. *Biomacromolecules*. 2019;20(9):3601–10.

(39) Chatterjee S, Chi-leung Hui P. Stimuli-Responsive Hydrogels: An Interdisciplinary Overview. In: Popa L, editor. *Hydrogels - Smart Materials for Biomedical Applications*. 1st ed. IntechOpen; 2019.

(40) Fu Y, Kao WJ. Drug release kinetics and transport mechanisms of non-degradable and degradable polymeric delivery systems. *Expert Opin Drug Deliv*. 2010;7(4):429–44.

(41) Mircioiu C, Voicu V, Anuta V, Tudose A, Celia C, Paolino D, et al. Mathematical modeling of release kinetics from supramolecular drug delivery systems. *Pharmaceutics*. 2019;11(3):140.

(42) Brandl F, Kastner F, Gschwind RM, Blunk T, Teßmar J, Göpferich A. Hydrogel-based drug delivery systems: Comparison of drug diffusivity and release kinetics. *J Control Release*. 2010;142(2):221–8.

(43) Ritger PL, Peppas NA. A simple equation for description of solute release I. Fickian and non-Fickian release from non-swellable devices in the form of slabs, spheres, cylinders or discs. *J Control Release*. 1987;5(1):23–36.

(44) Ritger PL, Peppas NA. A simple equation for description of solute release II. Fickian and anomalous release from swellable devices. *J Control Release*. 1987;5(1):37–42.

(45) Liu S, Chen X, Zhang Q, Wu W, Xin J, Li J. Multifunctional hydrogels based on β-cyclodextrin with both biomineralization and anti-inflammatory properties. *Carbohydr Polym*. 2014;102(1):869–76.

(46) Sis MJ, Webber MJ. Drug Delivery with Designed Peptide Assemblies. *Trends Pharmacol Sci*. 2019;40(10):747–62.

(47) Lin CC, Metters AT. Hydrogels in controlled release formulations: Network design and mathematical modeling. *Adv Drug Deliv Rev*. 2006;58(12–13):1379–408.

(48) Ghannam M, Abu-Jdayil B, Esmail N. Flow behaviours comparison of crude oil–polymer emulsions. *Int J Ambient Energy*. 2018;39(6):581–93.

(49) Chakroun RW, Wang F, Lin R, Wang Y, Su H, Pompa D, et al. Fine-Tuning the Linear Release Rate of Paclitaxel-Bearing Supramolecular Filament Hydrogels through Molecular Engineering. *ACS Nano*. 2019;13(7):7780–90.

(50) Huang X, Brazel CS. On the importance and mechanisms of burst release in matrix-controlled drug delivery systems. *J Control Release*. 2001;73(2–3):121–36.

(51) Heuser T, Weyandt E, Walther A. Biocatalytic Feedback-Driven Temporal Programming of Self-Regulating Peptide Hydrogels. *Angew Chemie - Int Ed*. 2015;54(45):13258–62.

(52) Choe R, Il Yun S. Fmoc-diphenylalanine-based hydrogels as a potential carrier for drug delivery. *E-Polymers*. 2020;20(1):458–68.

(53) Anthony Hey. *Feynman And Computation*. 1st ed. CRC Press; 2002.

(54) Khan I, Saeed K, Khan I. Nanoparticles: Properties, applications and toxicities. *Arab J Chem*. 2019;12(7):908–31.

(55) Vert M, Doi Y, Hellwich K-H, Hess M, Hodge P, Kubisa P, et al. Terminology for biorelated polymers and applications. *Pure Appl Chem*. 2012;84(2):377–410.

(56) Ojo OA, Olayide II, Akalabu MC, Ajiboye BO, Ojo AB, Oyinloye BE, et al. Nanoparticles and their biomedical applications. *Biointerface Res Appl Chem*. 2021;11(1):8431–45.

(57) Cartaxo A. Nanoparticles types and properties – understanding these promising devices in the biomedical area. *Int J Nanomedicine*. 2018;1–8.

(58) Rawat RS. Dense Plasma Focus – From Alternative Fusion Source to Versatile High Energy Density Plasma Source for Plasma Nanotechnology. *J Phys Conf Ser*. 2015;591:012021.

(59) Pelaz B, Jaber S, De Aberasturi DJ, Wulf V, Aida T, De La Fuente JM, et al. The state of nanoparticle-based nanoscience and biotechnology: Progress, promises, and challenges. *ACS Nano*. 2012;6(10):8468–83.

(60) Gatoo MA, Naseem S, Arfat MY, Mahmood Dar A, Qasim K, Zubair S. Physicochemical properties of nanomaterials: Implication in associated toxic manifestations. *Biomed Res Int*. 2014;2014:498420.

(61) Pomogailo AD, Kestelman VN. Physical methods of incorporating nanoparticles into polymers. In: *Metallopolymer Nanocomposites*. 1st ed. Berlin, Heidelberg: Springer; 2005. p. 117–34.

(62) Knobel M, Nunes WC, Socolovsky LM, De Biasi E, Vargas JM, Denardin JC. Superparamagnetism and other magnetic features in granular materials: A review on ideal and real systems. *J Nanosci Nanotechnol*. 2008;8(6):2836–57.

(63) Ahmad R, Ali Z, Mou X, Wang J, Yi H, He N. Recent advances in magnetic nanoparticle design for cancer therapy. *J Nanosci Nanotechnol*. 2016;16(9):9393–403.

(64) Xiao Y, Du J. Superparamagnetic nanoparticles for biomedical applications. *J Mater Chem B*. 2020;8(3):354–67.

(65) Yang C, Hou YL, Gao S. Nanomagnetism: Principles, nanostructures, and biomedical applications. *Chinese Phys B*. 2014;23(5):057505.

(66) Kolhatkar AG, Jamison AC, Litvinov D, Willson RC, Lee TR. Tuning the magnetic properties of nanoparticles. *Int J Mol Sci*. 2013;14(8):15977–6009.

(67) Shahri MM. Magnetic materials and magnetic nanocomposites for biomedical application. In: Henry DJ, editor. *Harnessing Nanoscale Surface Interactions: Contemporary Synthesis, Applications and Theory*. 1st ed. Elsevier Inc.; 2019. p. 77–95.

(68) Kong LB, Liu L, Yang Z, Li S, Zhang T, Wang C. Theory of ferrimagnetism and ferrimagnetic metal oxides. In: Stojanovic BD, editor. *Magnetic, Ferroelectric, and Multiferroic Metal Oxides*. Elsevier Inc.; 2018. p. 287–311.

(69) Sundaresan A, Rao CNR. Ferromagnetism as a universal feature of inorganic nanoparticles. *Nano Today*. 2009;4(1):96–106.

(70) Kružík M, Prohl A. Recent developments in the modeling, analysis, and numerics of ferromagnetism. *SIAM Rev*. 2006;48(3):439–83.

(71) Bertotti G. *Hysteresis in Magnetism: For Physicists, Materials Scientists, and Engineers*. 1st ed. Press A, editor. Elsevier Science; 1998. 129–254 p.

(72) Rajan A, Sahu NK. Review on magnetic nanoparticle-mediated hyperthermia for cancer therapy. *J Nanoparticle Res*. 2020;22(11):319.

(73) Pai AB. Iron Oxide Nanoparticle Formulations for Supplementation. In: Carver PL, editor. *Essential Metals in Medicine: Therapeutic Use and Toxicity of Metal Ions in the Clinic*. Berlin, Boston: De Gruyter; 2019. p. 157–80.

(74) Rodrigues ARO, Ramos JMF, Gomes IT, Almeida BG, Araújo JP, Queiroz MJRP, et al. Magnetoliposomes based on manganese ferrite nanoparticles as nanocarriers for antitumor drugs. *RSC Adv*. 2016;6(21):17302–13.

(75) Rodrigues ARO, Matos JOG, Nova Dias AM, Almeida BG, Pires A, Pereira AM, et al. Development of multifunctional liposomes containing magnetic/plasmonic $MnFe_2O_4$/Au core/shell nanoparticles. *Pharmaceutics*. 2019;11(1):10.

(76) Cabrera LI, Somoza Á, Marco JF, Serna CJ, Puerto Morales M. Synthesis and surface modification of uniform MFe_2O_4 (M=Fe, Mn, and Co) nanoparticles with tunable sizes and functionalities. *J Nanoparticle Res*. 2012;14(6):873.

(77) Pereira DSM, Cardoso BD, Rodrigues ARO, Amorim CO, Amaral VS, Almeida BG, et al. Magnetoliposomes containing calcium ferrite nanoparticles for applications in breast cancer therapy. *Pharmaceutics*. 2019;11(9):477.

(78) Cardoso BD, Rodrigues ARO, Almeida BG, Amorim CO, Amaral VS, Castanheira EMS, et al. Stealth magnetoliposomes based on calcium-substituted magnesium ferrite nanoparticles for curcumin transport and release. *Int J Mol Sci*. 2020;21(10):3641.

(79) Ramasamy S, Samathanam B, Reuther H, Adyanpuram MNMS, Enoch IVMV, Potzger K. Molecular encapsulator on the surface of magnetic nanoparticles. Controlled drug release from calcium Ferrite/Cyclodextrin–tethered polymer hybrid. *Colloids Surf B Biointerfaces*. 2018;161:347–55.

(80) Wu M, Gu L, Gong Q, Sun J, Ma Y, Wu H, et al. Strategies to reduce the intracellular effects of iron oxide nanoparticle degradation. *Nanomedicine*. 2017;12(5):555–70.

(81) Abu-Dief AM, Abdel-Fatah SM. Development and functionalization of magnetic nanoparticles as powerful and green catalysts for organic synthesis. *Beni-Suef Univ J Basic Appl Sci*. 2018;7(1):55–67.

(82) Akbarzadeh A, Samiei M, Davaran S. Magnetic nanoparticles: preparation, physical properties, and applications in biomedicine. *Nanoscale Res Lett*. 2012;7(1):144.

(83) Norris MD, Seidel K, Kirschning A. Externally Induced Drug Release Systems with Magnetic Nanoparticle Carriers: An Emerging Field in Nanomedicine. *Adv Ther*. 2019;2(1):1800092.

(84) Ramya S, Thiruvenkataswamy S, Kavithaa K, Preethi S, Winster H, Balachander V, et al. pH Dependent Drug Release of Silibinin, a Polyphenol Conjugated with Magnetic Nanoparticle Against the Human Colon Cancer Cell. *J Clust Sci*. 2020;32(2):305–17.

(85) Tietze R, Zaloga J, Unterweger H, Lyer S, Friedrich RP, Janko C, et al. Magnetic nanoparticle-based drug delivery for cancer therapy. *Biochem Biophys Res Commun*. 2015;468(3):463–70.

(86) Ajinkya N, Yu X, Kaithal P, Luo H, Somani P, Ramakrishna S. Magnetic iron oxide nanoparticle (IONP) synthesis to applications: Present and future. *Materials (Basel)*. 2020;13(20):4644.

(87) Teng Y, Du Y, Shi J, Pong PWT. Magnetic iron oxide nanoparticle-hollow mesoporous silica Spheres: Fabrication and potential application in drug delivery. *Curr Appl Phys*. 2020;20(2):320–5.

(88) Tebaldi ML, Oda CMR, Monteiro LOF, de Barros ALB, Santos CJ, Soares DCF. Biomedical nanoparticle carriers with combined thermal and magnetic response: Current preclinical investigations. *J Magn Magn Mater*. 2018;461:116–27.

(89) Datta NR, Krishnan S, Speiser DE, Neufeld E, Kuster N, Bodis S, et al. Magnetic nanoparticle-induced hyperthermia with appropriate payloads: Paul Ehrlich's "magic (nano)bullet" for cancer theranostics? *Cancer Treat Rev*. 2016;50:217–27.

(90) Raouf I, Khalid S, Khan A, Lee J, Kim HS, Kim MH. A review on numerical modeling for magnetic nanoparticle hyperthermia: Progress and challenges. *J Therm Biol*. 2020;91:102644.

(91) Kobayashi T. Cancer hyperthermia using magnetic nanoparticles. *Biotechnol J*. 2011;6(11):1342–7.

(92) Bleehent NM. Hyperthermia in the treatment of cancer. *Br J Cancer Suppl*. 1982;5:96–100.

(93) Wust P, Hildebrandt B, Sreenivasa G, Rau B, Gellermann J, Riess H, et al. Hyperthermia in combined treatment of cancer. *Lancet*. 2002;3(1):487–97.

(94) Gilchrist RK, Medal R, Shorey WD, Hanselman RC, Parrott JC, Taylor CB. Selective inductive heating of lymph nodes. *Ann Surg*. 1957;146(4):596–606.

(95) Suriyanto, Ng EYK, Kumar SD. Physical mechanism and modeling of heat generation and transfer in magnetic fluid hyperthermia through Néelian and Brownian relaxation: a review. *Biomed Eng Online*. 2017;16:36.

(96) Obaidat IM, Narayanaswamy V, Alaabed S, Sambasivam S, Muralee Gopi CV V. Principles of Magnetic Hyperthermia: A Focus on Using Multifunctional Hybrid Magnetic Nanoparticles. *Magnetochemistry*. 2019;5(4):67.

(97) Shaterabadi Z, Nabiyouni G, Soleymani M. Physics responsible for heating efficiency and self-controlled temperature rise of magnetic nanoparticles in magnetic hyperthermia therapy. *Prog Biophys Mol Biol*. 2018;133:9–19.

(98) Laurent S, Forge D, Port M, Roch A, Robic C, Vander Elst L, et al. Magnetic iron oxide nanoparticles: Synthesis, stabilization, vectorization, physicochemical characterizations, and biological applications. *Chem Rev*. 2008;108(6):2064–110.

(99) Chang D, Lim M, Goos JACM, Qiao R, Ng YY, Mansfeld FM, et al. Biologically targeted magnetic hyperthermia: Potential and limitations. *Front Pharmacol*. 2018;9:831.

(100) Hayashi K, Nakamura M, Miki H, Ozaki S, Abe M, Matsumoto T, et al. Magnetically responsive smart nanoparticles for cancer treatment with a combination of magnetic hyperthermia and remote-control drug release. *Theranostics*. 2014;4(8):834–44.

(101) Zhang ZQ, Song SC. Multiple hyperthermia-mediated release of TRAIL/SPION nanocomplex from thermosensitive polymeric hydrogels for combination cancer therapy. *Biomaterials*. 2017;132:16–27.

(102) Angelakeris M. Magnetic nanoparticles: A multifunctional vehicle for modern theranostics. *Biochim Biophys Acta - Gen Subj*. 2017;1861(6):1642–51.

(103) Thiesen B, Jordan A. Clinical applications of magnetic nanoparticles for hyperthermia. *Int J Hyperth*. 2008;24(6):467–74.

(104) Chandrasekharan P, Tay ZW, Hensley D, Zhou XY, Fung BKL, Colson C, et al. Using magnetic particle imaging systems to localize and guide magnetic hyperthermia treatment: Tracers, hardware, and future medical applications. *Theranostics*. 2020;10(7):2965–81.

(105) Hergt R, Hiergeist R, Zeisberger M, Schüler D, Heyen U, Hilger I, et al. Magnetic properties of bacterial magnetosomes as potential diagnostic and therapeutic tools. *J Magn Magn Mater*. 2005;293(1):80–6.

(106) Alphandéry E, Faure S, Seksek O, Guyot F, Chebbi I. Chains of magnetosomes extracted from AMB-1 magnetotactic bacteria for application in alternative magnetic field cancer therapy. *ACS Nano*. 2011;5(8):6279–96.

(107) Kossatz S, Ludwig R, Dähring H, Ettelt V, Rimkus G, Marciello M, et al. High therapeutic efficiency of magnetic hyperthermia in xenograft models achieved with moderate temperature dosages in the tumor area. *Pharm Res*. 2014;31(12):3274–88.

(108) Mamiya H. Recent advances in understanding magnetic nanoparticles in ac magnetic fields and optimal design for targeted hyperthermia. *J Nanomater*. 2013;2013.

(109) Cai Z, Wu C, Yang L, Wang D, Ai H. Assembly-Controlled Magnetic Nanoparticle Clusters as MRI Contrast Agents. *ACS Biomater Sci Eng*. 2020;6(5):2533–42.

(110) Hoult DI, Bhakar B. NMR signal reception: Virtual photons and coherent spontaneous emission. *Concepts Magn Reson*. 1997;9(5):277–97.

(111) Shen Z, Wu A, Chen X. Iron Oxide Nanoparticle Based Contrast Agents for Magnetic Resonance Imaging. *Mol Pharm*. 2017;14(5):1352–64.

(112) Shan L, Chopra A, Leung K, Eckelman WC, Menkens AE. Characterization of nanoparticle-based contrast agents for molecular magnetic resonance imaging. *J Nanoparticle Res*. 2012;14(9):1122.

(113) Fu S, Cai Z, Ai H. Stimulus-Responsive Nanoparticle Magnetic Resonance Imaging Contrast Agents: Design Considerations and Applications. *Adv Healthc Mater*. 2020;10(5):2001091.

(114) Mlynárik V. Introduction to nuclear magnetic resonance. *Anal Biochem*. 2017;529:4–9.

(115) Kircher MF, Allport JR, Graves EE, Love V, Josephson L, Lichtman AH, et al. In Vivo High Resolution Three-Dimensional Imaging of Antigen-Specific Cytotoxic T-Lymphocyte Trafficking to Tumors. *Cancer Res*. 2003;63(20):6838–46.

(116) Kresse M, Wagner S, Pfefferer D, Lawaczeck R, Elste V, Semmler W. Targeting of ultrasmall superparamagnetic iron oxide (USPIO) particles to tumor cells in vivo by using transferrin receptor pathways. *Magn Reson Med*. 1998;40(2):236–42.

(117) Perez JM, Josephson L, Weissleder R. Use of magnetic nanoparticles as nanosensors to probe for molecular interactions. *ChemBioChem*. 2004;5(3):261–4.

(118) De Haan HW. Mechanisms of proton spin dephasing in a system of magnetic particles. *Magn Reson Med*. 2011;66(6):1748–58.

(119) Anani T, Rahmati S, Sultana N, David AE. MRI-traceable theranostic nanoparticles for targeted cancer treatment. *Theranostics*. 2020;11(2):579–601.

(120) Scheenen TWJ, Zamecnik P. The Role of Magnetic Resonance Imaging in (Future) Cancer Staging: Note the Nodes. *Invest Radiol*. 2021;56(1):42–9.

(121) Nayeem J, Al-Bari MAA, Mahiuddin M, Rahman MA, Mefford OT, Ahmad H, et al. Silica coating of iron oxide magnetic nanoparticles by reverse microemulsion method and their functionalization with cationic polymer P(NIPAm-co-AMPTMA) for antibacterial vancomycin immobilization. *Colloids Surf A Physicochem Eng Asp*. 2021;611:125857.

(122) Reczyńska K, Marszałek M, Zarzycki A, Reczyński W, Kornaus K, Pamuła E, et al. Superparamagnetic iron oxide nanoparticles modified with silica layers as potential agents for lung cancer treatment. *Nanomaterials*. 2020;10(6):1076.

(123) Li Y, Chen H, Wu J, He Q, Li Y, Yang W, et al. Preparation and characterization of APTES modified magnetic MMT capable of using as anisotropic nanoparticles. *Appl Surf Sci*. 2018;447:393–400.

(124) Zarinwall A, Waniek T, Saadat R, Braun U, Sturm H, Garnweitner G. Comprehensive Characterization of APTES Surface Modifications of Hydrous Boehmite Nanoparticles. *Langmuir*. 2021;37(1):171–9.

(125) Liu Y, Li Y, Li XM, He T. Kinetics of (3-aminopropyl)triethoxylsilane (APTES) silanization of superparamagnetic iron oxide nanoparticles. *Langmuir*. 2013;29(49):15275–82.

(126) Yamaura M, Camilo RL, Sampaio LC, Macêdo MA, Nakamura M, Toma HE. Preparation and characterization of (3-aminopropyl)triethoxysilane-coated magnetite nanoparticles. *J Magn Magn Mater*. 2004;279(2–3):210–7.

(127) Saif B, Wang C, Chuan D, Shuang S. Synthesis and Characterization of Fe_3O_4 Coated on APTES as Carriers for Morin-Anticancer Drug. *J Biomater Nanobiotechnol*. 2015;6(4):267–75.

(128) Bini RA, Marques RFC, Santos FJ, Chaker JA, Jafelicci M. Synthesis and functionalization of magnetite nanoparticles with different amino-functional alkoxysilanes. *J Magn Magn Mater*. 2012;324(4):534–9.

(129) Saravanan P, Jayamoorthy K, Anandakumar S. Fluorescence quenching of APTES by Fe_2O_3 nanoparticles – Sensor and antibacterial applications. *J Lumin*. 2016;178:241–8.

(130) Cazares-Cortes E, Cabana S, Boitard C, Nehlig E, Griffete N, Fresnais J, et al. Recent insights in magnetic hyperthermia: From the “hot-spot” effect for local delivery to combined magneto-photo-thermia using magneto-plasmonic hybrids. *Adv Drug Deliv Rev*. 2019;138:233–46.

(131) Armelles G, Cebollada A, García-Martín A, González MU. Magnetoplasmonics: Combining Magnetic and Plasmonic Functionalities. *Adv Opt Mater*. 2013;1(1):10–35.

(132) Lim J, Majetich SA. Composite magnetic-plasmonic nanoparticles for biomedicine: Manipulation and imaging. *Nano Today*. 2013;8(1):98–113.

(133) Stafford S, Garcia RS, Gun’ko YK. Multimodal magnetic-plasmonic nanoparticles for biomedical applications. *Appl Sci*. 2018;8(1):97.

(134) Sevenler D, Ünlü NL, Ünlü, MS. Nanoparticle Biosensing with Interferometric Reflectance Imaging. In: Vestergaard MC, Kerman K, Hsing I-M, Tamiya E, editors. *Nanobiosensors and Nanobioanalyses*. 1st ed. Springer Japan; 2015. p. 81–95.

(135) Barnes WL. Particle plasmons: Why shape matters. *Am J Phys*. 2016;84(8):593–601.

(136) Stockman MI. Nanoplasmonics: The physics behind the applications. *Phys Today*. 2011;64(2):39–44.

(137) Kneipp K. Surface-enhanced raman scattering. *Phys Today*. 2007;60(11):40–6.

(138) Wang W, Wang J, Ding Y. Gold nanoparticle-conjugated nanomedicine: design, construction, and structure-efficacy relationship studies. *J Mater Chem B*. 2020;8(22):4813–30.

(139) Malik P, Mukherjee TK. Recent advances in gold and silver nanoparticle based therapies for lung and breast cancers. *Int J Pharm*. 2018;553(1–2):483–509.

(140) Wu J, Qu Y, Yu Q, Chen H. Gold nanoparticle layer: A versatile nanostructured platform for biomedical applications. *Mater Chem Front*. 2018;2(12):2175–90.

(141) Daruich De Souza C, Ribeiro Nogueira B, Rostelato MECM. Review of the methodologies used in the synthesis gold nanoparticles by chemical reduction. *J Alloys Compd*. 2019;798:714–40.

(142) Yeh Y-C, Creran B, Rotello VM. Gold Nanoparticles: Preparation, Properties, and Applications in Bionanotechnology. *Nanoscale*. 2012;4(6):1871–80.

(143) Amendola V, Pilot R, Frasconi M, Maragò OM, Iatì MA. Surface plasmon resonance in gold nanoparticles: A review. *J Phys Condens Matter*. 2017;29:203002.

(144) Huang X, El-Sayed MA. Gold nanoparticles: Optical properties and implementations in cancer diagnosis and photothermal therapy. *J Adv Res*. 2010;1(1):13–28.

(145) Lu Y, Rosenholm JM. Gold nanoparticle-enhanced photodynamic therapy: effects of surface charge and mitochondrial targeting. *Ther Deliv*. 2015;6(3):307–21.

(146) Shukla N, Singh B, Kim HJ, Park MH, Kim K. Combinational Chemotherapy and Photothermal Therapy Using a Gold Nanorod Platform for Cancer Treatment. *Part Part Syst Charact*. 2020;37(8):2000099.

(147) Yang W, Liang H, Ma S, Wang D, Huang J. Gold nanoparticle based photothermal therapy: Development and application for effective cancer treatment. *Sustain Mater Technol*. 2019;22:e00109.

(148) Vines JB, Yoon JH, Ryu NE, Lim DJ, Park H. Gold nanoparticles for photothermal cancer therapy. *Front Chem*. 2019;7:167.

(149) Duong VT, Thuong TT, Lien NTH, Hoa DQ, Nhung TH. The Light-to-heat Conversion of Gold Nanoshells and Nanorods in Tissues. *Commun Phys*. 2016;24(3S2):83–8.

(150) Yuba E. Development of functional liposomes by modification of stimuli-responsive materials and their biomedical applications. *J Mater Chem B*. 2020;8(6):1093–107.

(151) Liu C, Zhang L, Zhu W, Guo R, Sun H, Chen X, et al. Barriers and Strategies of Cationic Liposomes for Cancer Gene Therapy. *Mol Ther - Methods Clin Dev*. 2020;18(September):751–64.

(152) Fan Y, Marioli M, Zhang K. Analytical characterization of liposomes and other lipid nanoparticles for drug delivery. *J Pharm Biomed Anal*. 2021;192:113642.

(153) Trucillo P, Campardelli R, Reverchon E. Liposomes: From bangham to supercritical fluids. *Processes*. 2020;8(9):1022.

(154) Yan W, Leung SSY, To KKW. Updates on the use of liposomes for active tumor targeting in cancer therapy. *Nanomedicine*. 2019;15(3):303–18.

(155) Lee MK. Liposomes for enhanced bioavailability of water-insoluble drugs: In vivo evidence and recent approaches. *Pharmaceutics*. 2020;12(3):264.

(156) Allen TM, Cullis PR. Liposomal drug delivery systems: From concept to clinical applications. *Adv Drug Deliv Rev*. 2013;65(1):36–48.

(157) Rodrigues ARO, Almeida BG, Rodrigues JM, Queiroz MJRP, Calhelha RC, Ferreira ICFR, et al. Magnetoliposomes as carriers for promising antitumor thieno[3,2-b]pyridin-7-arylamines: photophysical and biological studies. *RSC Adv*. 2017;7(25):15352–61.

(158) Khan AA, Allemailem KS, Almatroodi SA, Almatroudi A, Rahmani AH. Recent strategies towards the surface modification of liposomes: an innovative approach for different clinical applications. *3 Biotech*. 2020;10(4):163.

(159) Li Y, Cong H, Wang S, Yu B, Shen Y. Liposomes modified with bio-substances for cancer treatment. *Biomater Sci*. 2020;8(23):6442–68.

(160) Jabalera Y, Fernández-Vivas A, Iglesias GR, Delgado Á V., Jimenez-Lopez C. Magnetoliposomes of mixed biomimetic and inorganic magnetic nanoparticles as enhanced hyperthermia agents. *Colloids Surf B Biointerfaces*. 2019;183:110435.

(161) Piazzini V, Landucci E, Graverini G, Pellegrini-Giampietro DE, Bilia AR, Bergonzi MC. Stealth and cationic nanoliposomes as drug delivery systems to increase andrographolide BBB permeability. *Pharmaceutics*. 2018;10(3):128.

(162) Rodrigues ARO, Mendes PMF, Silva PML, Machado VA, Almeida BG, Araújo JP, et al. Solid and aqueous magnetoliposomes as nanocarriers for a new potential drug active against breast cancer. *Colloids Surf B Biointerfaces*. 2017;158:460–8.

(163) Namdari M, Cheraghi M, Negahdari B, Eatemadi A, Daraee H. Recent advances in magnetoliposome for heart drug delivery. *Artif Cells, Nanomedicine Biotechnol*. 2017;45(6):1051–7.

(164) Shin TH, Ketebo AA, Lee DY, Lee S, Kang SH, Basith S, et al. Decrease in membrane fluidity and traction force induced by silica-coated magnetic nanoparticles. *J Nanobiotechnology*. 2021;19(1):21.

(165) Rio ISR, Rodrigues ARO, Rodrigues AP, Almeida BG, Pires A, Pereira AM, et al. Development of novel magnetoliposomes containing nickel ferrite nanoparticles covered with gold for applications in thermotherapy. *Materials (Basel)*. 2020;13(4):815.

(166) Shirmardi Shaghasemi B, Virk MM, Reimhult E. Optimization of Magneto-thermally Controlled Release Kinetics by Tuning of Magnetoliposome Composition and Structure. *Sci Rep.* 2017;7(1):7474.

(167) Fortes Brollo ME, Domínguez-Bajo A, Tabero A, Domínguez-Arca V, Gisbert V, Prieto G, et al. Combined Magnetoliposome Formation and Drug Loading in One Step for Efficient Alternating Current-Magnetic Field Remote-Controlled Drug Release. *ACS Appl Mater Interfaces*. 2020;12(4):4295–307.

(168) Vlasova KY, Piroyan A, Le-Deygen IM, Vishwasrao HM, Ramsey JD, Klyachko NL, et al. Magnetic liposome design for drug release systems responsive to super-low frequency alternating current magnetic field (AC MF). *J Colloid Interface Sci*. 2019;552:689–700.

(169) Attia MF, Anton N, Wallyn J, Omran Z, Vandamme TF. An overview of active and passive targeting strategies to improve the nanocarriers efficiency to tumour sites. *J Pharm Pharmacol*. 2019;71(8):1185–98.

(170) Rodrigues ARO, Gomes IT, Almeida BG, Araújo JP, Castanheira EMS, Coutinho PJG. Magnetic liposomes based on nickel ferrite nanoparticles for biomedical applications. *Phys Chem Chem Phys*. 2015;17(27):18011–21.

(171) Veloso SRS, Ferreira PMT, Martins JA, Coutinho PJG, Castanheira EMS. Magnetogels: Prospects and main challenges in biomedical applications. *Pharmaceutics*. 2018;10(3):145.

(172) Veloso SRS, Almeida BG, Coutinho PJG, Castanheira EMS, Martins JA, Jervis PJ, et al. Dehydropeptide-based plasmonic magnetogels: A supramolecular composite nanosystem for multimodal cancer therapy. *J Mater Chem B*. 2019;8(1):45–64.

(173) Veloso SRS, Andrade RGD, Castanheira EMS. Review on the advancements of magnetic gels: towards multifunctional magnetic liposome-hydrogel composites for biomedical applications. *Adv Colloid Interface Sci*. 2021;288:102351.

(174) Weeber R, Kantorovich S, Holm C. Ferrogels cross-linked by magnetic particles: Field-driven deformation and elasticity studied using computer simulations. *J Chem Phys*. 2015;143(15):154901.

(175) Santos PJ, Macfarlane RJ. Reinforcing Supramolecular Bonding with Magnetic Dipole Interactions to Assemble Dynamic Nanoparticle Superlattices. *J Am Chem Soc*. 2020;142(3):1170–4.

(176) Rozhkov DA, Pyanzina ES, Novak E V., Cerdà JJ, Sintes T, Ronti M, et al. Self-assembly of polymer-like structures of magnetic colloids: Langevin dynamics study of basic topologies. *Mol Simul*. 2018;44(6):507–15.

(177) Zubarev AY. Rheological Properties of Polydisperse Magnetic Fluids. Effect of Chain Aggregates. *Fluids*. 2001;93(1):80–8.

(178) Fu R, Yan YY, Roberts C. Study of the effect of dipole interactions on hyperthermia heating the cluster composed of superparamagnetic nanoparticles. *AIP Adv*. 2015;5(12):127232.

(179) Rosa AP, Cunha FR. The influence of dipolar particle interactions on the magnetization and the rotational viscosity of ferrofluids. *Phys Fluids*. 2019;31(5):052006.

(180) Sung B, Kim MH, Abelmann L. Magnetic microgels and nanogels: Physical mechanisms and biomedical applications. *Bioeng Transl Med*. 2021;6(1):e10190.

(181) Bonhome-Espinosa AB, Campos F, Rodriguez IA, Carriel V, Marins JA, Zubarev A, et al. Effect of particle concentration on the microstructural and macromechanical properties of biocompatible magnetic hydrogels. *Soft Matter*. 2017;13(16):2928–41.

(182) Soares PIP, Machado D, Laia C, Pereira LCJ, Coutinho JT, Ferreira IMM, et al. Thermal and magnetic properties of chitosan-iron oxide nanoparticles. *Carbohydr Polym*. 2016;149:382–90.

(183) Villamin ME, Kitamoto Y. Influence of pH on Dynamic Magnetic Susceptibility of Iron-Oxide Nanoparticles in a Chitosan Hydrogel Matrix. *IEEE Trans Magn*. 2019;55(2):2019–22.

(184) Crippa F, Moore TL, Mortato M, Geers C, Haeni L, Hirt AM, et al. Dynamic and biocompatible thermo-responsive magnetic hydrogels that respond to an alternating magnetic field. *J Magn Magn Mater*. 2017;427(October 2016):212–9.

(185) Zadrail A, Tokárová V, Tpánek F. Remotely triggered release from composite hydrogel sponges. *Soft Matter*. 2012;8(6):1811–6.

(186) Echeverria C, Fernandes S, Godinho M, Borges J, Soares P. Functional Stimuli-Responsive Gels: Hydrogels and Microgels. *Gels*. 2018;4(2):54.

(187) Weiner AL, Carpenter-Green SS, Soehngen EC, Lenk RP, Popescu MC. Liposome–collagen gel matrix: A novel sustained drug delivery system. *J Pharm Sci*. 1985;74(9):922–5.

(188) Grijalvo S, Mayr J, Eritja R, Díaz DD. Biodegradable liposome-encapsulated hydrogels for biomedical applications: A marriage of convenience. *Biomater Sci*. 2016;4(4):555–74.

(189) Zhao F, Yao D, Guo R, Deng L, Dong A, Zhang J. Composites of polymer hydrogels and nanoparticulate systems for biomedical and pharmaceutical applications. *Nanomaterials*. 2015;5(4):2054–130.

(190) Zylberberg C, Matosevic S. Bioengineered liposome-scaffold composites as therapeutic delivery systems. *Ther Deliv*. 2017;8(6):425–45.

(191) Wickremasinghe NC, Kumar VA, Hartgerink D. Two-Step Self-Assembly of Liposome-Multidomain Peptide Nano fiber Hydrogel for Time-Controlled Release. *Biomacromolecules*. 2014;15(10):3587–3595.

(192) Yao H, Lu H, Zou R, Chen X, Xu H. Preparation of encapsulated resveratrol liposome thermosensitive gel and evaluation of its capability to repair sciatic nerve injury in rats. *J Nanomater*. 2020;2020:2840162.

(193) Elkhoury K, Russell CS, Sanchez-Gonzalez L, Mostafavi A, Williams TJ, Kahn C, et al. Soft-Nanoparticle Functionalization of Natural Hydrogels for Tissue Engineering Applications. *Adv Healthc Mater*. 2019;8(18):e1900506.

(194) Veloso SRS, Andrade RGD, Ribeiro BC, Fernandes AVF, Rodrigues ARO, Martins JA, et al. Magnetoliposomes incorporated in peptide-based hydrogels: Towards development of magnetolipogels. *Nanomaterials*. 2020;10(9):1702.

(195) Accardo A, Morelli G. Review peptide-targeted liposomes for selective drug delivery: Advantages and problematic issues. *Biopolymers*. 2015;104(5):462–79.

(196) Hanuš J, Ullrich M, Dohnal J, Singh M, Štěpánek F. Remotely controlled diffusion from magnetic liposome microgels. *Langmuir*. 2013;29(13):4381–7.

(197) De Cogan F, Booth A, Gough JE, Webb SJ. Spatially controlled apoptosis induced by released nickel(II) within a magnetically responsive nanostructured biomaterial. *Soft Matter*. 2013;9(7):2245–53.

(198) De Cogan F, Booth A, Gough JE, Webb SJ. Conversion of Magnetic Impulses into Cellular Responses by Self-Assembled Nanoparticle-Vesicle Hydrogels. *Angew Chemie*. 2011;123(51):12498–501.

(199) Hernández-Hernández AA, Aguirre-Álvarez G, Cariño-Cortés R, Mendoza-Huizar LH, Jiménez-Alvarado R. Iron oxide nanoparticles: synthesis, functionalization, and applications in diagnosis and treatment of cancer. *Chem Pap*. 2020;74(11):3809–24.

(200) Israel LL, Galstyan A, Holler E, Ljubimova JY. Magnetic iron oxide nanoparticles for imaging, targeting and treatment of primary and metastatic tumors of the brain. *J Control Release*. 2020;320:45–62.

(201) Zhi D, Yang T, Yang J, Fu S, Zhang S. Targeting strategies for superparamagnetic iron oxide nanoparticles in cancer therapy. *Acta Biomater*. 2020;102:13–34.

(202) Aisida SO, Akpa PA, Ahmad I, Zhao T kai, Maaza M, Ezema FI. Bio-inspired encapsulation and functionalization of iron oxide nanoparticles for biomedical applications. *Eur Polym J*. 2020;122:109371.

(203) Kang DH, Jung HS, Ahn N, Yang SM, Seo S, Suh KY, et al. Janus-compartmental alginate microbeads having polydiacetylene liposomes and magnetic nanoparticles for visual lead(II) detection. *ACS Appl Mater Interfaces*. 2014;6(13):10631–7.

(204) Pittermannová A, Ruberová Z, Zadražil A, Bremond N, Bibette J, Štěpánek F. Microfluidic fabrication of composite hydrogel microparticles in the size range of blood cells. *RSC Adv*. 2016;6(105):103532–40.

(205) Van Elk M, Lorenzato C, Ozbakir B, Oerlemans C, Storm G, Nijsen F, et al. Alginate microgels loaded with temperature sensitive liposomes for magnetic resonance imageable drug release and microgel visualization. *Eur Polym J*. 2015;72:620–31.

(206) Mart RJ, Liem KP, Webb SJ. Magnetically-controlled release from hydrogel-supported vesicle assemblies. *Chem Commun*. 2009;2009(17):2287–9.

(207) Robert Blumenthal RI. Magnetically Triggered Drug Release from Liposome Embedded Gel. *J Nanomedine Biotherapeutic Discov*. 2014;4(3):1000130.

(208) Ullrich M, Hanuš J, Štěpánek F. Remote control of enzymatic reaction in compartmentalized microparticles: A system for the delivery of unstable actives. *Chem Eng Sci*. 2015;125:191–9.

(209) Zhu H, Srivastava R, Brown Q, McShane MJ. Combined physical and chemical immobilization of glucose oxidase in alginate microspheres improves stability of encapsulation and activity. *Bioconjug Chem*. 2005;16(6):1451–8.

(210) Won K, Kim S, Kim KJ, Park HW, Moon SJ. Optimization of lipase entrapment in Ca-alginate gel beads. *Process Biochem*. 2005;40(6):2149–54.

(211) Adler-Abramovich L, Gazit E. The physical properties of supramolecular peptide assemblies: From building block association to technological applications. *Chem Soc Rev*. 2014;43(20):6881–93.

(212) Cai Y, Zheng C, Xiong F, Ran W, Zhai Y, Zhu HH, et al. Recent Progress in the Design and Application of Supramolecular Peptide Hydrogels in Cancer Therapy. *Adv Healthc Mater*. 2021;10(1):2001239.

(213) Veloso SRS, Silva JFG, Hilliou L, Moura C, Coutinho PJG, Martins JA, et al. Impact of citrate and lipid-functionalized magnetic nanoparticles in dehydropeptide supramolecular magnetogels: Properties, design and drug release. *Nanomaterials*. 2021;11(1):16.

(214) El-Toni AM, Habila MA, Labis JP, Alothman ZA, Alhoshan M, Elzatahry AA, et al. Design, synthesis and applications of core-shell, hollow core, and nanorattle multifunctional nanostructures. *Nanoscale*. 2016;8(5):2510–31.

(215) Massou H, Albigot R, Prats M. Carboxyfluorescein fluorescence experiments. *Biochem Educ*. 2000;28(3):171–3.

(216) Reddy SMM, Dorishetty P, Deshpande AP, Shanmugam G. Hydrogelation Induced by Change in Hydrophobicity of Amino Acid Side Chain in Fmoc-Functionalised Amino Acid: Significance of Sulfur on Hydrogelation. *ChemPhysChem*. 2016;17(14):2170–80.

(217) Khanna L, Verma NK. Biocompatibility and superparamagnetism in novel silica/$CaFe_2O_4$ nanocomposite. *Mater Lett*. 2014;128:376–9.

(218) Nakagawa T, Takagai Y. Simple Synthesis of Gold Nanoparticles by Sodium Borohydride Reduction Method and Their Ligand Exchange Reaction. *Bunseki Kagaku*. 2019;68(10):751–5.

(219) Brown KR, Walter DG, Natan MJ. Seeding of colloidal Au nanoparticle solutions. 2. Improved control of particle size and shape. *Chem Mater*. 2000;12(2):306–13.

(220) Zhai Y, Zhai J, Wang Y, Guo S, Ren W, Dong S. Fabrication of iron oxide core/gold shell submicrometer spheres with nanoscale surface roughness for efficient surface-enhanced Raman scattering. *J Phys Chem C*. 2009;113(17):7009–14.

(221) Franzè S, Selmin F, Rocco P, Colombo G, Casiraghi A, Cilurzo F. Preserving the integrity of liposomes prepared by ethanol injection upon freeze-drying: Insights from combined molecular dynamics simulations and experimental data. *Pharmaceutics*. 2020;12(6):530.

(222) Cardoso BD, Rio ISR, Rodrigues ARO, Fernandes FCT, Almeida BG, Pires A, et al. Magnetoliposomes containing magnesium ferrite nanoparticles as nanocarriers for the model drug curcumin. *R Soc Open Sci*. 2018;5(10):181017.

(223) Bates RG, Bower VE. Alkaline Solutions for pH Control. *Anal Chem*. 1956;28(8):1322–4.

(224) Perrin DD, Dempsey B. *Buffers for pH and Metal Ion Control*. 1st ed. London, England: Springer, Dordrecht; 1974. 24–76 p.

(225) Veloso SRS, Jervis PJ, Silva JFG, Hilliou L, Moura C, Pereira DM, et al. Supramolecular ultra-short carboxybenzyl-protected dehydropeptide-based hydrogels for drug delivery. *Mater Sci Eng C*. 2021;122:111869.

(226) Mondal S, Saha M, Ghosh M, Santra S, Khan MA, Das Saha K, et al. Programmed supramolecular nanoassemblies: Enhanced serum stability and cell specific triggered release of anti-cancer drugs. *Nanoscale Adv*. 2019;1(4):1571–80.

(227) Nandel FS, Sahrawat TR. Conformational study of poly-ΔAbu peptides and construction of amphipathic nanostructure. *Biopolymers*. 2009;92(1):44–51.

(228) Buczek A, Siodłak D, Bujak M, Makowski M, Kupka T, Broda MA. Impact of the ΔPhe configuration on the Boc-Gly-ΔPhe-NHMe conformation: experiment and theory. *Struct Chem*. 2019;30(5):1685–97.

(229) Valeur E, Bradley M. Amide bond formation: Beyond the myth of coupling reagents. *Chem Soc Rev*. 2009;38(2):606–31.

(230) Ferreira PMT, Monteiro LS, Pereira G, Ribeiro L, Sacramento J, Silva L. Reactivity of dehydroamino acids and dehydrodipeptides towards N- bromosuccinimide: Synthesis of β-bromo- and β,β-dibromodehydroamino acid derivatives and of substituted 4-imidazolidinones. *European J Org Chem*. 2007;2007(35):5934–49.

(231) Slomp G. Analysis of ABX Spectra in NMR Spectroscopy. *Appl Spectrosc Rev*. 1969;2(2):263–351.

(232) Haines-Butterick L, Rajagopal K, Branco M, Salick D, Rughani R, Pilarz M, et al. Controlling hydrogelation kinetics by peptide design for three-dimensional encapsulation and injectable delivery of cells. *Proc Natl Acad Sci U S A*. 2007;104(19):7791–6.

(233) Chakraborty P, Tang Y, Yamamoto T, Yao Y, Guterman T, Zilberzwige-Tal S, et al. Unusual Two-Step Assembly of a Minimalistic Dipeptide-Based Functional Hypergelator. *Adv Mater*. 2020;32(9):1906043.

(234) Rizwan M, Yahya R, Hassan A, Yar M, Azzahari AD, Selvanathan V, et al. pH sensitive hydrogels in drug delivery: Brief history, properties, swelling, and release mechanism, material selection and applications. *Polymers (Basel)*. 2017;9(4):137.

(235) Shi Y, Li D, Ding J, He C, Chen X. Physiologically relevant pH- and temperature-responsive polypeptide hydrogels with adhesive properties. *Polym Chem*. 2021;12(19):2832–9.

(236) Jervis PJ, Amorim C, Pereira T, Martins JA, Ferreira PMT. Exploring the properties and potential biomedical applications of NSAID-capped peptide hydrogels. *Soft Matter*. 2020;16(44):10001–12.

(237) Draper ER, Adams DJ. Controlling the Assembly and Properties of Low-Molecular-Weight Hydrogelators. *Langmuir*. 2019;35:6506–21.

(238) Kan X, Liu H, Pan Q, Li Z, Zhao Y. Anion-π interactions: From concept to application. *Chinese Chem Lett*. 2018;29(2):261–6.

(239) Tuo DH, Liu W, Wang XY, Wang XD, Ao YF, Wang QQ, et al. Toward Anion-π Interactions Directed Self-Assembly with Predesigned Dual Macrocyclic Receptors and Dianions. *J Am Chem Soc*. 2019;141(2):1118–25.

(240) Liao JZ, Dui XJ, Zhang HL, Wu XY, Lu CZ. Polyoxometalate anion-π interaction-directed assembly of a three-dimensional hydrogen-bonded supramolecular framework with nanoscale porosity. *CrystEngComm*. 2014;16(46):10530–3.

(241) Chen L, Revel S, Morris K, C. Serpell L, Adams DJ. Effect of molecular structure on the properties of naphthalene-dipeptide hydrogelators. *Langmuir*. 2010;26(16):13466–71.

(242) Adams DJ, Mullen LM, Berta M, Chen L, Frith WJ. Relationship between molecular structure, gelation behaviour and gel properties of Fmoc-dipeptides. *Soft Matter*. 2010;6(9):1971–80.

(243) Vilaça H, Pereira G, Castro TG, Hermenegildo BF, Shi J, Faria TQ, et al. New self-assembled supramolecular hydrogels based on dehydropeptides. *J Mater Chem B*. 2015;3(30):6355–67.

(244) Veloso SRS. *Multifunctional nanogels containing magnetic/plasmonic nanoparticles for therapeutic applications*. University of Minho; 2018.

(245) Baby DK. Rheology of hydrogels. In: Thomas S, Chandrasekharakurup S, Chandran N, editors. *Rheology of Polymer Blends and Nanocomposites: Theory, Modelling and Applications*. 1st ed. Elsevier Inc.; 2019. p. 193–204.

(246) Sathaye S, Mbi A, Sonmez C, Chen Y, Blair DL, Schneider JP, et al. Rheology of peptide- and protein-based physical hydrogels: Are everyday measurements just scratching the surface? *Wiley Interdiscip Rev Nanomed Nanobiotechnology*. 2015;7(1):34–68.

(247) Yan C, Pochan DJ. Rheological properties of peptide-based hydrogels for biomedical and other applications. *R Soc Chem*. 2010;39(9):3528–40.

(248) Zuidema JM, Rivet CJ, Gilbert RJ, Morrison FA. A protocol for rheological characterization of hydrogels for tissue engineering strategies. *J Biomed Mater Res - Part B Appl Biomater*. 2014;102(5):1063–73.

(249) Zheng Y, Liang Y, Zhang D, Sun X, Liang L, Li J, et al. Gelatin-Based Hydrogels Blended with Gellan as an Injectable Wound Dressing. *ACS Omega*. 2018;3(5):4766–75.

(250) Frith WJ, Donald AM, Adams DJ, Aufderhorst-Roberts A. Gels formed from amino-acid derivatives, their novel rheology as probed by bulk and particle tracking rheological methods. *J Nonnewton Fluid Mech*. 2015;222:104–11.

(251) Cox TR, Erler JT. Remodeling and homeostasis of the extracellular matrix: Implications for fibrotic diseases and cancer. *DMM Dis Model Mech*. 2011;4(2):165–78.

(252) Kocen R, Gasik M, Gantar A, Novak S. Viscoelastic behaviour of hydrogel-based composites for tissue engineering under mechanical load. *Biomed Mater*. 2017;12(2):025004.

(253) Hyun K, Kim SH, Ahn KH, Lee SJ. Large amplitude oscillatory shear as a way to classify the complex fluids. *J Nonnewton Fluid Mech*. 2002;107(1–3):51–65.

(254) Wee MSM. *Physico-chemical characterisation and functionality of the polysaccharide extracted from the New Zealand black tree fern, Cyathea medullaris*. Massey University; 2015.

(255) Donley GJ, Singh PK, Shetty A, Rogers SA. Elucidating the G'' overshoot in soft materials with a yield transition via a time-resolved experimental strain decomposition. *Proc Natl Acad Sci U S A*. 2020;117(36):21945–52.

(256) Pande S, Islam MM, Mohanta SC, Uddin N. Single-Step Synthesis of Manganese Ferrite Nanoparticles with Enhanced Magnetization via Chemical Co-precipitation Route. *J Sci Res*. 2019;11(2):225–34.

(257) Rotjanasuworapong K, Lerdwijitjarud W, Sirivat A. Synthesis and characterization of $Fe_{0.8}Mn_{0.2}Fe_2O_4$ ferrite nanoparticle with high saturation magnetization via the surfactant assisted co-precipitation. *Nanomaterials*. 2021;11(4):876.

(258) Ereath Beeran A, Nazeer SS, Fernandez FB, Muvvala KS, Wunderlich W, Anil S, et al. An aqueous method for the controlled manganese (Mn^{2+}) substitution in superparamagnetic iron oxide nanoparticles for contrast enhancement in MRI. *Phys Chem Chem Phys*. 2015;17(6):4609–19.

(259) Aono H, Hirazawa H, Naohara T, Maehara T, Kikkawa H, Watanabe Y. Synthesis of fine magnetite powder using reverse coprecipitation method and its heating properties by applying AC magnetic field. *Mater Res Bull*. 2005;40(7):1126–35.

(260) Kazemzadeh H, Ataie A, Rashchi F. Synthesis of Magnetite Nano-Particles By Reverse Co-Precipitation. *Int J Mod Phys Conf Ser*. 2012;5:160–7.

(261) Korsakova S, Kotsikau DA, Haiduk YS, Pankov V V. Synthesis and Physicochemical Properties of $Mn_xFe_{3-x}O_4$ Solid Solutions. *Condens Matter Interphases*. 2020;22(4):417–29.

(262) Modaresi N, Afzalzadeh R, Aslibeiki B, Kameli P. Competition between the impact of cation distribution and crystallite size on properties of $Mn_xFe_{3-x}O_4$ nanoparticles synthesized at room temperature. *Ceram Int*. 2017;43(17):15381–91.

(263) Taufiq A, Sunaryono, Rachman Putra EG, Okazawa A, Watanabe I, Kojima N, et al. Nanoscale Clustering and Magnetic Properties of $Mn_xFe_{3-x}O_4$ Particles Prepared from Natural Magnetite. *J Supercond Nov Magn*. 2015;28(9):2855–63.

(264) Hergt R, Dutz S, Röder M. Effects of size distribution on hysteresis losses of magnetic nanoparticles for hyperthermia. *J Phys Condens Matter*. 2008;20(38):5214.

(265) Goya GF, Lima E, Arelaro AD, Torres T, Rechenberg HR, Rossi L, et al. Magnetic Hyperthermia With Fe_3O_4 Nanoparticles: The Influence of Particle Size on Energy. *IEEE Trans Magn*. 2008;44(11):4444–7.

(266) Rodriguez-Carvajal J. FullProf. *Newsletter*; 2001. p. 26:12-19.

(267) Khlebtsov NG. Determination of size and concentration of gold nanoparticles from extinction spectra. *Anal Chem*. 2008;80(17):6620–5.

(268) Li Y, Baeta C, Aras O, Daniel M-C. Preparation of lisinopril-capped gold nanoparticles for molecular imaging of angiotensin-converting enzyme. *Smart Biomed Physiol Sens Technol VI*. 2009;7313:731304.

(269) Moraes Silva S, Tavallaie R, Sandiford L, Tilley RD, Gooding JJ. Gold coated magnetic nanoparticles: From preparation to surface modification for analytical and biomedical applications. *Chem Commun*. 2016;52(48):7528–40.

(270) Wang L, Park HY, Lim SII, Schadt MJ, Mott D, Luo J, et al. Core@shell nanomaterials: Gold-coated magnetic oxide nanoparticles. *J Mater Chem*. 2008;18(23):2629–35.

(271) León Félix L, Sanz B, Sebastián V, Torres TE, Sousa MH, Coaquira JAH, et al. Gold-decorated magnetic nanoparticles design for hyperthermia applications and as a potential platform for their surface-functionalization. *Sci Rep*. 2019;9(1):4185.

(272) Wang H, Goodrich GP, Tam F, Oubre C, Nordlander P, Halas NJ. Controlled texturing modifies the surface topography and plasmonic properties of Au nanoshells. *J Phys Chem B*. 2005;109(22):11083–7.

(273) Alrahili M, Savchuk V, McNear K, Pinchuk A. Absorption cross section of gold nanoparticles based on NIR laser heating and thermodynamic calculations. *Sci Rep*. 2020;10(1):1–9.

(274) Hu Y, Liu X, Cai Z, Zhang H, Gao H, He W, et al. Enhancing the Plasmon Resonance Absorption of Multibranched Gold Nanoparticles in the Near-Infrared Region for Photothermal Cancer Therapy: Theoretical Predictions and Experimental Verification. *Chem Mater*. 2019;31(2):471–82.

(275) Yang C, Sui H, Li X, Han J, Luo X, Zhang H, et al. Gold nanoparticle superstructures with enhanced photothermal effect. *CrystEngComm*. 2013;15(17):3490–7.

(276) Riedel R, Mahr N, Yao C, Wu A, Yang F, Hampp N. Synthesis of gold-silica core-shell nanoparticles by pulsed laser ablation in liquid and their physico-chemical properties towards photothermal cancer therapy. *Nanoscale*. 2020;12(5):3007–18.

(277) Faramawy SM. Spectrophotometric Studies on Antioxidants-Doped Liposomes. *J Am Sci*. 2011;7(7):363–9.

(278) Rio ISR, Rodrigues ARO, Rodrigues JM, Queiroz MRP, Calhelha RC, Ferreira ICFR, et al. Magnetoliposomes Based on Magnetic/Plasmonic Nanoparticles Loaded with Tricyclic Lactones for Combined Cancer Therapy. *Pharmaceutics*. 2021;13:1905.

(279) Behera M, Ram S. Synthesis and characterization of core–shell gold nanoparticles with poly(vinyl pyrrolidone) from a new precursor salt. *Appl Nanosci*. 2013;3(1):83–7.

(280) Nonkumwong J, Pakawanit P, Wipatanawin A, Jantaratana P, Ananta S, Srisombat L. Synthesis and cytotoxicity study of magnesium ferrite-gold core-shell nanoparticles. *Mater Sci Eng C*. 2016;61:123–32.

(281) Ravichandran M, Velumani S, Ramirez JT, Vera A, Leija L. Biofunctionalized $MnFe_2O_4$@Au core–shell nanoparticles for pH-responsive drug delivery and hyperthermal agent for cancer therapy. *Artif Cells, Nanomedicine Biotechnol*. 2018;46(S3):S993–1003.

(282) Valeur B. *Molecular Fluorescence: Principles and Applications*. Wiley-VCH; 2001.

(283) Nakamura T, Hayashi S. Enhancement of dye fluorescence by gold nanoparticles: Analysis of particle size dependence. *Japanese J Appl Physics*, Part 1 Regul Pap Short Notes Rev Pap. 2005;44(9A):6833–7.

(284) Greenspan P, Mayer EP, Fowler SD. Nile red: A selective fluorescent stain for intracellular lipid droplets. *J Cell Biol*. 1985;100(3):965–73.

(285) Greenspan P, Fowler SD. Spectrofluorometric studies of the lipid probe, nile red. *J Lipid Res*. 1985;26(7):781–9.

(286) Sakamoto A, Tasumi M. Symmetry of the benzene ring and its normal vibrations: The "breathing" mode is not always a normal vibration of a benzene ring. *J Raman Spectrosc*. 2021;Special Is.

(287) Zhao J, McCreery RL. Multichannel FT-Raman spectroscopy: Noise analysis and performance assessment. *Appl Spectrosc*. 1997;51(11):1687–97.

(288) Sheka EF, Popova NA, Popova VA. Virtual vibrational spectrometer for sp^2 carbon clusters. 1. Polycyclic benzenoid-fused hydrocarbons. *Fuller Nanotub Carbon Nanostructures*. 2021;29(9):703–15.

(289) Maddams WF, Royaud IAM. The characterization of polycyclic aromatic hydrocarbons by Raman spectroscopy. *Spectrochim Acta Part A Mol Spectrosc*. 1990;46(2):309–14.

(290) Baierl P, Kiefer W. Raman Scattering from Molecular Crystals. I. Powdered Naphthalene. *Appl Spectrosc*. 1978;32(2):240–3.

(291) Shinohara H, Yamakita Y, Ohno K. Raman spectra of polycyclic aromatic hydrocarbons. Comparison of calculated raman intensity distributions with observed spectra for naphthalene, anthracene, pyrene, and perylene. *J Mol Struct*. 1998;442(1–3):221–34.

(292) Freire PTC, Barboza FM, Lima JA, Melo FEA, Filho JM. Raman Spectroscopy of Amino Acid Crystals. In: Maaz K, editor. *Raman Spectroscopy and Applications*. IntechOpen; 2017. p. 201–23.

(293) Hernández B, Pflüger F, Derbel N, Conincka J De, Ghomi M. Vibrational Analysis of Amino Acids and Short Peptides in Hydrated Media. VI. Amino Acids with Positively Charged Side Chains: L-Lysine and L-Arginine. *J Phys Chem B*. 2010;114(2):1077–88.

(294) Zhu G, Zhu X, Fan Q, Wan X. Raman spectra of amino acids and their aqueous solutions. *Spectrochim Acta - Part A Mol Biomol Spectrosc*. 2011;78(3):1187–95.

(295) Kurouski D, Van Duyne RP, Lednev IK. Exploring the structure and formation mechanism of amyloid fibrils by Raman spectroscopy: A review. *Analyst*. 2015;140(15):4967–80.

(296) Raeburn J, Chen L, Awhida S, Deller RC, Vatish M, Gibson MI, et al. Using molecular rotors to probe gelation. *Soft Matter*. 2015;11(18):3706–13.

(297) Morris AM, Watzky MA, Finke RG. Protein aggregation kinetics, mechanism, and curve-fitting: A review of the literature. *Biochim Biophys Acta - Proteins Proteomics*. 2009;1794(3):375–97.

(298) Wang SSS, Chen YT, Chen PH, Liu KN. A kinetic study on the aggregation behavior of β-amyloid peptides in different initial solvent environments. *Biochem Eng J*. 2006;29(1–2):129–38.

(299) Kamihira M, Naito A, Tuzi S, Saitô H, Nosaka AY. Conformational transitions and fibrillation mechanism of human calcitonin as studied by high-resolution solid-state ^{13}C NMR. *Protein Sci*. 2000;9(5):867–77.

(300) Vahdat A. *The Importance of Macrophages, Lipid Membranes and Seeding in Experimental AA Amyloidosis*. 2019. 1–60 p.

(301) Cabaleiro-Lago C, Quinlan-Pluck F, Lynch I, Lindman S, Minogue AM, Thulin E, et al. Inhibition of amyloid β protein fibrillation by polymeric nanoparticles. *J Am Chem Soc*. 2008;130(46):15437–43.

(302) Xi WH, Wei GH. Amyloid-β peptide aggregation and the influence of carbon nanoparticles. *Chinese Phys B*. 2015;25(1):018704.

(303) Linse S, Cabaleiro-Lago C, Xue WF, Lynch I, Lindman S, Thulin E, et al. Nucleation of protein fibrillation by nanoparticles. *Proc Natl Acad Sci U S A*. 2007;104(21):8691–6.

(304) Laomeephol C, Guedes M, Ferreira H, Reis RL, Kanokpanont S, Damrongsakkul S, et al. Phospholipid-induced silk fibroin hydrogels and their potential as cell carriers for tissue regeneration. *J Tissue Eng Regen Med*. 2020;14(1):160–72.

(305) Versluis F, Van Elsland DM, Mytnyk S, Perrier DL, Trausel F, Poolman JM, et al. Negatively Charged Lipid Membranes Catalyze Supramolecular Hydrogel Formation. *J Am Chem Soc*. 2016;138(28):8670–3.

(306) El Kechai N, Bochot A, Huang N, Nguyen Y, Ferrary E, Agnely F. Effect of liposomes on rheological and syringeability properties of hyaluronic acid hydrogels intended for local injection of drugs. *Int J Pharm*. 2015;487(1–2):187–96.

(307) Galdiero S, Falanga A, Cantisani M, Vitiello M, Morelli G, Galdiero M. Peptide-lipid interactions: Experiments and applications. *Int J Mol Sci*. 2013;14(9):18758–89.

(308) Cserhåti T, Szögyi M. Interaction of phospholipids with proteins and peptides. New advances IV. *Int J Biochem*. 1994;26(1):1–18.

(309) Warasitthinon N, Genix A, Sztucki M, Robertson CG, Warasitthinon N, Genix A, et al. The payne effect: primarily polymer-related or filler-related phenomenon? *Rubber Chem Technol*. 2019;92(4):599–611.

(310) Kono K, Takagishi T. Temperature-sensitive liposomes. In: Düzgüneş N, editor. Methods in enzymology. *Academic Press*; 2004. p. 73–82.

(311) Hua Pan, Jon N. Marsh, Eric T. Christenson, Neelesh R. Soman, Olena Ivashyna, Gregory M. Lanza, Paul H. Schlesinger, Samuel A. Wickline. Postformulation Peptide Drug Loading of Nanostructures. In: Düzgüneş N, editor. *Methods in enzymology*. Academic Press; 2012. p. 17–39.

(312) Vigata M, Meinert C, Hutmacher DW, Bock N. Hydrogels as drug delivery systems: A review of current characterization and evaluation techniques. *Pharmaceutics*. 2020;12(12):1–45.

(313) Permanadewi I, Kumoro AC, Wardhani DH, Aryanti N. Modelling of controlled drug release in gastrointestinal tract simulation. *J Phys Conf Ser*. 2019;1295(1):012063.

(314) Nappini S, Bonini M, Bombelli FB, Pineider F, Sangregorio C, Baglioni P, et al. Controlled drug release under a low frequency magnetic field: Effect of the citrate coating on magnetoliposomes stability. *Soft Matter*. 2011;7(3):1025–37.

(315) Nappini S, Bombelli FB, Bonini M, Nordèn B, Baglioni P. Magnetoliposomes for controlled drug release in the presence of low-frequency magnetic field. *Soft Matter*. 2009;6(1):154–62.

(316) Zheng D, Ramos-Sebastian A, Jung WS, Kim SH. Fabrication and preliminary evaluation of alginate hydrogel-based magnetic springs with actively targeted heating and drug release mechanisms for cancer therapy. *Compos Part B Eng*. 2022;230:109551.

(317) Lajunen T, Viitala L, Kontturi LS, Laaksonen T, Liang H, Vuorimaa-Laukkanen E, et al. Light induced cytosolic drug delivery from liposomes with gold nanoparticles. *J Control Release*. 2015;203:85–98.

(318) Moretti L, Mazzanti A, Rossetti A, Schirato A, Polito L, Pizzetti F, et al. Plasmonic control of drug release efficiency in agarose gel loaded with gold nanoparticle assemblies. *Nanophotonics*. 2021;10(1):247–57.

(319) Mizuno Y, Furuya H. Volume shrinkage of polypeptide hybrid xerogels induced by a helix-sense inversion. *Polym J*. 2019;51(3):337–44.

(320) Ionov L. Hydrogel-based actuators: Possibilities and limitations. *Mater Today*. 2014;17(10):494–503.